REFERENCE ONLY

UNIVERSITY OF LONDON THESIS

Degree PhD Year 2005 Name of Author METAXAS M.G.

COPYRIGHT

This is a thesis accepted for a Higher Degree of the University of London. It is an unpublished typescript and the copyright is held by the author. All persons consulting the thesis must read and abide by the Copyright Declaration below.

COPYRIGHT DECLARATION

I recognise that the copyright of the above-described thesis rests with the author and that no quotation from it or information derived from it may be published without the prior written consent of the author.

LOANS

Theses may not be lent to individuals, but the Senate House Library may lend a copy to approved libraries within the United Kingdom, for consultation solely on the premises of those libraries. Application should be made to: Inter-Library Loans, Senate House Library, Senate House, Malet Street, London WC1E 7HU.

REPRODUCTION

University of London theses may not be reproduced without explicit written permission from the Senate House Library. Enquiries should be addressed to the Theses Section of the Library. Regulations concerning reproduction vary according to the date of acceptance of the thesis and are listed below as guidelines.

A. Before 1962. Permission granted only upon the prior written consent of the author. (The Senate House Library will provide addresses where possible).

B. 1962 - 1974. In many cases the author has agreed to permit copying upon completion of a Copyright Declaration.

C. 1975 - 1988. Most theses may be copied upon completion of a Copyright Declaration.

D. 1989 onwards. Most theses may be copied.

This thesis comes within category D.

☑ This copy has been deposited in the Library of UCL

☐ This copy has been deposited in the Senate House Library, Senate House, Malet Street, London WC1E 7HU.

Source Localisation and Dose Verification for ~~X-ray Intra-Operative Radiotherapy (IORT)~~ A NOVEL BRACHYTHERAPY UNIT.

Marinos G. Metaxas

Department of Medical Physics and Bioengineering
University College London

A thesis submitted to The University of London for
the Degree of Doctor of Philosophy

June 2005

UMI Number: U592144

All rights reserved

INFORMATION TO ALL USERS
The quality of this reproduction is dependent upon the quality of the copy submitted.

In the unlikely event that the author did not send a complete manuscript
and there are missing pages, these will be noted. Also, if material had to be removed,
a note will indicate the deletion.

UMI U592144
Published by ProQuest LLC 2013. Copyright in the Dissertation held by the Author.
Microform Edition © ProQuest LLC.
All rights reserved. This work is protected against
unauthorized copying under Title 17, United States Code.

ProQuest LLC
789 East Eisenhower Parkway
P.O. Box 1346
Ann Arbor, MI 48106-1346

Abstract

A recent development in the field of radiotherapy has been the introduction of the PRS Intrabeam system (Carl Zeiss Surgical GmbH, Oberkochen, Germany). This is essentially a portable, miniaturised, electron-driven photon generator that allows high intensity, soft-energy x-rays (50 kVp) to be delivered directly to the tumour site in a single fraction. The system has been used for the interstitial radiation treatment of both brain and breast tumours. At present, a standardised in-vivo dose verification technique is not available for the PRS treatments.

The isotropical distribution of photons about the tip of the PRS probe inserted in the tissue can effectively be viewed as a point source of radiation buried in the body. This work has looked into ways of localising the PRS source utilising its own radiation field. Moreover, the response of monoenergetic sources, mimicking realistic brachytherapy sources, has also been investigated. The purpose of this project was to attempt to localise the source as well as derive important dosimetric information from the resulting image.

A detection system comprised of a well-collimated Germanium detector (HPGe) has been devised in a rotate-translate Emission Computed Tomography (ECT) modality. The superior energy resolving ability of the detection system allowed for energy selective reconstruction to be carried out in the case of the monoenergetic source (^{241}Am). Results showed that the monoenergetic source can be localised to within 1 mm and the continuous PRS x-ray source to within 3mm. For the PRS dose map derivation, Monte Carlo studies have been employed in order to extract information on the dosimetric aspect of the resulting image. The final goal of this work was therefore to formulate a direct mathematical relation (Transform Map) between the image created by the escaping photons and the dose map as predicted by the theoretical model.

The formation therefore of the in-vivo PRS image could allow for a real-time monitoring system of the radiation delivery during the treatment whilst providing dose verification maps for patient records.

Acknowledgements

I would like to firstly thank my supervisors, Prof. Robert Speller and Dr. Gary Royle, for all their guidance, support and encouragement throughout my research years here at the Department of Medical Physics and Bioengineering, UCL. I thank them both for giving me the opportunity to improve myself as a scientist and as a person over the past years. I am especially indebted to Dr. Ivan Rosenberg for the kind provision of the PRS system on which the core of this work was based, as well as granting me the opportunity to continue working as a clinical scientist in the TARGIT trial at the Middlesex Hospital, UCLH throughout my research years.

For the purpose of this work, there are a number of people who have been of enormous help to me and need to be cordially acknowledged; namely Dr. Joao Seco whose contribution to the Monte Carlo studies has been enormous, Dr. Kjell Erlandsson for his IDL expertise, the workshop engineers, Stuart Morrison and Denzil Booth for their invaluable help in the phantom constructions. Special thanks must go to Chris Stacey and Steve Morgan for their tremendous input and discussions in the clinical dosimetry of the PRS system.

Furthermore, I would like to thank my colleagues in and around the department who have been very supportive and understanding in the stressful world of research; Jenny Griffiths, Emma Harris, Christy Theodorakou and Tryphon Lambrou.

Finally, to my beloved parents Gerassimos and Katerina, to my sister Assimina and to my brothers Nicholas and Lukas for their warm embrace, support and encouragement even from a long distance.

"Γηράσκω δ' αιεί διδασκόμενος"

I grow old ever learning new things

Solon 638-559 B.C.: Athenian statesman, poet and philosopher who introduced economic, legal and political reforms in Athens.

Table of Contents

Chapter 2 Tools and Techniques employed in the thesis

Chapter 3 Methodology for PRS400 Source Localisation and Dose Verification

Chapter 4 Results on PECT Source Localisation

Chapter 5 In-Vivo Dosimetry for the PRS400 treatments using PECT

List of Figures

List of Tables

CHAPTER 1

Background to Brachytherapy

1.1 Radiotherapy and the aims of Brachytherapy

Radiotherapy (RT) is defined as the therapeutic treatment of malignant cells (i.e. cancer) utilising ionising radiation (photons, electrons or protons) directly applied to the diseased area (tumour). The aim of radiotherapy is to deliver a prescribed amount of radiation dose to the tumour site solely, avoiding unwanted irradiation of the neighbouring healthy tissues. Other therapeutic modalities, such as chemotherapy and surgery, can be used as an alternative or in synergy with radiotherapy to treat cancer. Radiotherapy is categorised into two different modalities; *external beam radiotherapy* (EBRT) and *brachytherapy* (BT). In EBRT, radiation beams irradiate the patient externally from various angular orientations. Insertion of small radioactive sources directly into the tumour or tumour cavity is known as *brachytherapy* or short-distance therapy. Brachytherapy had its beginnings in Europe in the late 1890s with the discovery of radioactive ^{226}Ra (AAPM 1997). In 1903 Alexander Graham Bell wrote, "There is no reason why a tiny fragment of radium sealed in a fine glass tube should not be inserted into the very heart of the cancer, thus acting directly upon the disease material. Would it not be worthwhile making experiments along this line?"(Bell A.G.).

The major advantage of the intratumoural approach is that there is a large difference between the radiation dose delivered to the tumour and that delivered to the surrounding healthy tissue. Radiation intensity falls off as $1/r^2$ (r being the radial distance from the radioactive source) and fall-off is enhanced by radiation absorption within the tumour tissue. Insertion of encapsulated radioactive sources means that superior localisation of the radiation dose delivered to the tumour volume can be obtained, resulting in the sparing of surrounding normal tissues (Khan 1994), however the high dose gradients in the immediate vicinity of the

sources will always pose problems in the accurate assessment of the radiation delivery to the tumour volume (Anderson 1995). Brachytherapy is sub-categorized into different modalities relating to the method of placement of the sources, which strongly depends on the topology, the size and the physiology of the tumour as shown in Table 1.1 (Aird and Williams 1993, Glasgow 1998, Khan 1994).

Method Placement	**Type of Insertion**	**Strength of Sources**	**Absorbed Dose / Rate**	**Duration of Treatment**
Interstitial Intraluminal Superficial Intracavitary	Manual Loading or Remote Loading	40 mCi/pellet (^{137}Cs) 10.0 Ci/pellet (^{192}Ir)	Low Dose Rate (LDR) 0.4-2.0 Gyh^{-1} High Dose Rate (HDR) >12.0 Gyh^{-1}	Permanent Hours/Days Minutes

Table 1.1 Different types of BT treatments. These are characterised by the type of placement, the source strength and consequent absorbed dose rate. Treatment times span from a few minutes to even permanent placement of seeds.

In interstitial BT, radioactive sources are implanted directly into the tumour site using catheters or needles (e.g. breast and prostate gland). In intraluminal BT, sources are temporarily inserted in a linear arrangement in the lumen of an organ (e.g. bronchus, oesophagus) and in superficial BT, such as skin malignancies, sources are supported in a mould over the tumour. Intracavitary BT (ICBT) involves the placement of radioactive sources in an applicator that has been positioned in a body cavity (e.g. the uterus, vagina, and nasopharynx). Acceptable cure rates using ICBT are dependent on being able to deliver significant radiation doses to tissues at considerable distances from the cavity surface, e.g. to the pelvic walls in gynaecological ICBT. To meet these goals, applicator modifications, insertion techniques, dose specification and its formalism have been highly

developed for ICBT systems (AAPM 1993). Insertion of radioactive source can be performed manually or remotely (after-loading). In an after-loading routine, hollow catheters or empty source containers are placed in the target volume and the sources loaded remotely later. This technological advancement greatly reduced the radiation exposure to staff members and allowed for the development and implementation of a range HDR sources (AAPM 1998). Currently there are a number of BT systems routinely used such as the Manchester and Paris system for both interstitial and ICBT and the Quimby system for interstitial BT only (AAPM 1997, Anderson and Presser 1995). The placement of the sources in the body can be temporary or permanent depending on the type of treatment and the source's strength specification. In a permanent BT implant the seeds are left in the tissue (e.g. ^{103}Pd and ^{125}I prostate gland implants). In a temporary implant the sources are inserted for a short period of time (minutes or hours) (e.g. ^{192}Ir breast cancer implants). The strength of BT sources is specified in terms of Air Kerma rate as recommended by ICRU 1985 AAPM 1987 and AAPM 1991. It is defined as the Air Kerma rate in air measured at a reference distance of 1.0m and corrected for air attenuation, in units of μGyh^{-1}. Finally and most importantly, a BT system is also characterized by the dosimetry system employed to prescribe, describe and assess the radiation dose delivered to the patient (Khan 1994). For accurate assessment of the dose distribution around the implanted source, the precise position of the seeds must be determined. Computerised dose calculations or treatment planning (TP) prior to a BT treatment is therefore necessary for delivering a homogeneous radiation dose, which avoids hot spots in the tumour site and the surrounding normal tissues.

1.2 Current Techniques of Planning/Checking in Brachytherapy

The need for source localisation is an important issue in the field of BT. In order to calculate dose distributions, the positions and orientation of the radioactive sources relative to the target volume and relative to each other must be known. An anatomical target volume, which is generally diseased tissue surrounded by an acceptable margin of presumably normal tissue, must be determined prior to

performing an implant. A BT dosimetry system, as specified by ICRU guidelines (ICRU 1985), is denoted by "a set of rules taking into account the source strengths, geometry and method of application in order to obtain suitable dose distributions over the volume(s) to be treated." In order to calculate the dose distributions around the implanted volume, the coordinates of the location of the radioactive sources must be accurately determined. Source localisation is most commonly accomplished by external radiographic systems that utilise the attenuating properties of the source holders. A minimum of two radiographs, obtained simultaneously or sequentially with no movement of the source is required. These radiographs must be taken from different perspectives, normally in an orthogonal orientation (anterior-posterior AP and lateral), with both the implanted source and a reference point visible on the films. Dummy source holders instead of real sources are employed for the planning of the BT treatments. Meli (1995) reviewed several methods for radiographic source localisation and these are presented in Table 1.2; they fall into three broad categories: isocentric radiographs, shift radiographs and non-isocentric radiographs. Non-orthogonal localisation techniques are required when the applicators and dummy sources are not visible on the radiographs (e.g. cervical cancer). Recent advances in digital radiography now allow films to be scanned directly into computers for display and source identification, rather than the commonly used manual digitisation of the applicator or source coordinates from the developed radiographs. Modern treatment planning systems (TPS) in BT are able to display the isodose curves of the radiation field directly on the radiographs. BT is routinely performed with the aid of radiographs, thus limiting the information on the dose distribution in organs at risk. Most commonly used TPS extract 2-dimensional information (seed localisation) from the radiographs to provide a dose distribution map. Film dosimetry in BT is therefore carried out on a point-based dose prescription rather than a volume based prescription (Fragoso 2003). Currently, BT is facing new challenges as recent advances in medical imaging continue to open the door to innovative planning and checking techniques (Deehan 2000). In their list of future research recommendation in clinical BT, Cumberlin and Coleman (2002) suggest, "New techniques for anatomical localisation of target volume should be developed" (Recommendation 6).

Method of source Identification	Number of films	Film Orientation	Magnification method	Accuracy	Comment
Manual	2	Orthogonal Isocentric	Geometric reconstruction (exact)	Excellent (0.5-2.0mm)	Most accurate: limited only by patient movement
			Average magnification (approximate)	Good (2.0-5.0mm)	Works best for small sources grouped near isocenter
Manual	2	Arbitrary angle Isocentric	Geometric reconstruction (exact)	Good	Can select angle to maximise source visibility.
			Average magnification (approximate)	Modest (> 5.0mm)	Less accurate than true orthogonal
Manual	2	Stereo Shift	Geometric reconstruction (exact)	Good	Even with an exact calculation small error (0.5mm) yield measurable magnification errors
			Average magnification (approximate)	Modest	Less accurate as it combines inherent shift errors with magnification errors
Auto	3	Implant near isocenter Isocentric films with 45° angle between them	Average magnification (approximate)	Modest	Works best for closely spaced sources in small implants
Auto	3	One vertical film: two ± 8° from vertical films at isocenter	Geometric reconstruction	Good	Works best for closely spaced sources in small implants
Auto	2	Arbitrary angles not necessary co-planar	Geometric reconstruction	Modest	Requires location of tips and ends of each source

Table 1.2 Review of different source localisation radiographic techniques in Brachytherapy (adapted from Meli 1995).

Furthermore, consideration should also be given in the "soft tissue deformation during insertion procedure, which is the most formidable obstacle in the meaningful application of 3D imaging in the planning and guidance of BT..." (Recommendation 7).

Digital images from CT and MRI scanners are nowadays widely used for BT treatment planning. In interstitial BT, post-implant dosimetry checks are performed using CT or MRI scans, from which dose-volume histograms (DVHs) are generated (Li *et al* 2001). Usually a series of parallel, transverse slices through the treatment volume and its surroundings are obtained, which can act as an accurate method of identifying the position and orientation of intracavitary brachytherapy (ICBT) applicators (Lerma and Williamson 2002). The digital images are displayed on the treatment planning computer monitor, which has the ability to enhance them, so that the source or x-ray marker positions, the target volume and the surrounding organs can be viewed more clearly. MRI and Ultrasound (US) imaging are preferred over CT imaging as they offer superior soft tissue delineation. However, while 3-D images are effective in delineating gross anatomy, they usually do not sufficiently distinguish diseased tissue from healthy tissue. Another drawback of using CT and MRI scanning is that serial scans are not always continuous and can be separated by a few millimetres. Therefore, they may fail to show dummy sources lying between adjacent serial or reconstructed scans (Lerma and Williamson 2002).

More recently, there has been great concern to move towards real-time monitoring and verification of HDR brachytherapy treatments using various imaging techniques (Nakano *et al* 2003, Duan *et al* 2003, Sheikh-Bagheri and Munro 1998). This allows for dynamic assessment of the treatment delivery, enabling fast user intervention and abortion of treatment if required. The imaging techniques employed by various authors for real time BT monitoring is the point of interest in this work and will be discussed at length in Chapter 5.

In summary, BT is one of the therapeutic modalities in modern RT that involves the permanent or temporary insertion of radioactive sources directly upon the tumour site or tumour cavity. Dosimetry checks and treatment outcome are dependent on localisation of the radioactive seeds in the tissue, such that the distribution of dose delivered can be computed. Various verification methods for

source position exist, some of which can provide a means for real-time monitoring during treatment.

1.3 Introduction to the PRS400 - A novel Brachytherapy unit

Photoelectron Corp. (Lexington USA), (now Carl Zeiss Surgical GmbH, Oberkochen, Germany) were the primary manufacturer of a novel, miniature electron accelerator, a novel brachytherapy source, which does not have the drawbacks of radioactive implants. The Photonic Radiosurgery System (PRS) is a needle-shaped x-ray generator that can deliver interstitial radiation doses in a single treatment session (see Fig. 1.1). It is an electronically controlled, high-intensity, low-energy x-ray point source. The radiation output is generated by an electron beam impinging on a thin gold (Au) target located at the end of an evacuated drift tube (probe).

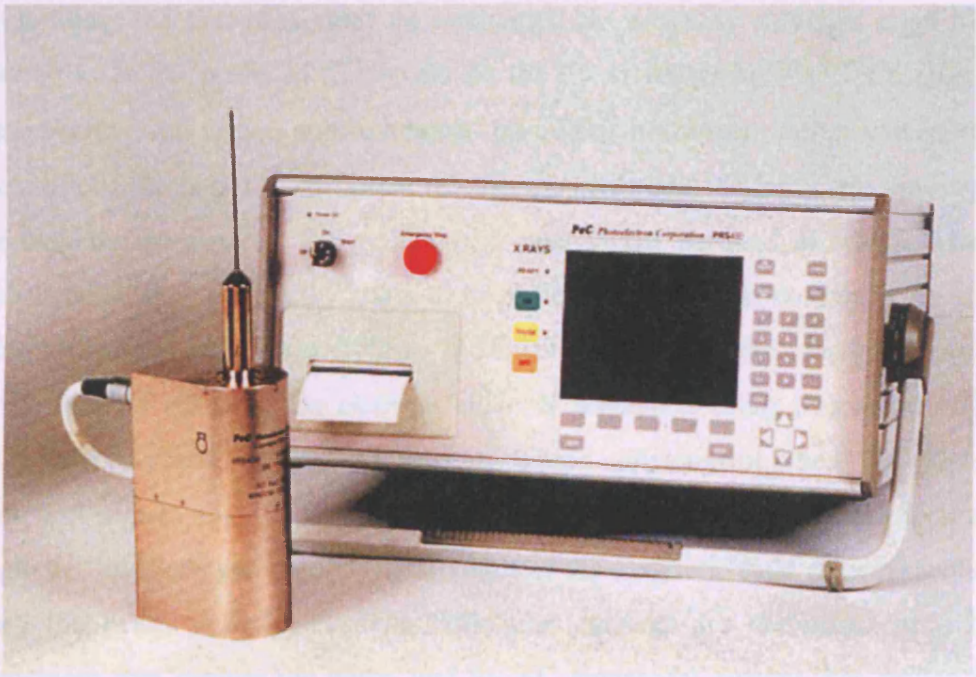

Figure 1.1 The PRS400 system. The miniature x-ray source XRS (left) and its control console (right) are shown. The XRS weighs 1.57kg (3.45lbs) and its dimensions are 17.5x11.0x7.0 cm.

1.3.1 PRS400 Specifications

The heart of the PRS system is a thin needle, 3.2 mm in diameter and 100 mm long, from whose tip low energy x-ray photons are isotropically emitted. The system is comprised of the x-ray source (PRS) and the control console that powers the XRS electronics. The control console is microprocessor based and contains a colour flat panel display (VDU), which provides additional information to ensure the safety and effective use of the system. The housing of the PRS contains the electronics that produce and steer the beam of electrons down the probe. The electrons are generated by an electron gun at various beam currents (5, 10, 20 or 40 μA). The gun is a conventional miniature gun with a barium oxide thermionic cathode (Dinsmore *et al* 1996). The resulting electron beam produced is approximately Gaussian in shape with a diameter of 0.35±0.05mm. The beam is accelerated through a high voltage field (30, 40 or 50 kV) and it then passes through a deflection chamber to ensure beam straightness. Figure 1.2 shows the cross section schematic of the housing of the PRS x-ray source. Following acceleration, the electrons enter an evacuated, magnetically shielded, rigid tube, referred to as the probe in this work. At the tip of the probe the electrons hit a hemispherical Au target, approximately 1μm thick and x-rays are produced. The thickness of the target is sufficient to stop the electrons, whilst at the same time allowing the passage of the generated x-rays in the forward direction. Monte Carlo studies showed this thickness to be optimal for x-ray production at the PRS energy (Yanch and Harte 1996). In order to achieve the nearly spherical distribution of photons, the electron beam is precessed using two sets of X-Y beam deflection coils in the PRS housing. These coils control where the electron beam will impact with the target. Deflection currents are applied to these coils and magnetic fields are generated. The strength of the magnetic field determines how much the beam is deflected. The deflection currents are composed of a DC component that centres the beam and an AC sinusoidal current that causes the beam to move in a circular manner around the tip of the probe. This process is known as beam *dithering*; describes a continuous "ring" shaped target, which results in a spherical x-ray distribution (cloud) about the tip of the probe.

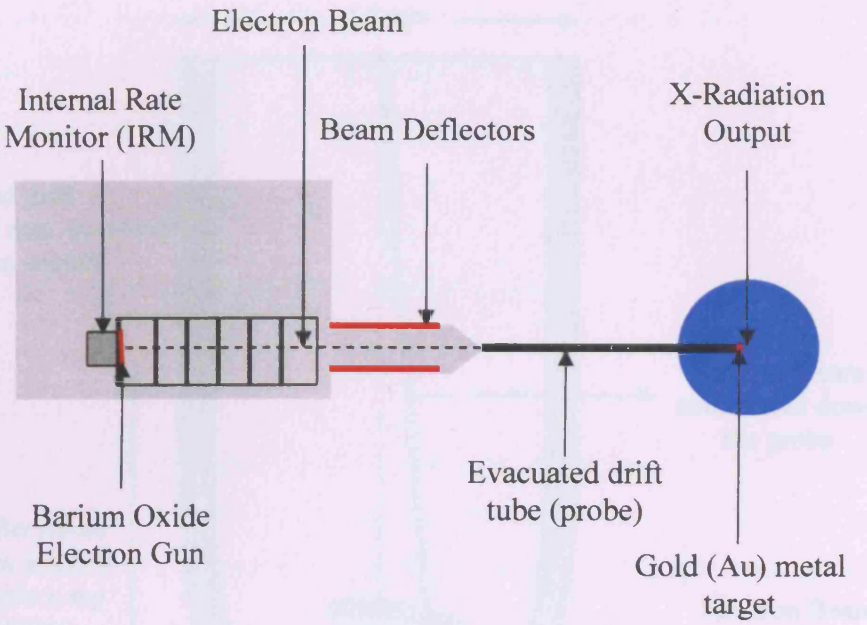

Figure 1.2 Internal schematic of the PRS housing. The electron beam is accelerated down the probe and "steered" accordingly by the deflection coils in order to produce an isotropic distribution of soft x-rays (50 kVp).

Figure 1.3 shows a detailed cross sectional diagram of the tip of the probe. This can be viewed as a point source whose "apparent" centre of the dose distribution lies within the probe, approximately 0.9 mm from its tip (Biggs and Thomson 1996). The probe surface is coated with chromium nitride (CrN). The round tip of the probe contains a beryllium substrate (2cm length). This radiation translucent material allows un-attenuated emission of x-rays thus providing an isotropic distribution. There is a nickel film under the probe's surface to improve adhesion and durability. These coatings determine the low-energy cut-off of the x-ray spectrum (Biggs and Thomson 1996).

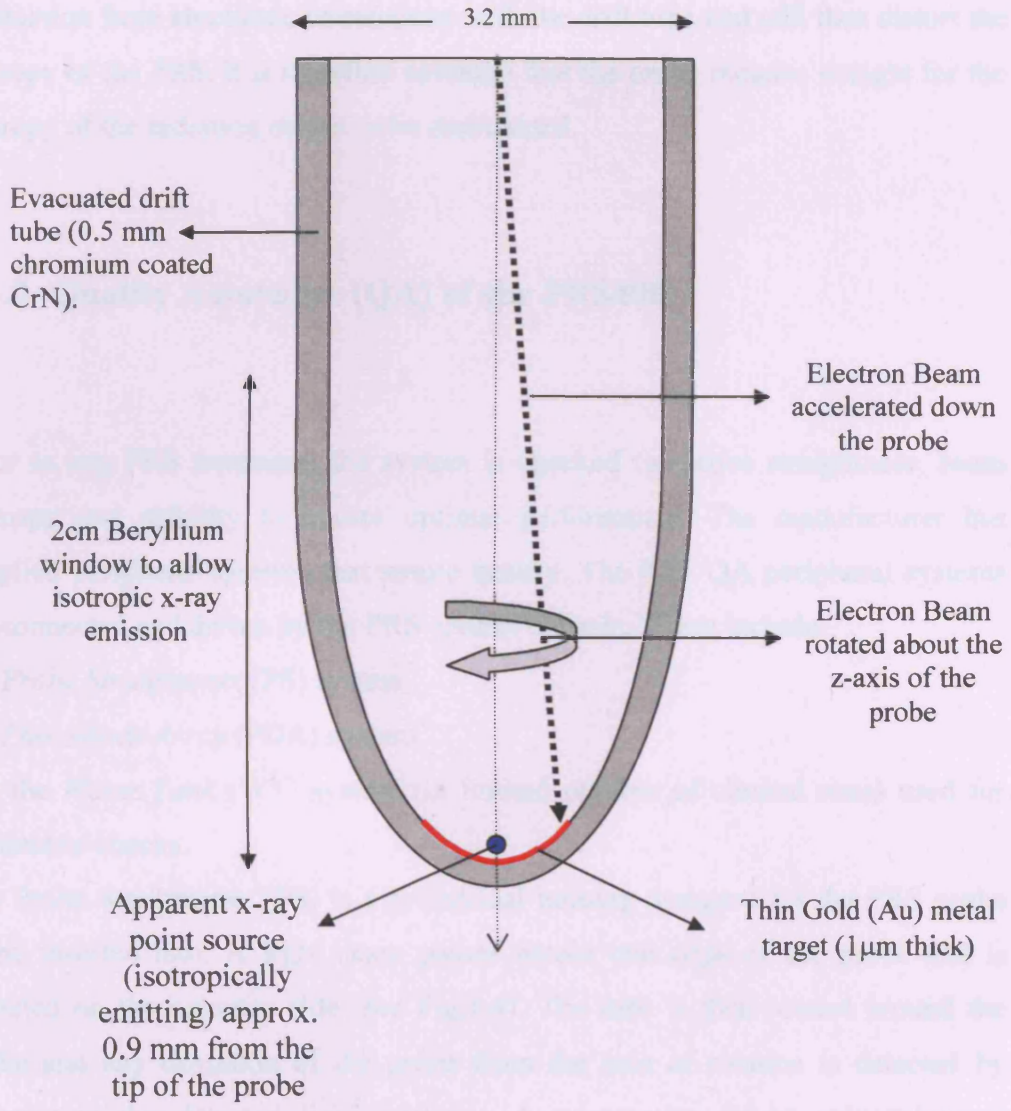

Figure 1.3 Enlargement of the tip of the PRS drift tube. The rotating electron beam strikes the gold metal target to produce a near spherical distribution of low-energy (soft) x-rays at the tip of the probe. The emitted radiation output can be considered as a point source of radiation at approximately 0.9 mm from the end of the probe.

For stable operation, the electron beam is shielded from external magnetic fields and from both dc and ac stray magnetic fields in the operating room.

The drift tube of the PRS is mechanically vulnerable. Bending of the probe will result in non-uniform x-ray production, as electrons will be striking the internal

edges of the drift tube. This will cause additional, non-controllable x-ray production from electronic interactions with the drift tube and will thus distort the isotropy of the PRS. It is therefore essential that the probe remains straight for the isotropy of the radiation output to be maintained.

1.3.2 Quality Assurance (QA) of the PRS400

Prior to any PRS treatment, the system is checked for probe straightness, beam isotropy and stability to ensure optimal performance. The manufacturer has supplied peripheral systems that assure quality. The PRS QA peripheral systems are connected and driven by the PRS control console. These include:
the *Probe Straightener* (PS) system,
the *Photodiode Array* (PDA) system,
and the *Water Tank* (WT) system (in limited number of clinical sites) used for dosimetric checks.
The Probe Straightener (PS) is a cylindrical housing designed for the PRS probe to be inserted into. A light beam passes across one edge of the probe and is detected on the opposite side (see Fig.1.4). The tube is then rotated around the probe and any deviation of the probe from the axis of rotation is detected by changes in the detected light intensity. A micrometer driven axle (plunger) controlled by a mechanical stopper can be used to gradually press the probe back to a desired position, according to any light deviation detected. The process is carefully repeated until the light intensity deviation recorded on the photo-detector is to within tolerance. The straightness of the probe can be confirmed and adjusted when necessary to within ±0.01mm. Once straightness is checked, the PRS radiation output needs to be carefully assured for quality. The PDA is a means of checking the directional uniformity or isotropy of the radiation output. Again, the PDA is designed to be inserted over the PRS probe and is used to confirm the isotropy of the radiation output at various orientations.

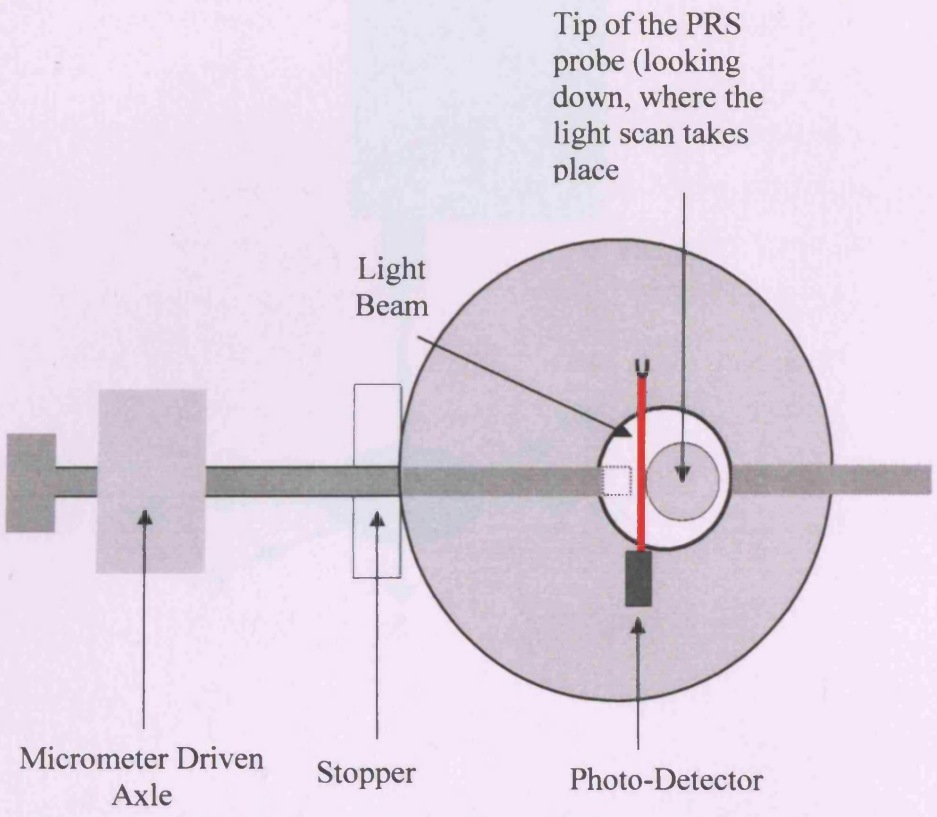

Figure 1.4 Internal schematic of the Probe Straightener (PS). The light beam is rotated around the tip of the probe to check its straightness. A mechanical plunger can be used to adjust the probe back to its vertical position.

An array of photodiode detectors is positioned equidistant from the isocenter at the tip of the probe, i.e. at 1 cm from the edge of the tip designed. The orientation of the PDA can be seen in Figure 1.5. The z amplitude relates to the focusing of the beam along the axis of the electron beam propagation. Once the beam is focussed on the metal target, the deflection coils are adjusted automatically in order to produce the rotation of the electron beam. The response of the photodiodes in the ± x and in the ± y direction are used in turn to optimise the beam isotropy accordingly.

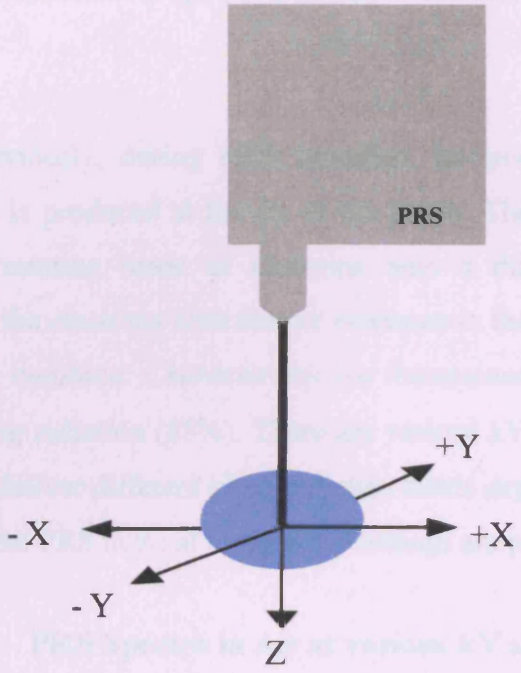

Figure 1.5 The orientation of the photo diodes (PDA) that are employed for the measurement and adjustment of the PRS beam isotropy. The diodes are placed 1cm from the isocenter, i.e. the tip of the probe, and are used to monitor the radiation output.

The isotropy adjustment process is performed automatically by the control console and is specified by the manufacturer to within 10% (PeC, USA). Beam stability is constantly checked using radiation monitors that are independently employed. Each of these consists of a BGO (Bismuth Germanium Oxide) scintillation detector. One of these is placed in the PRS x-ray gun housing and is thus referred to as the Internal Rate Monitor (IRM) (See Fig 1.2). The IRM is placed along the z-axis of the probe and is used to monitor x-ray production in the backward direction. The IRM counts are implemented in the calculation of the PRS's dose rate and are set as the standard for computing the monitor units (MUs) required for a prescribed treatment. The other detector is external to the PRS source and can be used to monitor the radiation output during treatment. The PRS console constantly monitors the count rate of both these counters and will prompt the user to abort treatment if the reading falls beyond a certain threshold.

1.3.3 X-Ray Emission spectra of the PRS400 output

As stated previously, during PRS operation, an isotropic distribution of low-energy x-rays is produced at the tip of the probe. These x-rays are produced by impinging a rotating beam of electrons onto a thin gold metal target. The interaction of the electrons with atomic electrons in the metal target produces two types of x-ray emission: *Characteristic* (or fluorescence) x-rays (about 15%) and *Bremsstrahlung* radiation (85%). There are various kV and μA settings, allowing the system to deliver different sized radiation fields depending on the tumour size. Spectra from the PRS in air at various kV settings are presented in Figure 1.6.

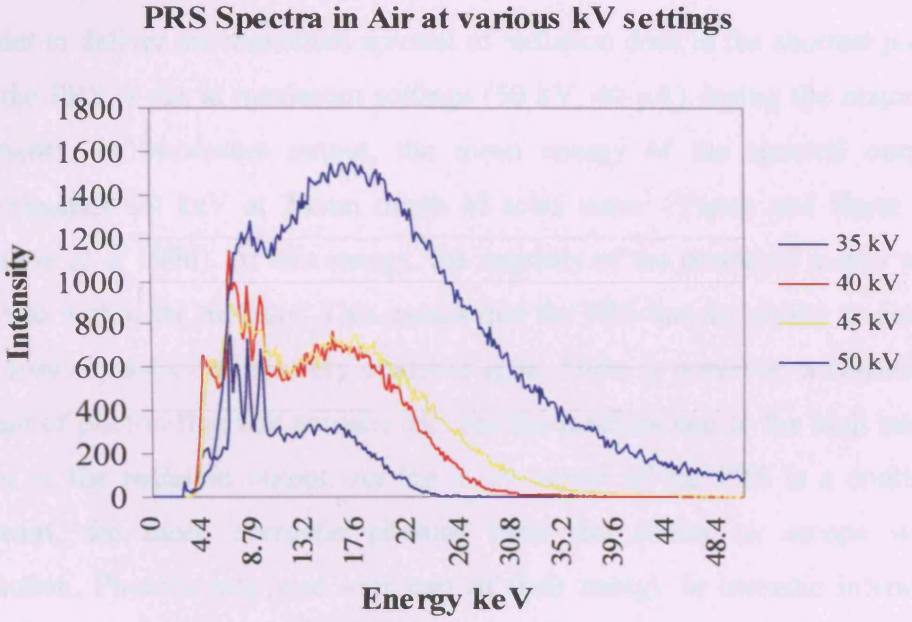

Figure 1.6 PRS spectra in air at various kV settings (35, 40, 45, 50 kV) at constant tube current (40 μA) measured on a High Purity Germanium detector (HPGe).

The lowest-energy peak (7.36 keV) closely matches the L_3-K and L_2-K transitions of Ni and comes from the nickel coating of the drift tube. The Au lines are identified as the M-L_3 transition at 9.62 keV, the M-L_2 transition at 11.42 keV and the free-L_3 transition at 11.92 keV (Dinsmore *et al* 1996).

The PRS half-value layer (HVL) measurements at maximum output have been performed by other authors (Beatty *et al* 1996) and are given in Table 1.3.

PRS maximum output 50 kVp, 40 μA	Half Value Layer (HVL) Aluminium thickness	Corresponding Equivalent Photon Energy
In Air	0.10mm	10.0 keV
In 5mm solid water	0.30mm	14.8 keV
In 10mm solid water	0.71mm	19.9 keV

Table 1.3 Half Value Layer (HVL) measurements made on the PRS in air and in solid water material. (Beatty *et al* 1996)

In order to deliver the maximum amount of radiation dose in the shortest possible time the PRS is run at maximum settings (50 kV, 40 μA) during the majority of treatments. At maximum output, the mean energy of the spectral output is approximately 20 keV at 20mm depth of solid water (Yanch and Harte 1996, Dinsmore *et al* 1996). At this energy, the majority of the produced x-rays will be absorbed within the medium. This means that the PRS has the ability to deliver a high dose of radiation in a very confined area. There is however, a considerable amount of photon flux that actually escapes the medium due to the high intensity nature of the radiation output. As the x-ray output of the PRS is a continuous spectrum, the more energetic photons have the ability to escape without interaction. Photons may also lose part of their energy in inelastic interactions (Compton interactions) in the medium and still manage to escape the object with consequently lower energy. At maximum setting, the emitted photon flux vs. scatter material thickness as recorded with a Germanium detector at maximum setting is presented in Figure 1.7. The scattering material in this case is Perspex (PMMA) placed in front of the PRS source and the consequent photon flux transmitted is measured at a distance of 0.5m using a 30μm pinhole placed at the face of a High Purity Germanium detector (HPGe). The detector signal is collected using a high rate amplifier and is quoted in terms of counts detected per second (cps).

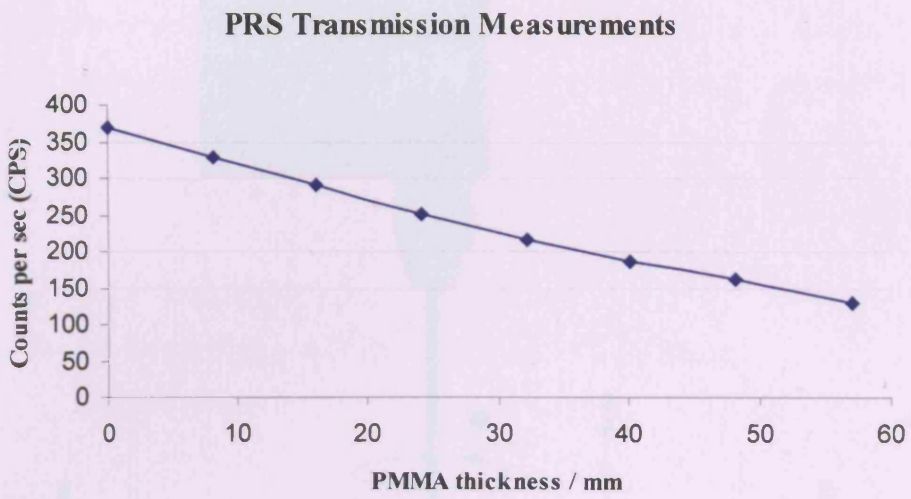

Figure 1.7 Transmission measurements of the PRS source in air through various thicknesses of PMMA. A high rate amplifier was employed to accommodate the high intensity flux produced by the PRS.

1.3.4 PRS400 Dose Distribution measurements

The dosimetry of the PRS is performed using a dedicated water tank supplied by the manufacturer. This tank is designed to measure the dose delivered in water by the PRS (Yasuda *et al* 1996). The detector used is an ionisation chamber (IC) (PTW Type N23342, PTW, Freiburg, Germany). This soft x-ray, 0.02 ml parallel plate detector is used to measure absolute dose depth curves. The principle of operation of the water tank is shown in Figure 1.8. The probe axis lies along the z-axis of the x-z coordinate system. The origin of this coordinate system is located at the point at which dose is measured by the ionisation chamber and the PRS is mounted with the probe vertical and can be moved in the x-z plane.

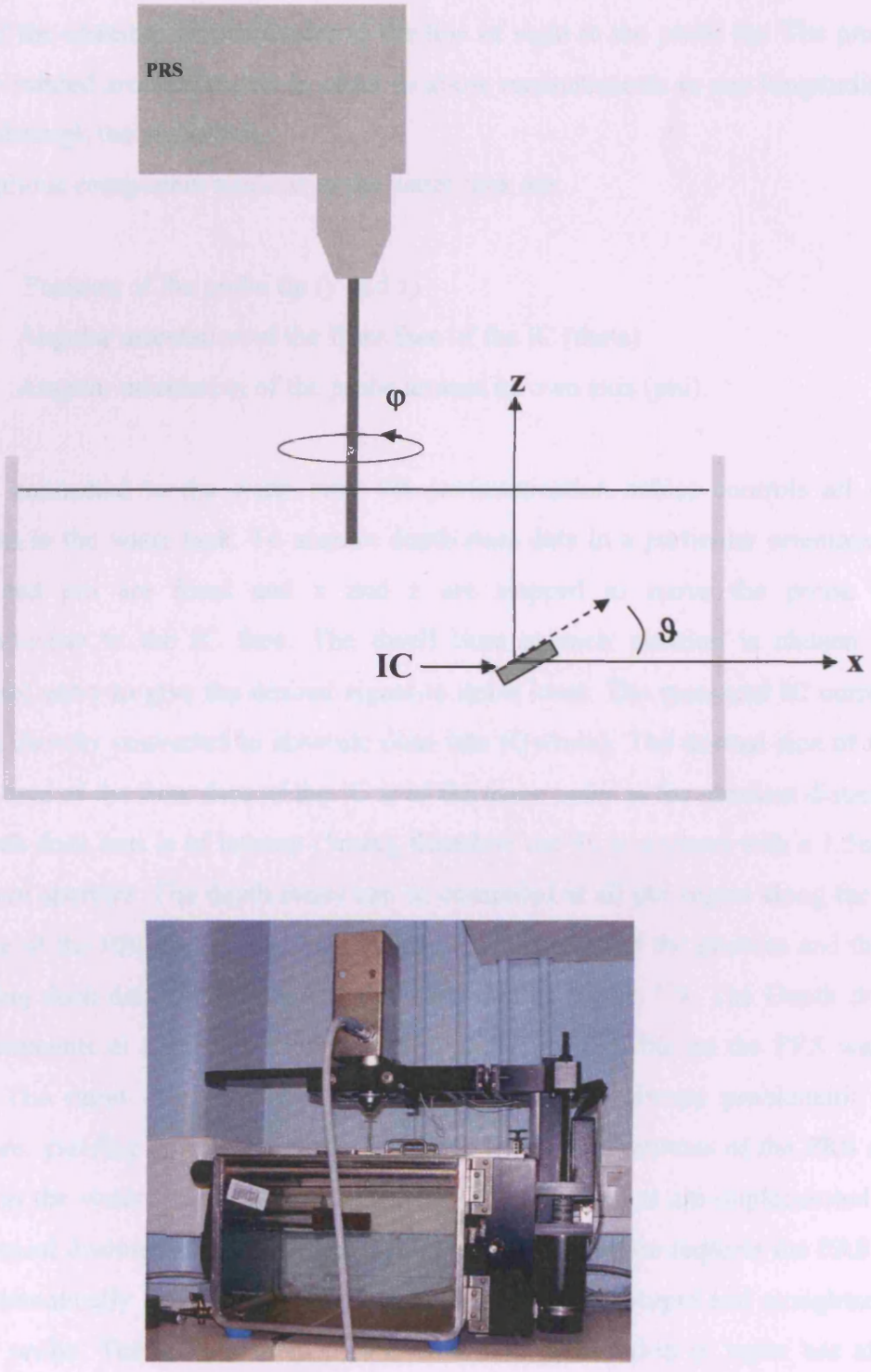

Figure 1.8 Diagram (top) and picture (bottom) of the water tank employed to perform dosimetric checks on the PRS. This system is used to record the probe's output at various angular orientations using an ionisation chamber (IC). The absolute dose rate of the system is assessed so accurate treatments in terms of radiation dosage prescription can be delivered.

For any x-z position of the probe tip, the ion chamber is rotated to keep the front face of the chamber perpendicular to the line of sight to the probe tip. The probe can be rotated around its axis in order to allow measurements in any longitudinal plane through the probe axis.
The various component motions in the water tank are:

a) Position of the probe tip (y and z)
a) Angular orientation of the front face of the IC (theta)
c) Angular orientation of the probe around its own axis (phi).

A PC connected to the water tank via communication cables controls all the motions in the water tank. To acquire depth dose data in a particular orientation, theta and phi are fixed and x and z are stepped to move the probe tip perpendicular to the IC face. The dwell time at each position is chosen by keyboard entry to give the desired signal-to noise level. The measured IC current can be directly converted to absolute dose rate (Gy/min). The normal size of the active area of the front face of the IC is of the same order as the smallest distance at which dose data is of interest (5mm), therefore the IC is covered with a 1.5mm platinum aperture. The depth doses can be computed at all phi angles along the x-z plane of the PRS probe. The near isotropic distribution of the photons and their resulting dose delivery in water is demonstrated in Figure 1.9. The Depth dose measurements at a distance closer than 5mm are not possible on the PRS water rank. The rapid dose gradients at such distances are always problematic to measure, yielding erroneous results. Absolute dose measurements of the PRS are made in the water tank at 10mm for the tip of the probe and are implemented in the clinical dosimetry of the PRS. Standard clinical procedure requires the PRS to be systematically checked for stability and isotropy of its output and straightness of the probe. The measurement of the PRS dose distribution in water has also been performed using radiographic film dosimetry. Radiographic film (Gafchromic MD-55 Dosimetry Media, ISP, USA) which was sensitive to low-energy x-radiation was inserted between two solid water cylinders with a groove cut in the centre of them for perfect fit of the PRS probe. The colouration of the film during irradiation demonstrated visually (see Figure 1.10) the near-spherical distribution of photons about the tip of the PRS probe.

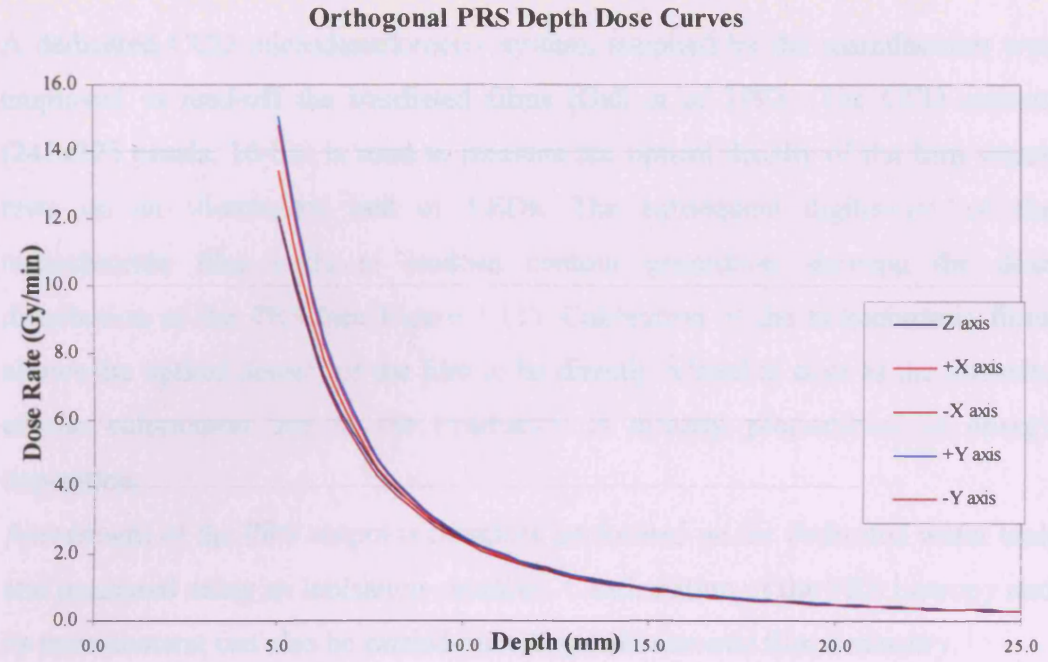

Figure 1.9 Depth Dose curves of the PRS in water. Isotropy of the beam is confirmed by measurement of the dose rate at all angular orientations about the tip of the probe. The PRS enables the delivery of high intensity, low-energy (50 keV max) photons, at a dose rate of about 3Gy/min at 10mm from the tip of the probe.

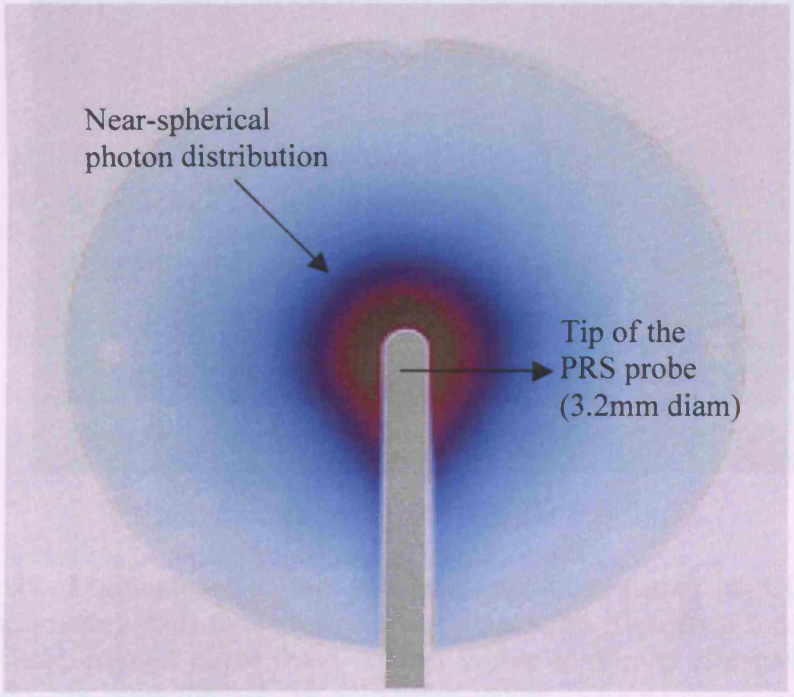

Figure 1.10 PRS irradiated radiochromic film. The blue circle around the tip of the probe demonstrates the isotropy of the PRS output. The intensity of the colouration of the irradiated film is proportional to energy deposition, and thus the information about dose distribution can be extracted directly from the film.

A dedicated CCD microdensitometer system, supplied by the manufacturer was employed to read-off the irradiated films (Gall *et al* 1993). The CCD camera (242x375 pixels, 16-bit) is used to measure the optical density of the film which rests on an illuminated bed of LEDs. The subsequent digitisation of the radiochromic film leads to isodose contour generation showing the dose distribution of the PRS (see Figure 1.11). Calibration of the radiochromic films allows the optical density of the film to be directly related to dose as the intensity of the colouration due to the irradiation is directly proportional to energy deposition.

Assessment of the PRS output is therefore performed on the dedicated water tank and measured using an ionisation chamber. Confirmation of the PRS isotropy and its measurement can also be carried out using radiochromic film dosimetry.

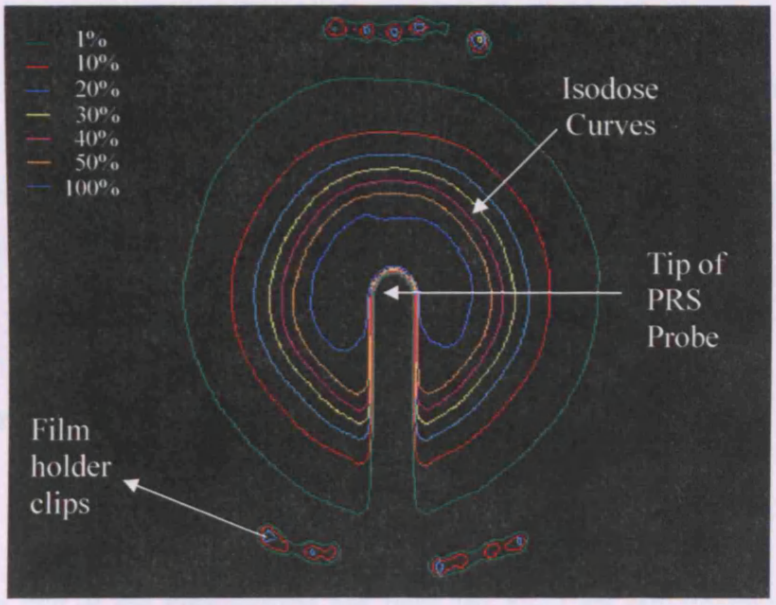

Figure 1.11 Digitisation of the radiochromic film (using a CCD based microdensitometer) leads to isodose contour generation. The small indentation in the inner most contour curve (blue colour) is due to minute attenuation of the transmitted x-ray beam through the gold metal target.

Summarising, the quality assurance (QA) peripherals and the dosimetric studies performed on the PRS confirm the near-spherical distribution of photons about the tip of the probe. The PRS produces an intense beam of low-energy (soft) x-rays able to deliver a dose rate of about 3 Gy/min at a distance of 10mm from the tip of the probe. The radiation output of the PRS can be regarded as a point source of x-radiation embedded in the tissue, thus rendering it a brachytherapy (BT), high dose rate (HDR) treatment system. This novel system has advantages over conventional BT radioactive sources in terms of operator safety together with handling and storage and disposal of BT seeds.

1.4 Clinical Applications of the PRS400

The PRS system is designed for interstitial radiotherapy, delivering a high intensity beam of soft x-rays in a single session. The invasive nature of the probe (100mm length, 3.2mm diameter) allows delivery of radiation directly to the tumour site. Furthermore, new applications of the PRS have explored the possibility of treating surgical tumour cavities, i.e. the cavity created following tumour excision.

1.4.1 Stereotactic Brain Radiosurgery

The primary use of the PRS system has been the adjuvant radiotherapy of brain metastatic tumours. These are solid tumours by nature and can be treated interstitially using the PRS during standard strereotactic biopsy procedures (Warnke et al 2003, Cosgrove *et al* 1997). This is achieved by affixing the PRS housing onto a stereotactic frame (CRW stereotactic frame, Radionics, USA), allowing the probe to be inserted down the same canula as the biopsy needle (see Figure 1.12). The PRS probe is inserted once confirmation of tumour histo-pathology is available, ensuring that it is placed in the centre of the malignant

structure. The HDR achieved by the PRS means that treatment times are considerably shortened. Feasibility studies on the PRS requested for FDA (Food and Drug Administration, USA) approval were performed using this technique. The outcome proved the technique to be successful and the PRS system was granted approval for the treatment of metastatic brain tumours in 1998. A year later it was approved for the radiotherapy treatment of any solid tumours, either as an adjuvant or in a single session radiotherapy treatment. In adjuvant radiotherapy, the PRS is used to deliver a localised fraction of radiation treatment (local boost) followed by external beam radiotherapy (EBRT). Furthermore, the PRS has proved very useful in treating patient with recurrent malignancies for whom further exposure of healthy brain tissue to external beams is contraindicated. Brain radiosurgery using the PRS is currently undertaken in many medical centres around the world.

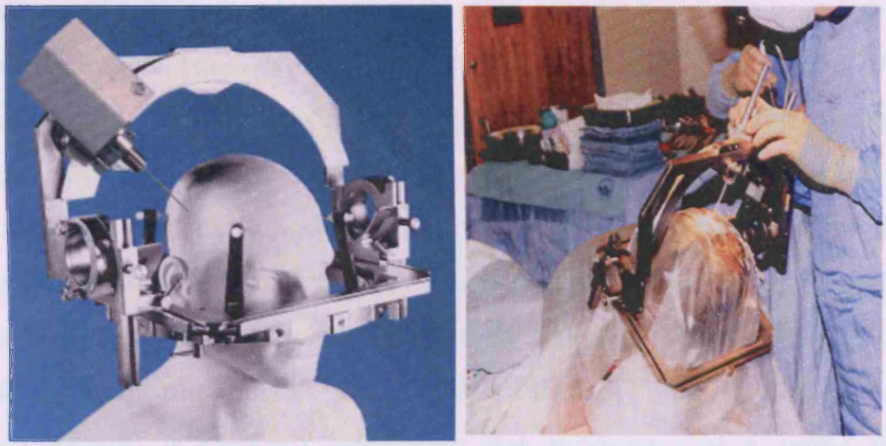

Figure 1.12 The PRS affixed onto the CRW brain stereotactic biopsy frame (left). The PRS is inserted down the biopsy track and is able to deliver radiation interstitially (right). Single fraction doses of 10 to 20 Gy are delivered to the periphery of the lesions generally in less than 30 minutes.

1.4.2 Intra-Operative Radiotherapy (IORT)

IORT is defined as an Intracavitary radiotherapy treatment that provides a localised radiative boost to the bed of a tumour following its surgical resection

(excision). IORT is performed in the operating theatre and requires mobile radiotherapy units for in-situ treatment. Currently, there are such devices available specially designed for IORT; an electron beam, mobile linear accelerator (LINAC) has been designed (NOVAC7, Hitesys Inc, Italy) and is currently implemented in the IORT treatment of breast cancers (Picardi *et al* 2000, Veronesi *et al* 2001). The PRS's compact size and thus ease of transportation, renders it a possible candidate for IORT. The system is currently used for the treatment of early breast cancers in a number of centres around the world. Studies have shown that recurrence of breast cancer in over 90% of cases takes place in the same index quadrant as the primary site (Baum and Vaidya, 1997). These findings have lead to the rationale that radiation delivery to the index quadrant of the excised tumour (i.e. following lumpectomy) may be sufficient to control the disease and prevent recurrences (Vaidya *et al* 2004). Conventionally, breast cancer is treated by lumpectomy followed by a six-week post-operative fractionated EBRT. Randomised trials at 30 months follow up have indicated that brachytherapy is equivalent to whole breast radiotherapy (Polgar *et al* 2002). This result provided further evidence for the treatment of the index quadrant solely. The idea of delivering a single fraction of radiation to the tumour bed following its resection was first introduced by Professor M. Baum's team at the Institute of Surgical Studies, UCL and has been pioneered at the Middlesex Hospital UCLH. The viability of this technique is currently being tested (Vaidya *et al*, 2001). A multi-centred randomised trial called TARGIT (Targeted Intra-operative Radiotherapy) is currently underway; this proposes that a single fraction of radiation to the index quadrant of the excised tumour alone could achieve as good a local control as radiotherapy to the whole breast (EBRT). If proven equivalent in terms of local recurrence and cosmesis, this could eliminate the need for expensive and time-consuming post-operative EBRT.

In order to achieve conformity of the PRS probe to the tumour bed, spherical applicators of various sizes depending on the cavity have been designed (see Figure 1.13). The applicators have been specially manufactured so that the radiation output of the PRS is not perturbed or distorted in any way. The manufacturer for has not disclosed the material that these applicators are made off for proprietary reasons. The pliable breast tissue can be wrapped around the applicators. The PRS source is always in the centre of the applicator regardless of

its size and in this way the applicator is used to encompass the diseased tissue. Thus conformity of the PRS to the target volume is achieved. The PRS is fixed to the desired position in the breast using a dedicated gantry (Intrabeam, Zeiss).

The radiation dose for the TARGIT trial treatment is prescribed to be 5 Gy at 10mm from the edge of the spherical applicator. The largest size applicator employed is 5cm in diameter.

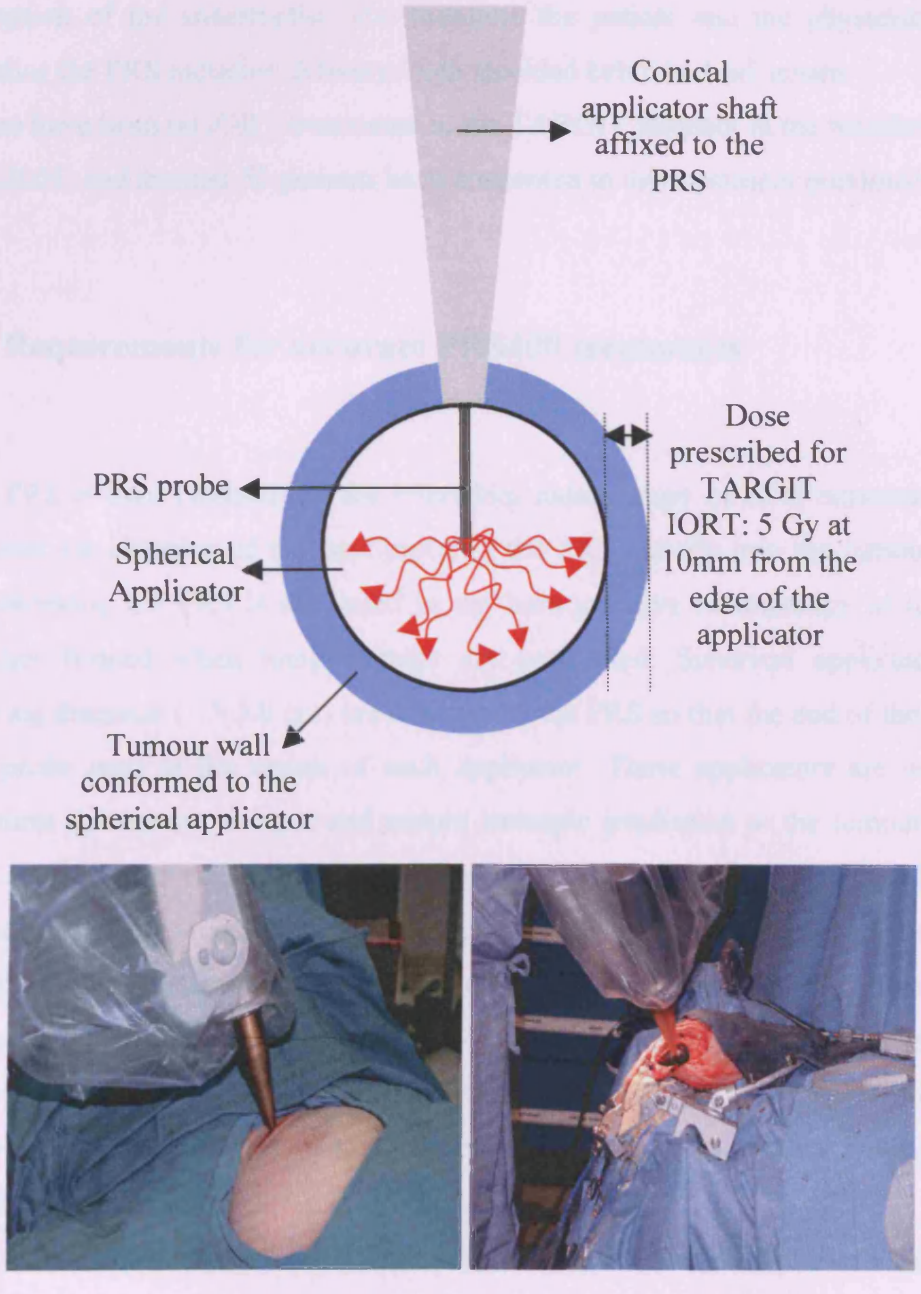

Figure1.13 Enlargement of the spherical applicator is shown in the top picture. The tip of the probe lies in the centre of the applicator allowing uniform irradiation of the tumour wall. The PRS applicator is inserted in the breast (bottom left) and in the brain (bottom right). Typical treatment times are about 30 minutes.

The tip of the probe is placed in the centre of the applicator, as stated previously and treatment delivery time for 5 Gy at 35mm from the tip is about 35 minutes.
The advantage of this treatment is that the patient is still under general anaesthesia, thus minimising movement and ensuring accurate local radiation delivery.
During the actual treatment the operating theatre staff vacate the premises with the exception of the anaesthetist who monitors the patient and the physicists who monitor the PRS radiation delivery, both shielded behind a lead screen.
There have been 60 IORT treatments in the TARGIT protocol at the Middlesex so far (2005) and another 50 patients have consented to this treatment previously.

1.5 Requirements for accurate PRS400 treatments

The PRS is used clinically in the interstitial radiotherapy of solid tumours. This requires the insertion of the bare probe of the PRS directly into the tumour site. Furthermore, the PRS is also used in the intraoperative radiotherapy of tumour cavities formed when lumpectomies are performed. Spherical applicators of varying diameter (1.5-5.0 cm) are attached to the PRS so that the end of the tip of the probe rests at the centre of each applicator. These applicators are used to conform the tumour volume and ensure isotropic irradiation to the tumour wall. The applicators are made of a special resin of low Z material (not disclosed by the manufacturer for propriety reasons) which does not cause considerable distortions in the dose distribution from the device. Nevertheless, the construction characteristics of the applicators do add some degree of perturbation to the dose distribution with respect to the bare probe. This leads to a discrepancy in the absolute PRS output measurement of between 5% and 10% across the range of the applicators (Ebert and Carruthers 2003).
In the case of the interstitial radiotherapy treatments, the PRS probe is inserted into the brain aided by a stereotactic frame attached to the head (Cosgrove *et al* 1996). A CT system employs landmarks to register the frame on the image and the coordinates of the tumour with respect to the head frame are computed using dedicated software. Affixing the PRS onto the frame and applying the specified

coordinates allows accurate placement of the PRS directly into the core of the tumour to within 0.4 mm ± 0.2 mm (Karger *et al*, 2003). Biopsy needles are employed to extract a sample of the tumour in order to confirm malignancy, thereby providing tumour location. The PRS probe is inserted along the biopsy track and radiation delivered. In hospital where in-theatre CT systems exist (primarily in the USA) the image of the PRS whilst inserted in the tumour can be visualised. This however, is not necessarily very helpful as the last 2 cm of the PRS drift tube is made of a thin Beryllium window which is transparent to x-ray photons. This results in an uncertainty in the accurate location of the PRS, as extrapolation is required to compute the end of the probe. The gold metal target however, may sometimes be visible on CT image (at an increased x-ray tube current, mAs).

For PRS intraoperative radiotherapy, localisation of the PRS and confirmation of the tumour site is not applicable. The pathological findings of the tumour have already been established and the patient undergoes wide local excision of the lump. The cavity and its orientation, as formed by the excision, are visible to the surgeon and conformation of the tumour cavity is performed using the appropriate size applicator. The tissue is sutured around the spherical applicator using a "purse" string, allowing the tumour margins to be encompassed or wrapped around the applicator. Confirmation of the position of the PRS is recorded in the treatment logbook as the distance measured from the edge of the applicator to the thorax, the pectoral muscle and the skin. In the TARGIT protocol, in vivo dosimetry is performed by the placement of small capillary tubes containing an array of TLD (LiF) crystals. Their respective distance from the applicator face is recorded and the TLDs are read out post-operatively. The TLD results, together with the physicist's checklist during the IORT treatment, are kept in the patient record. Furthermore, the PRS console provides constant monitoring of the IRM rate (every 10 seconds), and the total treatment delivery record (treatment ID) is stored locally in the console's processor. The gantry that the PRS system is affixed to enables the insertion of the probe into the patient. Positional inaccuracies in the implementation of the gantry cannot be accurately assessed. Problems arising from patient movement resulting in positional inaccuracies and thus treatment discrepancies are not encountered in IORT since the patient is

under general anaesthesia resulting in minimal motion, as stated previously. Conformation of the PRS to the tumour cavity is performed using the spherical applicators. The tumour walls come in contact with the external edges of the applicators (conformation) and are fixed by stitching the tissue onto the applicator, as discussed previously. In this way, any motion due to the breathing of the patient results in minute motion of the conformed applicator. Since the whole applicator consequently shifts together (albeit by a minute fraction) with the stitched tissue around it, there is no need for further patient motion considerations.

1.5.1 Effects upon treatment outcomes and success

Failure of PRS interstitial treatment has so far proved to be a rarity. The stability of the PRS (over the past five years) in IORT treatments at Middlesex Hospital has been very constant and the ease of the IORT technique has indeed been a revelation. The PRS x-ray system must be handled with care, as bending the probe has caused major concern. In the eventuality of the probe bending (caused by human error), the PRS control console performs a diagnostic test of the system prior to treatment delivery to check the expected output. If this is out of range then the system flags up an error message and the treatment is paused. If the bending of the probe is minor, i.e. not visible to the human eye, then straightening of the probe can take place in-situ and the treatment may be salvaged. If, however, the bending is significant, then careful straightening and re-commissioning of the system is required and thus treatment has to be aborted. The only available means of checking for correct radiation delivery is the rate monitor internal to the PRS and any major fluctuation (>10%) results in treatment failure. Monitoring of the treatment is therefore based solely on the internal photon counter. Failure of the IRM has never been reported so far and constant checks on the PRS support the fact that the IRM performance is very stable.

Ebert *et al* (2003) investigated the radiation risk to the distal rib bone and made comparisons with rib doses in EBRT. They showed the rib dose to be minimal due to the rapid fall-off of the PRS radiation dose with radial distance. However, in

the case of deep-seated tumours, or alternatively in the case of small-breasted, low-weight women, this problem needs to be carefully addressed. The TLD dosimetry protocol employed in TARGIT requires the insertion of two TLD crystals. This is the only physical means for dosimetry checks during the IORT treatment. Uncertainty in dose delivery during TARGIT treatments is yet to be quantified by a multi-centred dosimetry study (Ebert *et al* 2003). At present a clinical treatment planning system (TPS) dedicated to the PRS treatments is not available. One of the major obstacles in IORT is the lack of pre-knowledge of the tumour cavity, i.e. before the actual tumour resection. The dosimetry of the PRS is checked using the water tank for all applicator sizes. In this way, the treatment delivery time is pre-calculated and the system is switched on for the time required to deliver the dose prescribed (5Gy at 10cm from the edge of the applicator) for a specific applicator size, i.e. depending on the excised tumour size. The TLD protocol indicates whether dose delivery had been successful retrospectively, i.e. after the actual treatment has been delivered. The drive for real time dose monitoring stems from the need for precise knowledge of the position of the tip of the PRS probe with respect to critical anatomical structures.
This thesis looks at an alternative way of checking the PRS dosimetry during the treatment by employing the PRS's own radiation field.

1.6 Proposed new in-vivo PECT system and its advantages

It has been shown that the radiation output of the PRS is near isotropic about the tip of the drift tube, allowing lesions and tumour cavities to be irradiated interstitially, however not all photons stop in the tumour and there is a reasonable flux escaping the body. The new proposed in-vivo location system makes use of this fact and explores the idea of imaging the PRS whilst buried in the body by utilising its own radiation field. A portable detection system could be devised to image the PRS source. Such a system would behave as an Emission Computed Tomography (ECT) unit, imaging a point x-ray source rather than a perfused radionuclide (e.g. $^{99}Tc^{m}$) which has been injected into the patient intravenously.

The fact that the PRS is transported to the operating theatres and is used as a radio-surgical tool means that the ECT procedure needs to be carried out in-situ. This is effectively portal imaging using ECT to form the images, and hence is called *Portal ECT (PECT)*. Nevertheless, localisation of the PRS in the body is not the only aim of this imaging procedure; the motivation for this project is to extract both positional and dosimetric information for the PRS from the resulting emission images.

The first goal is to design an appropriate PECT imaging system that will produce images that carry localisation information. It is hoped that extraction of the dosimetric information could then be performed directly from these PECT images. Localisation information can greatly assist in the mapping of the dose deposition of the PRS photons in the body. This requires employment of dose calculation techniques by means of both physical measurements and theoretical predictions arising from Monte Carlo simulations. Monte Carlo modelling has been widely used in the field of radiotherapy for verification purposes of treatment planning systems (Takahashi *et al* 2003). Modelling of a number of brachytherapy seeds has been carried out using Monte Carlo in order to calculate radial dose functions (Mainegra-Hing *et al* 2003, Ballester *et al* 2004) and Monte Carlo modelling has proved essential in determining dose measurements in the vicinity of brachytherapy sources where large dose gradients yield uncertainties in the physical measurement (Ballester *et al* 2001, Pérez-Calatayud *et al* 2005).

The resulting images do not need to carry important anatomical information and thus do not have to be analysed and processed in the usual medical imaging manner. This project will involve the production of images from the PRS that will allow the user to pinpoint the probe in the patient in a time-efficient and reproducible way. The acquisition of the image, its reconstruction and the resulting dosimetric information extraction may eventually be carried out on-line, providing the physicist with real-time monitoring of the dose delivery. Of equal importance, images and the resulting dose calculations will allow for post-treatment verification of the delivered dose and can be stored in the patient's records. In the eventuality of tumour recurrence at the same or another quadrant of the breast (another primary site) in patients that have already undergone IORT, oncologists will have to refer to the previous treatment record in order to assess the patient's tolerance for further irradiation of the same breast.

Recapitulating, the PECT imaging system proposes to investigate whether the position of the PRS probe could be located by utilising the radiation output of the source. The PRS buried in the body acts as the emitting source and thus a detection system outside it could be employed to localise the PRS by forming an image of photons escaping the body. This is in essence a portal imaging task, similar to the techniques employed in EBRT.

1.7 Scope of the Project

The hypothesis of this project is to explore the possibility of utilising the PRS's own radiation field to localise the probe while the PRS is in use, i.e. during the actual treatment. This technique could be regarded as a special case of Emission Computed Tomography (ECT), involving a point x-ray source rather than a perfused radionuclide (e.g. $^{99}Tc^{m}$) injected into the patient intravenously. The resulting images will not need to be of diagnostic quality. However, they must contain sufficient information to allow localisation of the PRS source with respect to existing or implanted landmarks. The work will take into consideration the use of single photon energy emitters as well. This will assist in understanding the scattering events that would otherwise be impossible to detect on a polychromatic x-ray source such as the PRS. In addition, investigation of the response of realistic mono-energetic BT sources can also be carried out.

Localising the probe is not the only goal of this work. The intensity map generated by the emission image can provide additional information to source localisation. The distribution of the photon intensities about the tip of the probe can also provide information on the dosimetry of the system. This arises form the fact that the energy deposition of the PRS system is extremely localised due to the low photon energy nature of the system, i.e. about the tip of the probe. An image therefore, of the photon flux escaping the object (e.g. the breast) can be directly related to the distribution of energy deposited in the breast. In this way, the resulting image can indicate the way in which dose is being deposited and thus allow for monitoring of the radiation treatment.

Modelling of the experimental work by simulating the various detection parameters (detector, phantom, and source) allowed for the generation of theoretical images. Monte Carlo (MC) simulations can also be employed to perform computations on the dose deposition of the PRS photons. Calibration of the emitted or *escaped* photon image to the predicted dose map is proposed for the direct translation of the emission image to the dose map. The formulation of this relation of the intensity image to the energy deposition map (transform map) can allow for the extraction of dosimetric information. The collation of the localisation information with respect to anatomical markers together with the dosimetric information that arises from the images can set the basis of a real-time treatment planning system (TPS). This is a novel approach for real time quantification of the dose delivered during a PRS treatment. Provided that the emission image is produced in the first minutes of the treatment, monitoring of the treatment delivery could in theory be achieved allowing the user to intervene when necessary.

In summary, the images formed while the PRS is in operation could allow for real-time monitoring of the radiation delivery together with a post-treatment dose verification record.

Outline of the Thesis

The investigation and results performed during this research project are presented in this thesis in the following way:

- In chapter 2, the techniques that were employed in this project and the reason for their choice is discussed both in the design of the PECT source localisation system and in the PECT Transform Map derivation.
- In chapter 3, the PECT design is presented. The various components used and the reason for their implementation is discussed. The experimental PECT system is explained and the protocol that was followed for the investigation on the accuracy on source localisation (for both mono- and poly-energetic beams) is analysed. The MC modelling for both the spectral

and the dosimetric studies is presented and an argument for its purpose given.

- In chapter 4, the results on PECT source localisation precision are presented. The various image reconstruction techniques employed for the accurate source localisation of both types of beam are discussed. The idea of selective reconstruction is also presented. The effect of various scanning parameters on the localisation precision and an attempt to define the optimal settings of the PECT system are finally presented.
- In chapter 5, the results of the MC studies are presented. The rationale of a PECT transform map is discussed and its generation demonstrated. The result of the dosimetric studies and their correlation to measured data is shown. The significance of the transform map in the proposed design of a new PRS imaging verification system (with in-vivo dosimetry) is discussed.
- In chapter 6, a summary and the overall conclusions drawn from this research project are presented. The future directions of this work are discussed. Namely the clinical design of the PECT system and the possibility of a proposed treatment planning system (TPS) that will evolve from the implementation of the PECT system.

CHAPTER 2

Tools and Techniques employed in the thesis

2.1 Criteria for PRS400 self-source localisation.

As discussed in Chapter 1, the near-spherical radiation output of the PRS and its in-vivo capabilities both contribute towards rendering the system a brachytherapy tool. The output of the system can be regarded as a point source of x-radiation buried in the body. Devising imaging techniques in order to localise the PRS source by utilising its radiation output therefore requires careful consideration of the imaging modality chosen for the problem at hand. The PRS probe, inserted in the body for interstitial radiotherapy, and the consequent isotropic emission of photons about the tip of the probe can be regarded as an Emission Computerised Tomography (ECT) set-up. The correlation, however is somewhat crude, as the distinction between the PRS radiation output and that from typical radiotracers used in ECT needs to be addressed.

In ECT, gamma radiation emitting radioisotopes that are coupled to organ tracers are injected into the body intravenously. The radiation is therefore injected in the body in a solution, which is perfused by the targeted organ. This gives rise to a distribution of emitted photons across the organ under study rather than the point source radiation emission of the PRS. Furthermore, the PRS spectral output is a continuous spectrum (50kVp) instead of the single-energy emitted photons in ECT (Single Photon ECT- SPECT) e.g. 140 keV $^{99}Tc^{m}$ radionuclide. ECT images are used to assess the physiological function of organs by recording either the passage of the tracer or uptake of the tracer by the organ. In the use of the PRS there is no need for diagnostic information as mentioned before, however the

imaging techniques employed in ECT can be implemented to create a PRS image in an attempt to localise the source.

2.1.1 Basics of Computerised Tomography (CT)

Computerised Tomography (CT) is the general process of creating cross-sectional or tomographic images from projections (line integrals) of an object at multiple angles. The tomogram is effectively an image of a slice taken through a 3-D volume. Ideally it is free from the effect of intervening structures, thus providing a distinct improvement on the ability to visualise structures of interest when compared to planar radiographs.

There are two types of CT imaging modalities. These are defined by the position of the radiation source employed in the process of the imaging. In Transmission CT, commonly referred to as standard CT, x-rays external to the object traverse it from multiple angles of projection, while in Emission CT the source of radiation is internal to the object, as discussed earlier. In both forms of CT, the input projection data are line integrals or ray sums of some property, and the tomographic image is a representation of that property. In modern CT systems (4^{th} generation), rotation of the x-ray source around the patient, recorded on a ring of scintillation detectors, results in the production of a three dimensional density image of the part of the body exposed. This is accomplished by measuring the transmitted intensity of x-rays through the patient at different angles. Image reconstruction is then performed. This is the process of estimating an image from a set of angular projections. In practice there are a limited number of projections, or views, and a limited number of detector samples. In transmission CT, given a particular beam aperture of the x-ray fan beam (beam width), it is possible to calculate the minimum number of detector samples required to prevent distortion due to aliasing. This minimum is known as the Nyquist criterion (Webb 2002). This criterion states that if Δs is the beam width, then the maximum sampling distance is $\Delta s / 2$, or at least two samples per beam width are required. Regarding

the number of views required, the problem is not so straightforward. A generic rule states that the number of views required to obtain a given resolution in CT is (π D)/d where D is the field of view and d is the smallest object to be resolved (Naterrer 1986). This relation can be obtained either formally using sampling theory, or empirically by requiring that the distance between two central rays belonging to two adjacent projection (i.e. two adjacent angular samples), is equal to the spacing between the rays (Todd Pokropek 2003).

The goal of CT imaging is to derive the unknown attenuation coefficients of the object based only on the set of projection functions. Several reconstruction techniques exist to accomplish this task. The most commonly employed algorithms are:

- Filtered Backprojection technique (FBP)
- Iterative Reconstruction technique (IRT)

Of these, the filtered backprojection (FBP) technique is used on the majority of CT image processing machines. In FBP, the inverse problem is addressed by the implementation of the Radon Transform function (Naterrer 1999). The measurements obtained at each projection are projected back along the line of projection. The resulting transformed projections are applied with a pre-weighted factor (filtering) and are then back-projected to produce the end result. The analytic solution to the FBP image reconstruction problem assumes that the data collected from various angles is consistent (Muehllehner and Hamisch 1999). In transmission CT, this condition is fulfilled when data is of good statistical quality. FBP implements differently shaped filters, depending on the nature of the study, in order to reduce the noise incorporated, thus optimising the resulting images (Van Laere *et al* 2001, Gilland *et al* 1988). The speed of accuracy and simplicity of FBP techniques have lead to their widespread use in CT. However, they are not easily implementable in cases where the set of measured line integrals do not adequately sample the object being imaged (Ollinger 1990).

The need to address the problem associated with poor counting statistics has led to the development of iterative reconstruction techniques IRT (Bruyant 2002). In

these techniques, the reconstruction algorithm iteratively updates an estimate of the image until the ray sums or projection measurements computed from the image match completely the input measurements. This offers an advantage over FBP in allowing direct modelling of the physical factors affecting poor statistical data (Gilland *et al* 1997). While the benefit of IRT has been appreciated for many years (Shepp and Vardi 1982, Hudson and Larkin 1994, Meikle and Hutton 1994) in a non-clinical environment, the development of faster computers has now allowed for the routine application of IRT in a clinical setting. There are a variety of commercial IRT algorithms, differing in the manner in which the projections are computed, in the type of error correction performed and finally in the order in which the corrections are made (Matsumoto *et al* 2003).

2.1.2 Principles of Emission Computerised Tomography (ECT)

ECT is the medical imaging modality that provides a qualitative and quantitative assessment of the volume distribution of biologically significant radiotracers after injection into the human body. The solution injected containing the radiopharmaceutical passes via the blood circulatory system and is deposited in the organ to be examined. Three-dimensional ECT is a process that allows the rotation of photon-sensitive cameras around the patient to record the distribution of the organ-specific emitted photons. ECT is subdivided into two categories depending on the nature of the radiation emitter used:

Single Photon ECT (SPECT) involves gamma (γ) emitting radiation sources (^{123}I, ^{67}Ga) and Positron Emission Tomography (PET) involves positron (β^+) emitters (^{18}F, ^{82}Rb). Positrons undergoing annihilation with electrons produce two photons (511 keV) travelling at opposite directions. Formation of a three dimensional representation of the organ is achieved by taking multiple images from different directions in both PET and SPECT. The photon energy range in PET is far greater than the PRS's x-ray output and therefore falls out of the scope of this work. In SPECT, the distribution of the emitted photons is recorded on the cameras as

shown in Figure 2.1. The rotation of the cameras around the targeted organ allows data acquisition from multiple angles (projections) over a short time. This is necessary as all injected emitters suffer radioactive decay. The goal of SPECT is to obtain information from the emitting organ in terms of blood volume, flow and uptake of the organ. A uniform distribution of photons in the target organ generally indicates normal uptake of the radiopharmaceutical. Contrary to that, a region with abnormally higher uptake usually defines a diseased lesion within that organ.

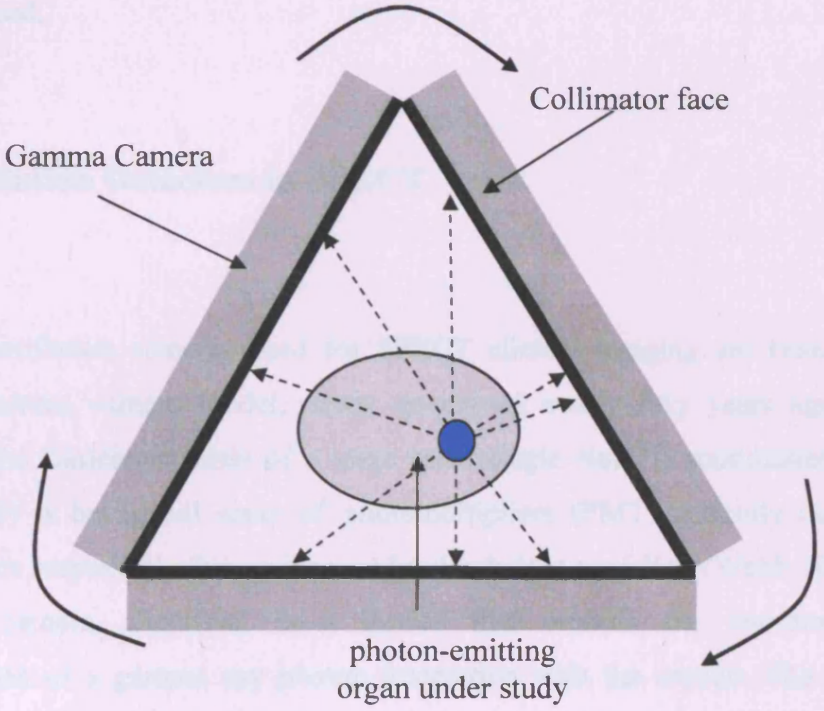

Figure 2.1 Typical ECT clinical set-up. The cameras are focused on the organ (blue circle) allowing projections to be acquired in a 360° rotation.

New advances in SPECT allow for the monitoring of changes in the organ activity distribution during acquisition. This is known as dynamic dSPECT, and is usually undertaken to assess physiological function of various organs such as the heart or

renal system (Pohle 2004, Blondel *et al* 2002, Khare *et al* 2001). Image reconstruction in SPECT is nowadays most commonly performed using IRT. The uptake of the radiotracer by the organ, in conjunction with the small tracer quantity (thus low-activity of the emitter), limits the photon-counting statistics in SPECT compared to transmission CT. Poor statistical data results in streak artefact formation in the resulting image when FBP is employed. In the case of functional SPECT studies, the problem of poor statistics becomes greater during the progressive uptake of the tracer by the organ. In general, SPECT images are of inferior spatial resolution to other imaging modalities in Radiology. Nevertheless, in the objective assessment and measurement of physiological processes, the ability of SPECT to produce images that provide quantitative analysis is unsurpassed.

2.2 Radiation Detectors in SPECT

Most scintillation cameras used for SPECT clinical imaging are based on the Anger gamma camera model, firstly conceived nearly fifty years ago (Anger 1958). The camera consists of a large area, single NaI(Tl) scintillation crystal, viewed by a hexagonal array of photomultipliers (PMT) optically coupled to electronics responsible for position and pulse-height encoding (Webb 2002). The gamma camera, therefore, is a device that records the two-dimensional coordinates of a gamma ray photon interaction with the crystal. The image is formed by the accumulation of many such events over the exposure time. All SPECT systems in Nuclear Medicine use mechanical collimation to form an image of the radioisotope distribution on the face of the gamma camera. These collimators impose a hard physical constraint that couples detection sensitivity and spatial resolution in an inverse relationship. There is a range of general performance criteria for the choice of collimators employed depending on the organ study performed. There have been a number of different collimator designs in the last ten years, however the detection sensitivity/spatial resolution inverse

relationship has not considerably improved thus there is now a motivation towards the development of electronically collimated gamma cameras (Compton cameras) that can provide information about the incoming photons via their Compton interaction (Meier *et al* 2002, Singh and Brechner 1990). Various scintillation materials are in use for both SPECT and PET (CsI, BGO, GSO, and LSO), at various orientations and sizes according to their intended use. Currently there is a strong impetus towards replacing scintillators with semiconductor detection materials which offers superior energy resolution (Mestais *et al* 2001, Chambron *et al* 2000, Takayama *et al* 2000,). Semiconductors such as CdTe and CdZnTe have been shown to provide superior intrinsic spatial resolution. Furthermore, segmentation of the detectors offers superior contrast resolution compared to the Anger camera (Eisen *et al* 2004, Ogawa and Ohno 2003). Segmentation of the detector material into smaller pixel sizes provides better spatial resolution as position sensitivity increases. Growing emphasis, therefore, in modern SPECT detector development is given towards miniaturisation of the detectors and increasing the speed of read-out electronic, in an effort to decrease the overall examination times by maximising detector efficiency.

2.2.1 Selection of imaging detector systems for PRS400 Image Acquisition.

There are two types of imaging detectors employed in medical imaging. The type of the detector employed is based on the mode (or principle) of photon detection. There are therefore, two types of photon acquisition modes; the photon counting mode and the photon integration mode. The photon counting mode allows charges produced by the photon interactions with the detection material to be recorded if they occur above a given threshold. Such detectors can provide information about the incident photon energy depending on the energy resolving power of the detective material (e.g. NaI, CsI, CZT, HPGe etc). The integration mode relies on photon acquisition by every pixel of the detective material. This can usually be

achieved by direct or indirect photon interaction (i.e., in the case of CCD cameras, a scintillator crystal is used to convert ionising radiation to optical photons which are then converted into electrical charge in the camera).

Integration mode detectors provide spatial information as the resulting image is formed by the distribution of charges over the whole area of the pixel array. The requirements of photon-counting detection systems are often quoted in terms of energy resolution and detection quantum efficiency (DQE). The former requirement specifies the ability of the detector to resolve the energy of any incoming photon while the latter defines the fraction of the detected photons to the emitted ones. Furthermore, spatial resolution of a photon-counting detection system is often related to the structure design of the detector material (i.e. single or pixelated crystal). For a single crystal, the spatial resolving power is strongly dependent on the collimator system employed. The function of the collimator is to allow distinctive radiation passage to the detector material and the resulting resolution of the imaging system relies heavily on the acceptance angle of the collimator system. The importance of the collimation in achieving high spatial resolution will be discussed in greater depth in Chapter 4.

The need for energy resolving power when poly-energetic sources like the PRS are involved may not be of utmost importance. This is because the continuous PRS x-ray spectrum incorporates both primary and secondary (scattered) photons and distinction between the two is not possible. DQE may again not prove to be a stringent requirement, as the intense nature of the PRS output (x-ray therapeutic source) may compensate for low efficiency detectors. However, spatial resolution is an important issue in the choice of the most appropriate detection system. Clinical localisation of the PRS source when embedded in tissue requires a detection system with enhanced spatial resolution, able to form images in relative short times. As it is intended to attempt to localise the PRS source during the treatment, time for image formation could become crucial, as the information in that image will indicate quality assurance of the beam during the treatment. In context, the detection requirements for PRS localisation are as follows:

- Spatial Resolution-very important
- On-Line image formation-very important
- Energy resolution-not so important
- Detector Quantum Efficiency-not so important
- Size and cost-could become important

Various detectors could be employed for the ECT image acquisition of the PRS x-ray output. Scintillation crystals coupled to either PMTs or to CCD cameras could be considered. However, the scope of this work includes the use of mono-energetic sources as well as the PRS source. The reason for this, as stated previously, is to investigate the scattering events taking place within the test phantoms. In this way, the response to a realistic mono-energetic BT source could also be investigated. Investigation, therefore, of the scatter events implies that a superior energy resolving detector is required for accurate distinction between the primary and secondary (scattered) radiation. A superior energy resolving detector is not necessary for acquisition of the continuous PRS spectra as stated previously, however it could be used to simulate other detection systems. Employing a high energy resolving detector and acquiring spectra with it could allow the collected data to be manipulated so that detectors of inferior energy resolution can be simulated. In this way, by acquiring one set of data, the response of other detector systems with inferior capabilities can be deduced, thus assessing their practicality for PRS image acquisition. A list of the possible imaging detection systems that could be employed for this work is given in Table 2.1. A high purity germanium (p-Type HPGe, Ortec) detector was chosen for this work, since it can provide the means to simulate other detection set-ups. The detector is closely coupled to a preamplifier (Tennelec Corp., Oak Ridge, TN 47831), a spectroscopy amplifier (EG&G Ortec, Oak Ridge, TN 47831), and a PC-based multi-channel analyser (Maestro-32 MCA Emulator). The crystal has an active area of 36 mm diameter and a depth of 10 mm. The detector cool-down time is six hours. The major advantage of this detector is its superior energy resolving power over most common radiation detection systems. Energy resolution of the detector

using a standard reference ^{241}Am source was measured to be 0.5 keV FWHM at the 59.5 keV peak. The high energy resolving capability of this detector system means that it can be used to simulate a range of different detectors with inferior energy resolving power. Integration of different energy windows of the resulting spectra allows for other detection systems to be simulated. For example, if radiographic film, which has no energy resolving power, were to be simulated, the whole spectrum would have to be integrated. Other detectors with better energy resolution could be simulated by selecting an appropriate energy window for integration, as shown in Figure 2.2.

Detector	Detection type	(D)QE	Dynamic range	Energy Resolution	Spatial Resolution	Field Size (cm^2)	Reference
CdZnTe	Direct	0.1	Photon counting	3-5%	330 μm	1	Mainprize et al 2002
HPGe	Direct	~100%	Photon counting	0.5-1%	Defined by collimator	Size of crystal	Knoll 1988
NaI:Tl	Indirect	0.95 @ 140 keV	Photon counting	8-10%	Defined by collimator	Size of crystal	Van Eijk 2002
CCD	Indirect	0.25	10^4	n/a	7-100μm	>1	Gruner et al 2002
AMFPI	Direct	>0.9	10^4	n/a	100μm	1600	Yaffe and Rowlands 1997
Si PAD	Direct	<0.3	10^5	n/a	50μm	5	Wermes et al 2004
APD	Indirect	0.8	10^{11}	n/a	200μm	Size of pixel	Knoll 1988

Table 2.1 Radiation detectors employed in Medical Imaging

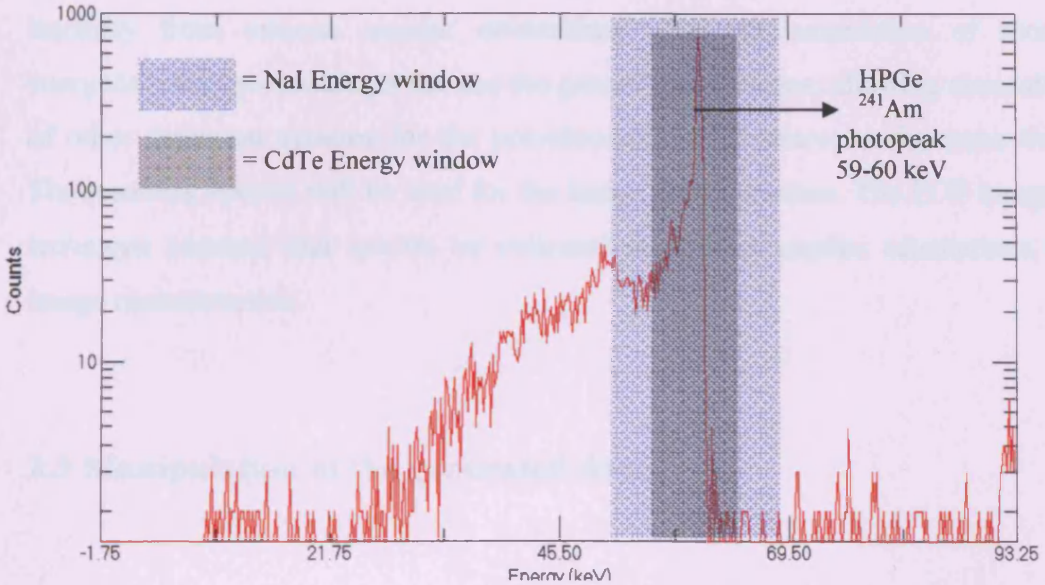

Figure 2.2 Typical ^{241}Am spectrum (source in phantom) as recorded on the germanium detector (HPGe). The spectrum of a high-energy resolving detector can be used to simulate other detector energy resolving responses by integrating over wider energy windows across the ^{241}Am photopeak.

Typically, a gamma camera (scintillation counter) has energy resolution of 8-10% and therefore is often used during a nuclear medicine investigation with an energy window of 20% centred on the photopeak. This can be simulated from the acquired HPGe spectrum by integrating an appropriate energy window. Similarly, a 10% energy window across the 59.5 keV peak will simulate a semiconductor detector at room temperature such as CZT [energy resolution of about 0.9 keV FWHM at 59.5 keV (Amptek Inc, USA)]. In the implementation of single energy emitters, distinction between primary and secondary (scattered) radiation is viable. An excellent energy-resolving detector will greatly contribute in accurate distinction of the recorded radiation. This can clearly be demonstrated in Figure 2.2 (the 59.5 keV energy of the ^{241}Am primary photons is denoted as the sharp peak on the spectrum). The implementation of the HPGe detector enables

therefore the accurate distinction of the emitted radiation. This assists in a better understanding of the scattering interactions occurring by recording the emitted intensity from various angular orientations. The implementation of mono-energetic sources encourages the use the germanium detector, allowing simulation of other detection systems for the polychromatic PRS source at the same time. The resulting spectra will be used for the image reconstruction. The ECT imaging technique requires that spectra be collected at various angular orientations for image reconstruction.

2.3 Manipulation of the generated data

Spectra from the PRS source inserted in an object that simulates human tissue (phantom) were recorded in a typical ECT manner. Synchronous data acquisition resulted in an array of continuous spectra being formed. The Data generated was used in the reconstruction of images. The primary goal of the image generation was an attempt to localise the source in the image. Images from various simulated detection systems were formed and assessed.

The scope of this work looks at extracting further information from the generated image, relating its intensity directly to the PRS's energy deposition (dose) distribution within the object. Photons escaping the phantom are recorded and thus an image of the emitted photon intensity is generated. Relating the intensity image to the dose distribution map is not a straightforward process.

Monte Carlo (MC) modelling techniques were employed to assist in this problem. MC modelling has been widely used in the field of radiotherapy for verification of experimental findings. MC codes are used to model photon transport for brachytherapy dose calculations and are able to support detailed 3D modelling of source geometry (Medich and Munro 2003, Rivard 2002, Das 1996, Williamson 1987). In general the AAPM TG-43 recommends MC investigators to "utilise well-benchmarked codes for brachytherapy dosimetry studies intended to produce reference quality dose-rate distributions for clinical use". In the context of this

work, MC modelling was chosen for the generation of the theoretical images as well as the dose distribution around the PRS source. Evidence has shown that MC dose calculations can offer some advantages over conventional dose computation in complex geometries (e.g. in the case of IMRT) or in regions close to the source vicinity (e.g. in the case of BT) (Laub 2000). The close correlation of measured to predicted findings (to within 1%) has enabled the accurate calibration of predicted PECT images to the PRS dose distribution (or dose map) to be carried out under the same conditions with an increased degree of confidence (Fragoso *et al* 2002).
Data generated in this work was therefore divided into two parts:

- Experimental or measured data arising from physical measurements using HPGe
- Modelled or theoretical data arising from the Monte Carlo simulations.

The experimental data was used to generate images from the measured projections while the Monte Carlo model generated the theoretical data. Manipulating both types of data meant that a software package able to handle both tasks was necessary. Reconstruction of the images based on the measured and the theoretical data had to be performed in the same manner so that direct comparison of the results could be accurately made. The software package able to perform this task, and hence employed, was IDL (Interactive Data Language, RSI). IDL software has the ability to manipulate many types of data format. It was primarily employed for the tomographic reconstructions of the experimental spectra. Manipulation of the raw data to simulate other detection set-ups was performed through IDL, allowing quick inspection of the resulting images. The theoretical data was also handled by IDL in order to replicate the experimental images. Monte Carlo generated spectra were also manipulated by IDL to produce the images, so that they can be directly compared to the measured ones. Sorting of the modelled spectra into corresponding energy bins according to pre-defined energy resolution criteria (to simulate different detector responses) was also performed in

IDL (Erlandson 2002). Furthermore, Monte Carlo generated data on the dosimetry of the PRS, i.e. the dose deposition distribution, was also handled by IDL. The software package proved very useful (ease of use and computational speed) in the image reconstruction task. A number of IDL image analysis tools available to the user allowed accurate localisation investigation. Moreover, these tools allowed for accurate inspection of the raw image data (sinograms), and extraction of data at regions of interest (i.e. at the vicinity of the tip of the PRS probe). The way in which the various data generated in this work was handled is shown in Figure 2.3. HPGe and MC generated spectra are ported into IDL for image reconstruction. Manipulation of the generated images performed in IDL on both types of generated data, allowing accurate computations to be made so that direct comparison and cross calibration of the two can be achieved. The relation of the emission image to the MC predicted PRS dose distribution can therefore be derived. Finally, this relation of the emission PRS image to the PRS dose map allowed for the transformation of the former to the latter therefore providing direct dosimetric information for the PRS probe as derived from its own emission map. This is in essence the main goal of this work as it allows direct correlation of the emitted image to the dose deposition of the PRS during a nominal radiotherapy treatment.

2.4 Monte Carlo Modelling

Monte Carlo (MC) modelling is a software analysis tool available to researchers that simulates a given experimental scenario and predicts its theoretical response. MC modelling is widely used for the accurate computation of the physical interactions of ionising radiation with matter. The availability of accurate photon cross-section libraries in conjunction with recent advances in computer processing power has made MC modelling an important tool in the dose calculation formalism endorsed by ICWG (1990) and AAPM (1995). There is a range of

different platforms available for the simulation of photon-electron transfer in matter (GEANT, MCNP, ITS, EGS).

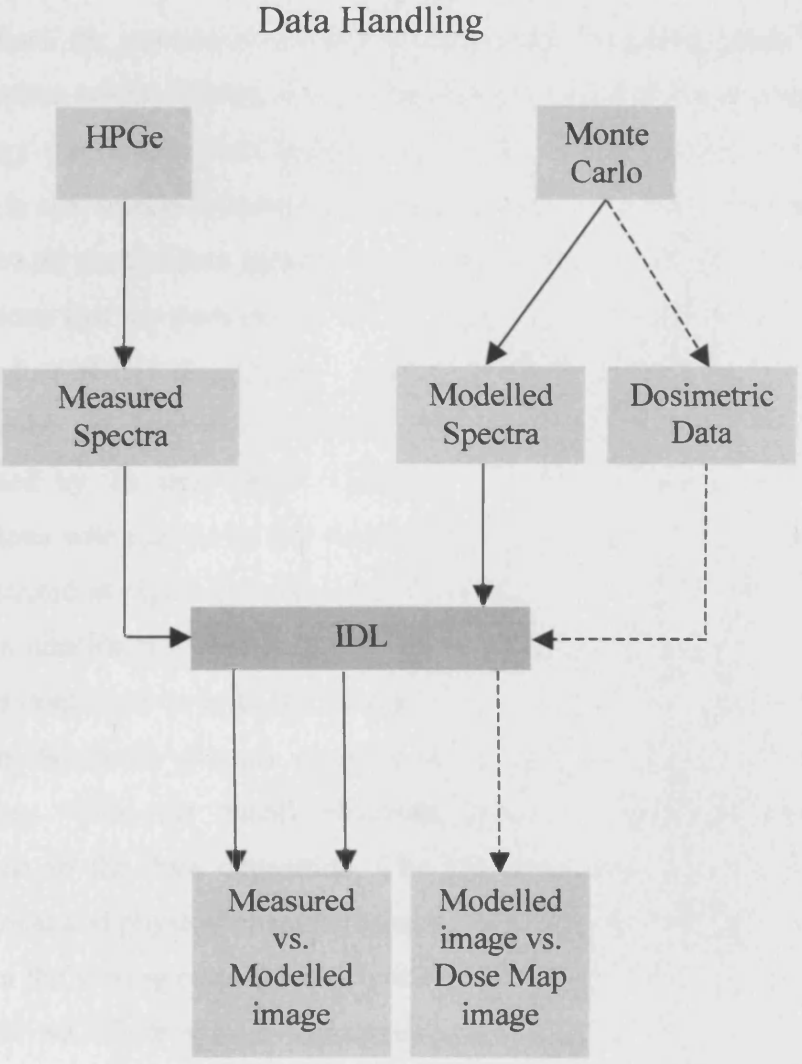

Figure 2.3 Flow chart of the way in which the generated data is processed. IDL was implemented to carry out this task as generated images had to be compared under similar conditions.

Not all MC codes simulate the different interactions in the same manner; often different photon cross-section libraries are employed. The photon MC simulation is in general performed in four steps and is effectively choosing a type of interaction suitable for the energy of the photon at hand randomly according to the simulations photon cross-section tables. The choice of the distance the photon

travels before the next interaction is also chosen randomly, as is the transport to the interaction site taking into consideration the physical dimensions of the geometry coded. The type of the interaction mechanism is also randomly selected and follows the probability of such an interaction occurring given by the photo cross-section tables. Finally, the choice of the outcome of the interaction in terms of energy transference and angular deviation (scattering angle) of the primary particle is also selected according to the photon cross sections. The MC code takes into account the incident particle energy and computes all the possible physical interactions that are permissible before randomly selecting a type of interaction. The product of this interaction is also followed down until its catastrophic end. The number of secondary particles that are generated and followed can be predefined by the user (stack number). The principal mechanisms of photon interactions with matter for the energy range of interest in this work (0-60 keV) are illustrated in Figure 2.4. The various interactions produce secondary particles, which in turn interact with matter to add up to the overall energy deposition. All particles contribute to both the image formation and dose deposition within the phantom. Scattered photons escaping the object contribute to emission image formation, while the recoil electrons generated by Compton interactions contribute to the dose deposition. The MC code has to be structured for the geometrical and physical characteristics of the materials employed, along with the result, or the scoring output, of the type of information that is requested.

The EGS MC Code system was employed for the modelling part of this work. EGS was originally developed at the Stanford Linear Acceleration Centre (SLAC), and was designed for the simulation of high-energy particles (Ford and Nelson 1978). It was later developed and modified to suit other applications. EGSnrc; developed by the National Research Council of Canada, was released in 2000 by Kawrakov and Rogers, and was the platform employed for the MC modelling task in this work. MC simulations were employed for the modelling of the source localisation experimental set-up (^{241}Am and PRS), as well as the dosimetric studies of the PRS source in both water and a phantom. The photon energy range and the kinetic energy range of the charged particles in EGSnrc lies between 1.0 keV and several hundred GeV. The code was structured using the

EGSnrc generic user code (GenUC) on a Linux machine. This was designed at the Institute of Cancer Research, Royal Marsden Hospital by Fragoso *et al* (2003).

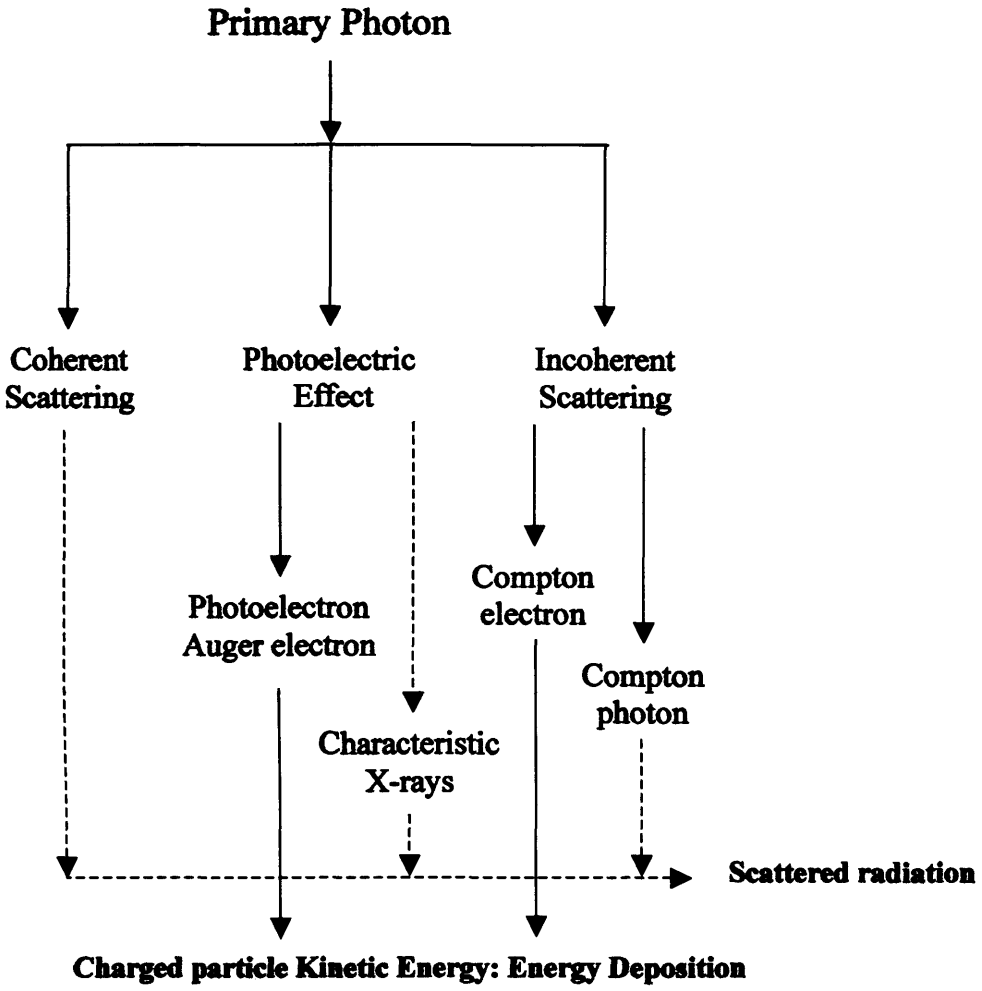

Figure 2.4 The principle mechanisms of interactions of photons at the energy range of interest in this work. The MC model computes and records the history of each photon and its consequent "by products".

The geometry and scoring modules of this package allow a variety of different geometry set-ups to be chosen with increased scoring capabilities. GenUC

provides a number of elemental volumes to be inserted in the geometry module of the structured code (spherical, cylindrical, parallelepiped). The output of the spectral results was analysed using Physics Analysis Workstation (PAW, CERN), and a binary format output file was ported into IDL for image reconstruction of the theoretical images. The dosimetric simulation studies were undertaken in order to compute the dose deposition of the PRS in a given medium. The code used for this work was BEAMnrc, specially developed for radiotherapy physics computations. The code was kindly provided by J. Seco (ICR Royal Marsden Hospital) and was accordingly adapted and optimised for the application of this research work

The geometry and scoring module in BEAMnrc are different to GenUC, but the computational processes and the photon cross-section databases remain the same. BEAMnrc provided information about the distribution of energy deposition by the PRS in a given medium and the resulting output file was again manipulated by IDL. This was achieved by scoring the energy deposited in a pre-specified elemental volume (voxel) per unit particle, averaged over the total number of photon histories. The distribution of the energy deposition therefore provides the theoretical dose map of the PRS in a given medium. The dose distribution predicted by the MC model can be calibrated against the emission image to give rise to the PECT Transform Map. This is achieved in IDL, as discussed previously. The way in which the MC generated data is handled is shown in Figure 2.5. IDL can generate visually the emitted intensity distribution (emission image) and the dose intensity distribution. Therefore, the relationship (transformation) of emission intensity to the dose intensity can therefore be computed.

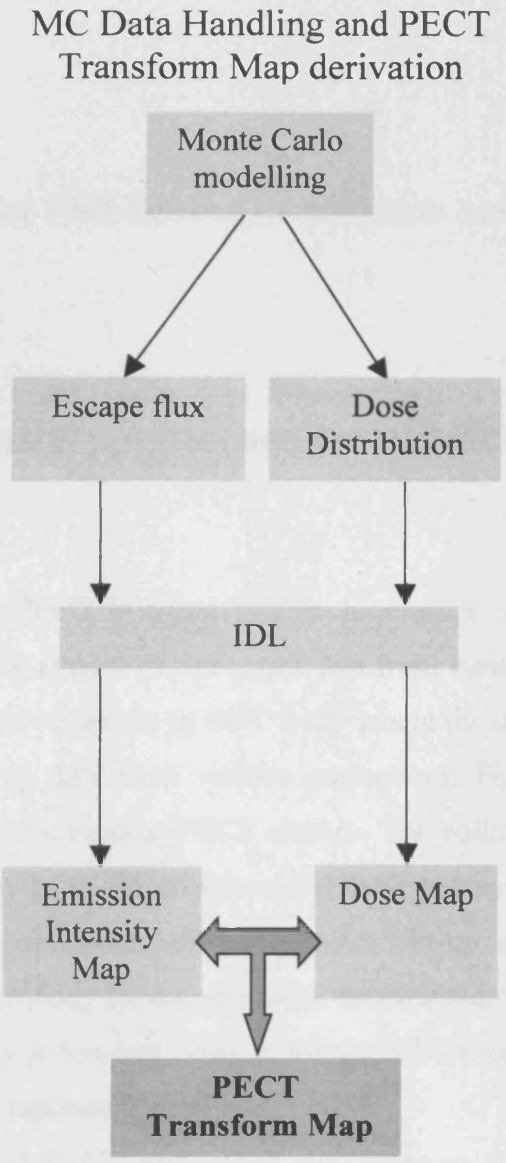

Figure 2.5 Flow chart of the techniques employed leading to the PECT transform map. Direct relation of the distribution of emitted photon intensity to the dose intensity distribution is achievable through IDL.

CHAPTER 3

Methodology for PRS Source Localisation and Dose Verification

3.1 In-vitro evaluation system and the choice of components

The design of the PECT imaging system requires a photon detection system coupled to a scanning system that acquires data from various angular projections. Clinically, this would resemble an ECT study where the detector is rotated around the patient, acquiring data from various projections. Figure 3.1 shows a rough schematic of a possible clinical PECT system. The collimated detector is rotated around the region of the PRS insertion and is focussed on the source plane.

The experimental simulation of the clinical set-up requires an object that replicates the human body (phantom) to be constructed. The whole experimental set-up is essentially a test-bed system for the PECT imaging system and will allow evaluation of inputted parameters.

During experimental PECT acquisition the phantom was rotated and scanned across the photon detection system. The detector for the PECT experimental work was a solid state Germanium detector (HPGe), employed for reasons explained in Chapter 2. Collimation of the detector face was achieved by using collimators with various acceptance angles. The design of the collimation system will be discussed in length later in this chapter. The PRS was not available for research work in the first phase of the project as it was still in clinical use at the Middlesex Hospital, UCLH. The system that this research project was performed on became available in 2003, once a newer version of the PRS became available for clinical use (TARGIT). The old system is still in use as a back up to the newer system, however it was released by the radiotherapy department for research purposes.

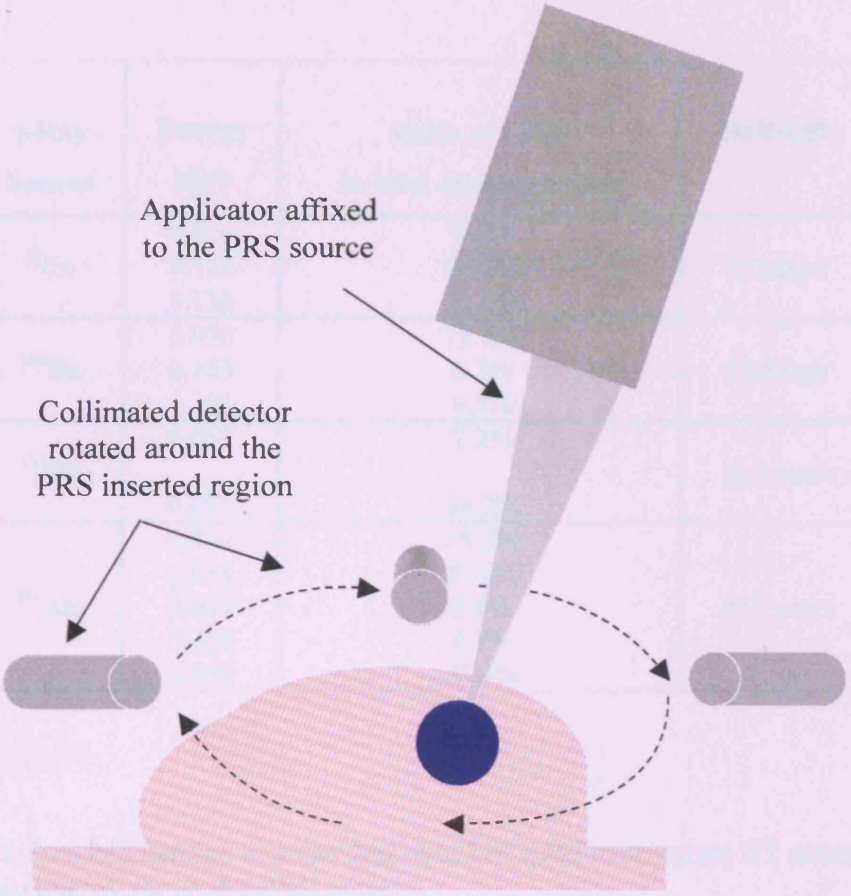

Figure 3.1 Schematic of a possible clinical PECT imaging system (not to scale).

The applicator set used in the IORT treatments was not available for research work as it is still in use as a back up to the clinical system and may be compromised by radiation damage.

The early stage of the PECT design employed the use of single energy gamma emitters. This choice was made on the grounds of simulating realistic BT sources, which are in general monochromatic. Furthermore, as discussed in the previous chapter, the energy resolving ability of the HPGe detector allows for accurate distinction between primary and secondary radiation. Therefore, the function of the PECT imaging system could be tested for future implementation of implanted BT source localisation. Taking this into account, several radioactive sources were considered. Table.2.1 presents possible radioactive sources that could be employed.

γ-Ray Source	Energy MeV	Ratio of γ rays to total disintegrations	Half-Life
^{57}Co	0.014 0.122 0.136	9.5% 85.5% 11.1%	272days
^{140}Ba	0.030 0.163 0.305	13.6% 6.2% 4.3%	12.8days
^{133}Ba	0.053 0.081	2.2% 34.2%	10.5 years
^{241}Am	0.014 0.018 0.021 0.026 0.059	13.5% 21.0% 5.0% 2.5% 35.3%	433 years

Table 3.1 Possible isotope sources that could be used to simulate BT sources at the photon energy range the PRS output.

For this work the choice of the source was governed by the sources available in the UCL Medical Physics Department. ^{241}Am (Amersham Int. Plc, UK) was chosen for this work. The predominating spectral output is at 59.5 keV (~35% abundance). The activity of the ^{241}Am source is 7400 MBq (200mCi). Typical photon output is 5.5×10^7 photons/sec per steradian. The source employed was enclosed in a metallic casing that allowed isotropic emanation of only the 59.5 keV photons; as the low energy gamma rays were stopped within the capsule. This implied that the source employed was effectively a point source of mono-energetic photons. For the purpose of this work, the choice of this source was ideal for the simulation of realistic brachytherapy sources, which are single energy emitters.

3.2 Phantom construction

A tissue equivalent (TE) phantom was constructed in order to simulate the patient in the laboratory. The design of the phantom was initially based on regular shape geometry (cylindrical). This simplistic approach to the clinical case meant that spurious results associated with anatomy irregularities can be initially avoided. Furthermore, the simplification of patient simulation in the shape of a regular geometry phantom has many advantages in the reconstruction and the modelling phase of the work.

3.2.1 Geometric Phantom

The phantom constructed for the preliminary work was made of Nylon-6/6 in a Perspex (acrylic) casing. Nylons have a polymer structure similar to a long protein. They are formed by condensation between the amino group ($-NH_2$) of one molecule and the carboxylic acid group (-COOH) of another molecule to form polyamides. Nylon-6/6 has the empirical chemical formula $(C_6H_{11}NO)_n$. Its density is 1130 kgm^{-3}. Acrylic has the empirical formula $(C_5H_8O_2)_n$ (Polymethylmethacrylate, PMMA). It is a clear, rigid thermoplastic that can be easily cast or moulded. Its density is 1170 kgm^{-3}. Both of these materials approximate to human tissue to within 20% at the range of diagnostic x-ray energies (10-100keV), as shown in Figure 3.2 (NIST Physical Reference Data) The phantom was initially designed to be homogenous, i.e. the whole of the inner phantom made of Nylon 6/6. The simulation of soft human tissue is achieved by this, however the effect of in-homogeneities, such as air-tissue interfaces and more realistically bone-tissue interfaces, cannot be simulated on the uniform homogeneous phantom. As the work progressed, the effect of phantom

heterogeneities was investigated with the insertion of other materials into the phantom to simulate other anatomical structures. These were inserted in the phantom in the form of Aluminium rods. Aluminium, with a density of 2700 kgm^{-3} approximates to within 25% to human bone for energies higher than 30 keV, as shown in Table 3.2. However, at lower energies the value of the Aluminium linear attenuation coefficient is higher than that of cortical bone, implying overestimation of bone attenuation.

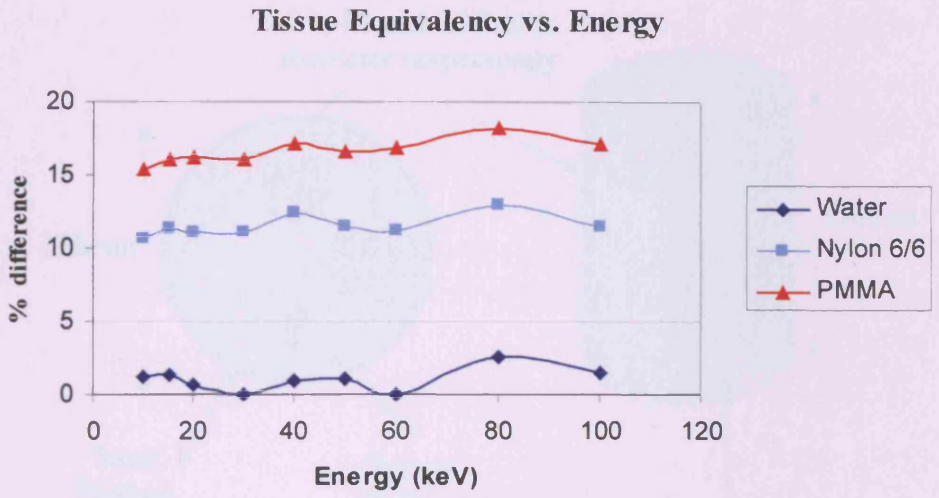

Figure 3.2 Materials employed to simulate soft tissue in the laboratory. The approximation of the materials to soft tissue is given as a function of percentage difference. (NIST Physical Reference data)

Energy (keV)	10	15	20	30	40	50	60	80	100
Cortical Bone (cm^{-1})	54.74	17.34	7.68	2.56	1.28	0.82	0.62	0.44	0.36
Aluminium (cm^{-1})	70.72	21.49	9.29	3.05	1.54	0.40	0.75	0.55	0.46
% Difference	29.18	23.89	20.87	19.29	20.05	21.99	24.38	24.15	28.94

Table 3.2 Linear Attenuation coefficients (μ cm^{-1}) of Aluminium and Cortical Bone (ICRU) for the energy range at hand (NIST Physical Reference data).

The shape of the phantom was of regular cylindrical geometry, as shown in Figure 3.3. A more detailed account of the phantom's dimensions together with distances between various regions within the phantom is presented in chapter 5. The Nylon component of the phantom was 126mm in diameter and 120mm in height. The Perspex casing was 3mm in thickness and was employed to form a rigid basis able to withstand the load of the PRS housing.

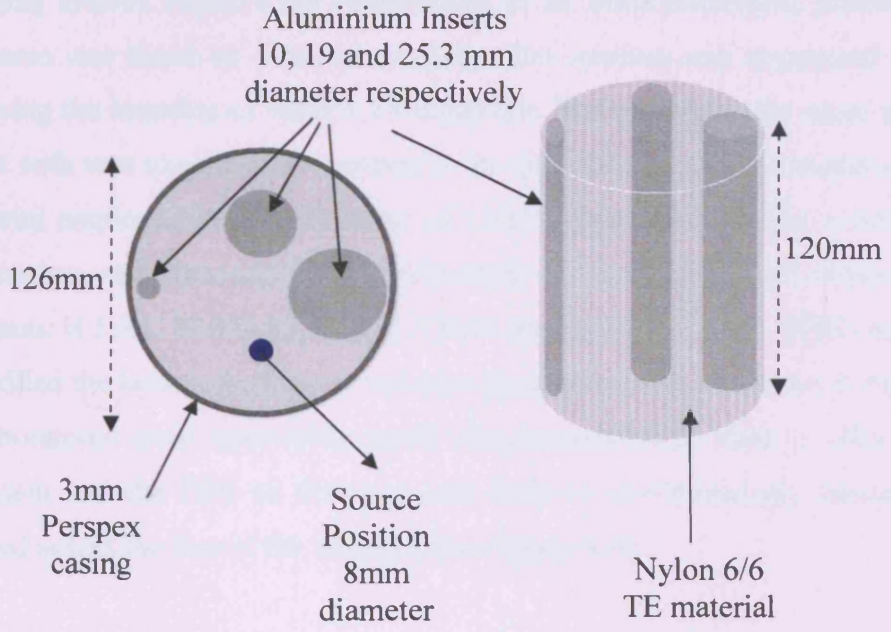

Figure 3.3 Schematic of the phantom constructed to simulate the clinical set-up. The phantom is comprised of two TE components (Nylon 6/6 and PMMA). The Aluminium rods are inserted to simulate bone structures.

The hole for insertion of the source is positioned halfway between the centre of the phantom and the Perspex case edge to provide an off-centre source position in the phantom. The hole is 60mm deep, such that the source lies on the centre plane of the phantom.

3.2.2 Anthropomorphic Phantom

As the work progressed, the need for clinically realistic phantoms, in terms of both geometry and composition, in order to quantify the viability of the PECT imaging system, required the construction of an anthropomorphic phantom. This phantom was based on a human cranium. The cranium was segmented laterally, allowing the insertion of various TE materials. The air gaps in the nasal area were filled with wax to enable the material to be contained within the cranium. The TE material employed was in the form of Lincolnshire Bolus seeds; a sucrose and magnesium carbonate material that simulates muscle (Elemental composition % by mass: H 5.9,C 37.9,O 52.7,Mg 3.5,Bulk density:1050 kg/m3, ICRU report 44), that filled the hollow cranium to simulate the human head, as shown in Figure 3.4. A laboratorial brain stereotactic frame was constructed in order to affix both the phantom and the PRS so that they can both be simultaneously translated and rotated across the face of the detector (See Figure 3.4).

Figure 3.4 The anthropomorphic phantom devised for PECT evaluation (left picture). The PRS was inserted in the phantom using a "crude" strereotactic frame (right picture).

The translation and rotation of the phantom across the detector meant that the PRS source had to be fixed to a rigid, moving structure. The frame was designed to carry the load of the PRS and the TE filled cranium. The speed of translation of the frame across each scanning position had to be carefully considered as bending of the probe was possible due to the inertia during the acceleration and deceleration stage of the linear motion. This had a detrimental effect on the overall PECT scanning time.

3.3 Equipment and Techniques employed in the in-vitro system

The PECT imaging system devised in the laboratory was a rotate-translate ECT system based on a single HPGe detector. The rotation of the detector around the phantom was not ergonomically feasible and therefore the phantom had to be rotated and translated across the face of a stationary collimated detector to achieve the same ECT effect. Although the incentive of this experimental work is to simulate the clinical setting, certain deviations from typical imaging system need to be addressed.

The deviations are:

- "Patient" is rotated (phantom rotation)
- Single detector requiring scanning around object
- Long acquisition times due to scanning and detector type

The source was inserted in the phantom and the detector collected the distribution of photons escaping the phantom as a function of their energy at each scanning position. Inserting the source in the centre of the uniform phantom would, due to symmetry, produce projections with the same intensity distribution. This is because when the phantom is rotated, the source will always lie in the same position. To make the scenario more clinically realistic, the source was inserted in an off–centre position (i.e. it lies half way between the centre and the edge of the

phantom). The phantom (and PRS) was then rotated and scanned across the face of the HPGe detector and spectra were acquired, as shown in Figure 3.5.

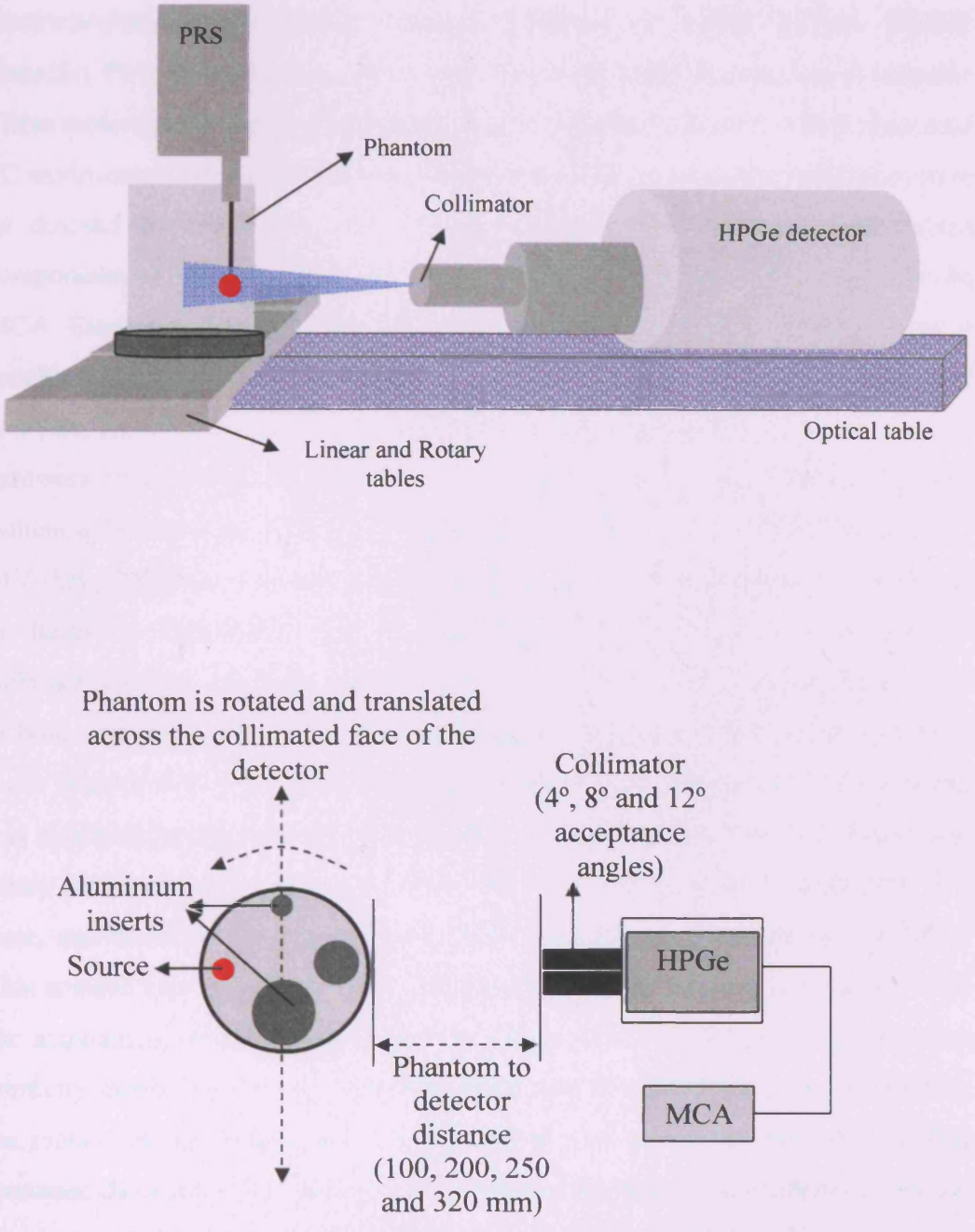

Figure 3.5 The experimental PECT set-up devised for imaging of the PRS (side-view top picture, top-view bottom picture). The phantom is rotated and translated across the face of a stationary, well-collimated HPGe detector.

Electromechanical positioning systems were employed for accurate and synchronous phantom translation. In practice, the phantom was fixed to a rotary table, which in turn was fixed to the linear scanner. Both platforms are electromechanical positioning systems, accurate to within ±25μm (Parker Hannifin Plc). Driver motors drive both the rotary table and the linear scanner. These motors are controlled independently by dedicated software, which runs on a PC environment. It was therefore proposed that a fully automated scanning system be devised by interfacing all scanning components. The three independent components of the system are the rotary and the translation table, and with the MCA Emulator that controls the detector. This allowed, in essence, for a synchronous data acquisition system, i.e. a spectrum acquired at every scanning position. To achieve this, a 4-channel I/O mounting rack was used to interface all hardware components. Digital DC input modules were incorporated for fast switching between the TTL signals that drive the Maestro input and the nominal 24V that powers the controllers for both scanning tables. The master controller of the hardware "handshake" was provided by the *job file* function in the Maestro software (Maestro MCA Emulator, Ortec). It was employed to trigger the motions of both scanners and at the same time control DAQ. This file consists of one or more lines of ASCII text, representing a series of commands that can automate and synchronise all the functions of the scanning system. The translation and rotary functions are controlled by allocation of I/O modules in the controller. The state, and therefore the triggering, of these modules is controlled by the MCA. This ensures that transition of the phantom to the next position is triggered once the acquisition of the previous scan is terminated and the resulting spectrum correctly stored. One major stumbling block was the electronic noise induced by the motion of the various parts which was picked up by the detector, yielding increased dead time. To overcome this problem, the motion controllers of both the rotation and the translation scanners were turned off for the duration of the spectral acquisition. Once the system was optimised, it allowed for a pre-defined number of synchronous spectra to be collected in a repetitive and reproducible manner. The flow diagram in Figure 3.6 shows the structure of the automated scanning system. The MCA has control over the functions of both motors and

triggers any appropriate motion upon request. The increment motion of both tables is pre-defined in the controller software and both wait on idle state until the command for motion is set by the MCA. Once the number of linear scanning positions at each angle is finished, the translation controller brings the table back to the starting position while the rotary table increments one angular step and the process is repeated.

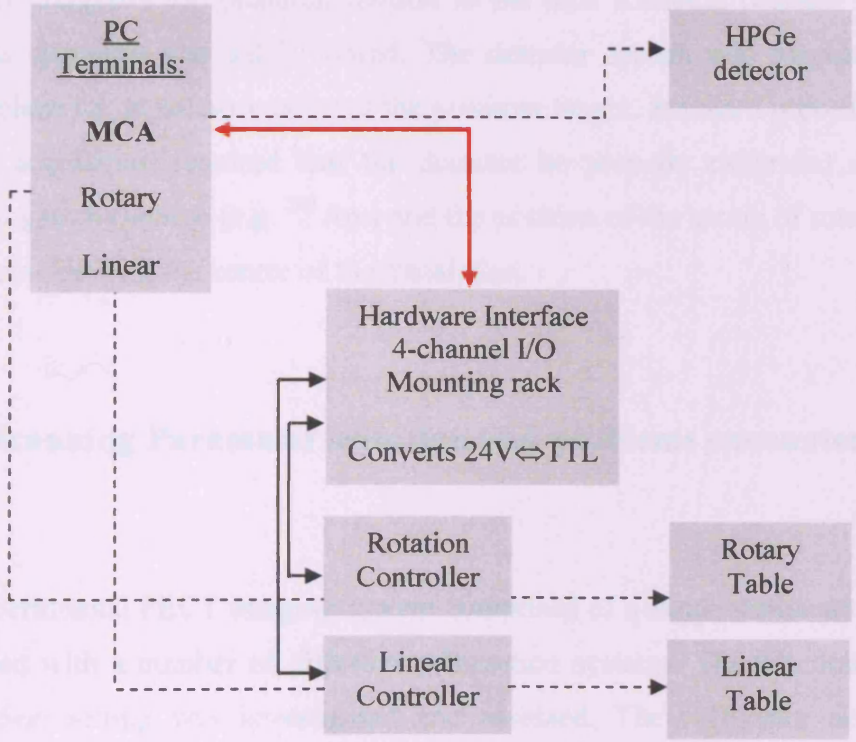

Figure 3.6 Schematic of the structure of the automated scanning system designed for experimental PECT imaging. The dashed lines indicate the nominal connections of the hardware components with their corresponding software (PC terminals). The red line indicates the handshake of the MCA software and the controllers via the mounting rack. The motions of the scanners are pre-defined and are triggered by the MCA software.

The controller software can be used to indicate the position at any moment in the study for both the translation and the rotary table. In this way, the user can inspect the resulting spectra at any scan position and investigate the effect of the geometry on the resulting spectrum in real time. The scanning parameters of each

study, such as the span of the scan and the linear and angular increment slide, are pre-defined in the controller software. Therefore the trigger that arises from the MCA software requests the linear and the rotary table to move by a pre-specified amount. The spectral acquisition parameters were defined in the MCA software. The MCA software also processed the storage of each spectrum so that the continuity of spectra collection would not be jeopardised, resulting in a continuous array of spectra required for accurate image reconstruction. The MCA therefore triggered the phantom motion to the next scanning position once the previous spectrum was safely stored. The detector system was focused on the source plane i.e. at halfway point of the phantom height. Standard procedure prior to data acquisition required that the detector be properly calibrated against a standard gamma source (e.g. ^{241}Am) and the position of the centre of rotation was set to coincide with the centre of the translation.

3.3.1 Scanning Parameter selection and problems encountered

The experimental PECT imaging system comprised of a single stationary detector employed with a number of different collimation systems. The function of each collimation setting was investigated and assessed. The collimator acceptance angle governs the flux of escaping photons that are actually detected by the detector element. The direct relationship of the Source to Detector distance (SDD) in conjunction with the collimator angle to the projected Field of View in the phantom plane is illustrated in Figure 3.7. The number of photon detected in the signal increases with increasing collimator acceptance angles as the FOV increases. It must be noted however, that the response of the collimators is not linear across the whole FOV area. This is due to perturbing effects of photons interacting with the edges of the collimators, making the central part of the FOV more sensitive than the outer. The spatial resolution of the PECT imaging system is dependent on the resulting FOV and plays an important role in the image

formation. The photon-counting rate of the detection system is strongly dependent on the FOV (flux of detected photons).

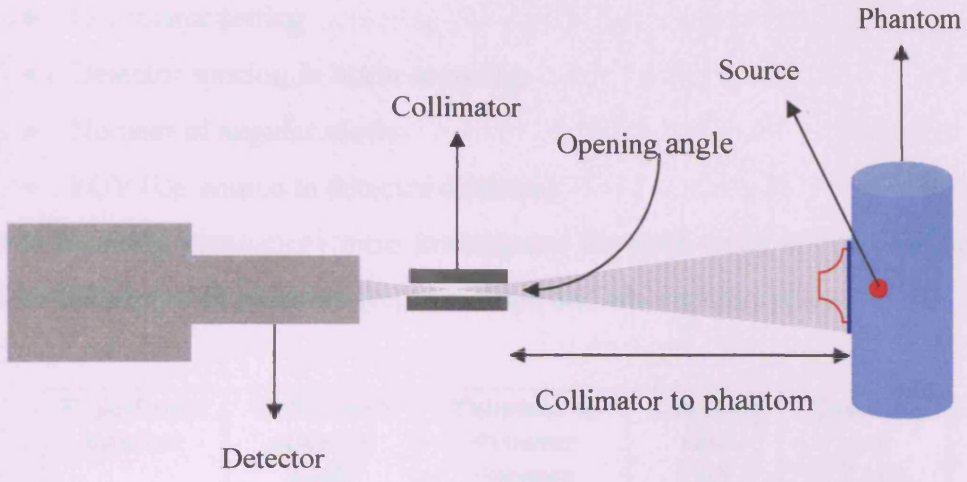

Figure 3.7 The collimator opening or acceptance angle in conjunction with the source to detector distance governs the Field of View (blue line) of the detection system projected on the phantom. The red line shows the non-uniform response of the collimators across the FOV range.

In the case of the PRS implementation in the PECT studies the high, flux of the emanating photons meant that special care had to be taken so that the photon counting performance of the detector was not compromised. In some cases the implementation of a high-rate amplifier was necessary to accommodate the high flux of PRS photons. Table 3.3 shows the complete list of the various collimator settings that were investigated in this work. The approximate (rounded figure) photon counting rate is measured on the uniform phantom at the centre of rotation, i.e. when the source in the phantom is aligned with the collimator. The 12° acceptance angle collimator could not be employed for the PRS work, as the high emitted flux could not be easily handled by the detector (>10000 cps).

In an attempt to optimise the PECT imaging system and to predict the ideal set-up for the most accurate means of localisation, various scanning parameters have been systematically investigated for both types of radiation sources (PRS and ^{241}Am). The effect of these parameters on the resulting image was assessed.

Quantitative image analysis at various parameter settings will provide the optimal PECT set-up.

The scanning parameters investigated were:

- Collimator setting
- Detector spacing in linear scanning
- Number of angular views
- FOV (i.e. source to detector distance)

These scanning parameters were investigated for both types of radiation source and on both types of phantom (regular shape and anthropomorphic).

Experiment number	**Collimator opening angle**	**Phantom to detector distance**	**Counting rate PRS Cps**	**Counting rate ^{241}Am Cps**
1	4°	100mm	1000*	250
2	4°	200mm	600	180
3	4°	250mm	500	100
4	8°	200mm	2000*	500
5	8°	250mm	1200*	300
6	8°	320mm	800	100
7	12°	250mm	N/A	700
8	12°	320mm	N/A	500

*High-Rate Amplifier required (Integration times: 2.5μsec compared to conventional Amplifiers of 8μsec)
N/A: not possible with PRS

Table 3.3 Collimator settings at various distances yielding different FOV. The counting rates are approximate (to the nearest rounded figure), however they do indicate the function of the collimation of the PECT imaging system.

In the case of the heterogeneous regular shape phantom, Aluminium rods were used to simulate bone and to act as position indicators on the image. Landmark registration using bone structures in the patient is often used in medical imaging and in particular in brachytherapy treatment planning systems. Landmark registration in the PECT case can provide additional geometric information and direct interpolation of distance measurements. Furthermore, in the case of image fusion e.g. PET-CT or SPECT-CT, various image registration methods employing landmarks are used (Joslin *et al* 1999). This is normally done by the insertion of external markers (or landmarks) whose 2-D coordinate system is employed for image fusion. This idea can also be employed in PECT and the application of image fusion will be discussed later.

3.3.2 System Performance and Error Analysis

The overall performance of the PECT system is based on the performance of all the individual components of the scanning system. Errors are introduced in the electromechanical motion of both the rotational and translational motions of the phantom across the face of the detector. Such errors in the accurate movement of the phantom can prove detrimental in the image reconstruction procedure as the true centre of rotation may have shifted. The positional variance of the system is negligible as the motors that drive both the rotary and the linear tables incorporate encoders which constantly record (every 5msec) the current position of the table and adjust the requested propagation of the table according to its previous position. This yields an overall positioning error of less than 30μm, a figure indeed negligible if considering the nominal linear increment of 5mm.

Errors are also introduced in the detector and its photon counting capability. Radiation measurements are single measurements of x, x being the number of detected photons, whose distribution function is generally defined by Gaussian distribution (for large x). The predicted variance is σ^2 for such a distribution

where $\sigma=\sqrt{x}$, the deviation from the true mean that typifies the single measurement x (Knoll 1988). This implies that for a single measurement with a 1% deviation, roughly 10000 counts are required to be detected. The effect of the photon counting statistics on the resultant image is discussed in chapter 4.

3.4 Image Reconstruction Techniques

Image reconstruction was carried out using a custom software code written in IDL (Speller 2003, Erlandson 2003). The spectra acquired at every position in the scanning of the phantom were transferred to IDL. The software was written so that it reconstructs images directly from the raw data (16bit binary format), in this case the whole array of spectra. No additional manipulation of these spectra prior to reconstruction is required. A standard filtered back projection FBP algorithm was chosen for the reconstruction of the images. Although the choice of this reconstruction method is contra-indicated for ECT imaging as mentioned before, it was considered that FBP would adequately handle the PECT data. This arises from the fact that the PECT acquired data is continuous and of superior statistical quality compared to standard ECT images. This is due to the fact that both sources analysed were placed interstitially rather that injected so the resulting intensity of the emitted photons was far greater than normal SPECT or PET images as the PRS is designed as a therapeutic x-ray source. Furthermore, the implementation of iterative reconstruction techniques (IRT) would dramatically add to the computation times required for image reconstruction, without benefiting in the quality of the resulting images. The algorithm was kindly provided by Professor R. Speller and was modified accordingly to handle the acquired data.

The algorithm firstly "reads in" the array of spectra. It then sorts out the array by arranging the total number of spectra into the appropriate angular and radial bin of a 2π revolution. Selective reconstruction is the process whereby images are created from distinctive energy windows; the high energy resolving power of the HPGe allows for careful distinction between scattered and primary radiation. This

is done in terms of channel numbers in each spectrum. The nominal number of channels used in this work was 512 and the channel numbers containing the 60 keV peak were pre-determined during energy calibration of the MCA. The selective reconstruction, which is a key factor in this work, can be carried out directly by the algorithm. During reconstruction, the code creates a sinogram from the rearranged data or projections. This is a 2-dimensional representation of the projections and is a very quick and efficient way of checking for irregularities in the data prior to reconstruction. A sinogram is the 2-dimensional representation of the whole data array and it is formed by rearranging the projections into a 180-degree distribution. Sinograms formed for different energy windows and for different phantom composition are shown in Figure 3.8. During the sinogram formation, the code process manipulates the projections by mapping the first 180-degree projections onto the *reversed* remaining 180-degree projections.

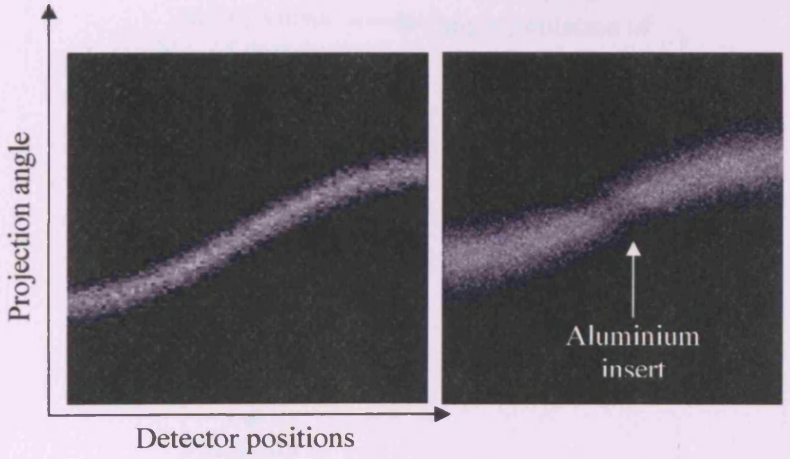

Figure 3.8 Formation of sinograms during image reconstruction. Data is presented in a 2π orientation. Sinograms formed by integration of: the photo-peak for homogenous phantom left and total spectrum integration for heterogeneous phantom composition (right).

The advantage of this technique is that it enhances the statistics of the data, resulting in better image quality. Furthermore, it compensates for the attenuation correction required in an ECT image formation. The sinogram needs to be

transposed for filtering to take place. The sinogram is then corrected for the centre of rotation depending on the number of detector positions employed. A standard Hamming filter was used for filtering the data in the Fourier frequency domain. The filtered sinogram is then re-transposed in its original orientation so that back projection can be performed using the Radon transform function. Figure 3.9 shows a flow chart of the structure of the reconstruction algorithm designed for this work. The resulting image can be processed, analysed and stored directly from the code.

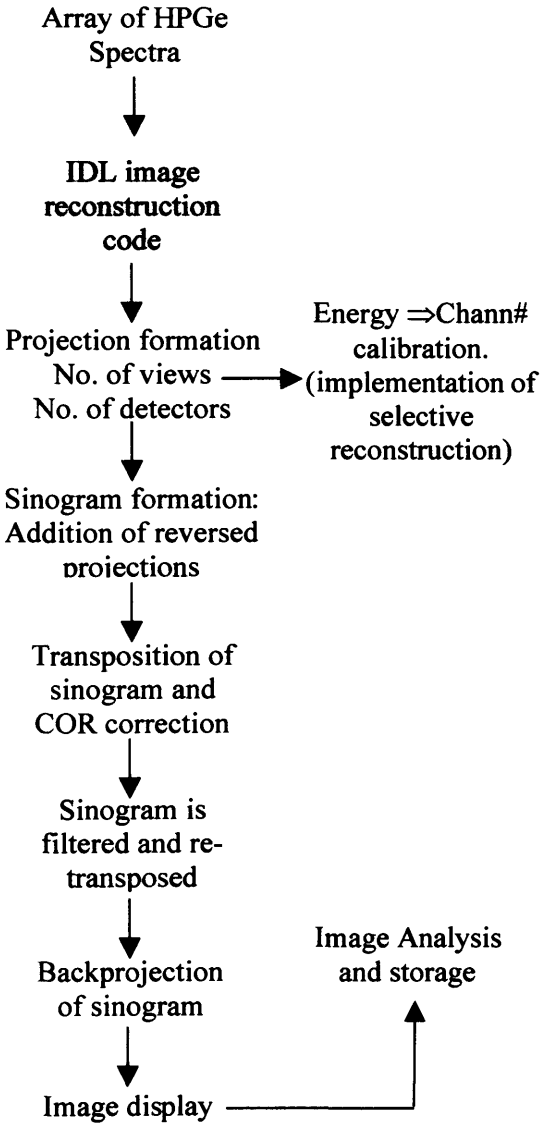

Figure 3.9 Flow-chart of the processes that take place during FBP image reconstruction. Energy window selection allowed for the simulation of other detection systems. Images were analysed and stored directly from the code.

The implementation of the Radon transform in Medical Imaging detects features within a 2-dimensional image. The definition of the Radon transform is graphically demonstrated in Figure 3.9.

Let us consider the intensity that is to be imaged as a 2 dimensional function in the x-y plane, i.e. f(x, y). The 1-dimensional projection of the intensity along a line L that is at a distance s from the origin and at angle θ with respect to the x-axis is defined as g (θ, s).

This is known as the line integral of the intensity f (x, y) along the line L and may be written as $g(\theta,s) = \int_L f(x,y)dL$

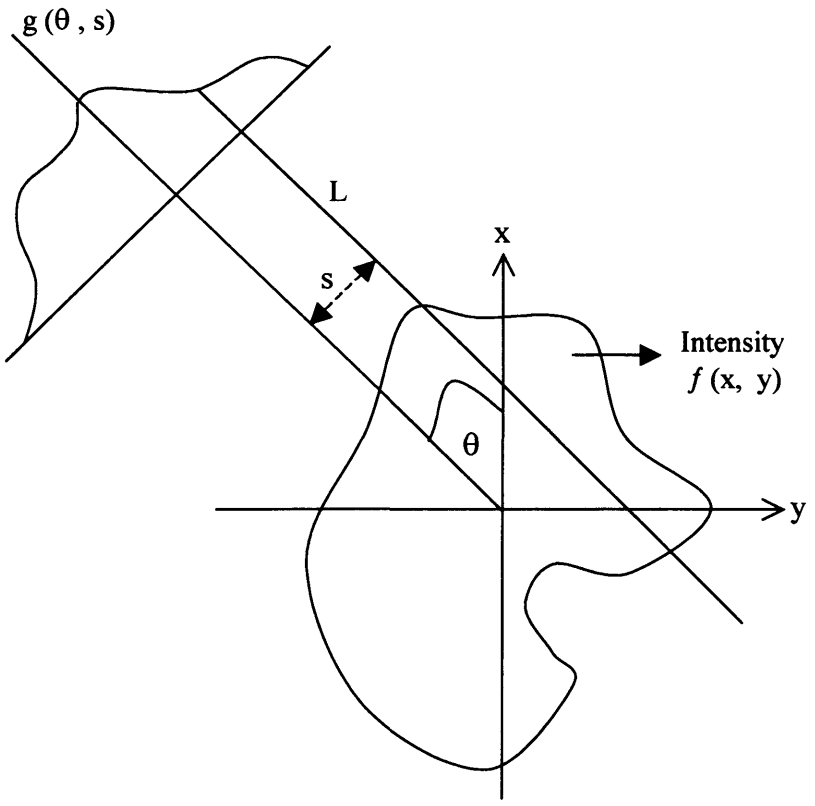

Figure 3.10 Line integral of the image intensity f (x, y) along a line L at a distance s form the origin at an angle θ from the vertical.

All points on line L must satisfy the equation:

$x\sin(\theta) - y\cos(\theta) = s$

Therefore, the projection function g (θ, s) can be re-written as:

$g(\theta,s) = \iint f(x,y)\delta(x\sin\theta - y\cos\theta - s)dxdy$.

The collection of all values of g (θ, s) at all θ is called the Radon Transform of image intensity f (x, y). Backprojecting the data using this function allows the image output to be defined in terms of horizontal and vertical coordinates. This becomes very important in the accurate translation of image coordinates to geometrical coordinates for source localisation assessment.

3.5 Reconstructed Image Analysis

Once images are constructed, the IDL programme allows the user to manipulate those images. The user can inspect the raw data that forms the images in terms of their resulting sinograms. Different energy window selection performed during selective reconstruction the resulting computed sinograms is shown in Figure 3.8.The user can perform a number of different image analysis applications as soon as the image is constructed. Region of interests (ROI) can be selected in the resulting image and different regions on the image can thus be inspected. This tool can be used for statistical analysis of the images and assessment of the quality of the images. Furthermore, contoured surface plots of the image can also be generated to provide the user with information about the intensity distribution of the image. However, the most common image analysis tool used in this work is the *profiler* shown in Figure 3.11. This command in IDL allows the user to draw profiles across a 2-dimensional image by moving the cross-hair cursor anywhere on the image plane. The advantage of this is that the position of the cross hairs on the image is quoted in terms of pixel coordinates in both axes of the image. The position where the maximum intensity lies can be accurately located on the profile and its coordinates recorded. Having pre-defined the source position in the

phantom in terms of real geometrical units, one can then verify the position of the source on the image by utilising the profiler application. Converting the pixel coordinates into real geometrical units, the precision with which the source is localised on the image can be investigated. The IDL *profiler* function was implemented as the standard method of localising the source on the image. This allowed for detailed assessment on the precision with which the source can be localised on the image.

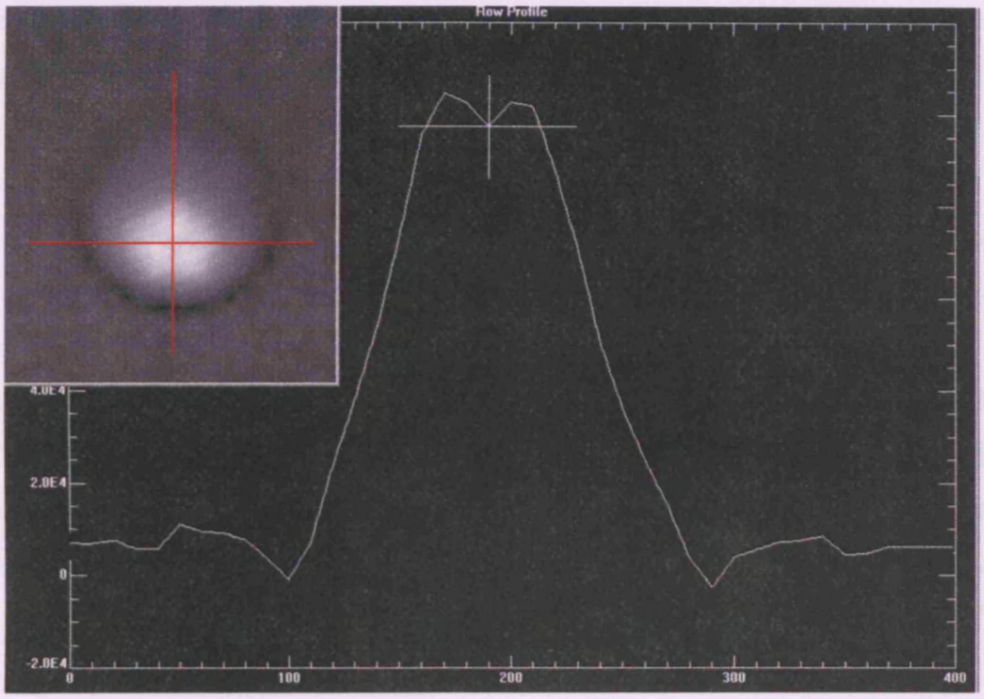

Figure 3.11 Profile across image (top left) to locate point of maximum intensity across the x and the y plane. Coordinates on the image are then translated into geometrical units so that accuracy of localisation can be assessed.

The FBP algorithm employed for the measured data was also used in the theoretical image formation. The simulation of the experimental set-up was performed in order to replicate the measured images, thereby allowing careful manipulation in order to extract further information. Replicating the images implied that the reconstruction route had to be identical in order to produce comparable images. IDL was therefore employed for theoretical data

manipulation and image formation as well as the experimental image reconstruction and proved a very powerful and reliable tool in the data analysis of this work.

3.6 Monte Carlo Simulations

The modelling of the experimental set-up was undertaken in order to replicate the measured images in an attempt to translate the photon emission image into a distribution of the dose deposited by the source. The Monte Carlo modelling was therefore employed to perform two different tasks. The schematic in Figure 2.5 (Chapter 2) shows the two different computer models that were employed in this work. The two modelling paths required different type of computations. The spectral collection code was structured to provide position and energy information for photons escaping a regular cylindrical TE phantom, but in the dosimetric modelling work, the energy deposition in the phantom was computed. This required a different geometry and scoring module (BEAMnrc). The output of both of the MC models was analysed and reconstructed using IDL. This allowed for accurate correlation of the emission image to the dose map under similar conditions using the same software. The theoretical dosimetric results were compared against measured data in water. This allowed for optimisation of the code in terms of the accuracy of the energy deposition. Dose maps of the PRS in the nylon phantom were computed and then cross calibrated against the emitted image so that the convolution parameters could be derived. Phantoms of differing compositions were investigated.

3.7 Monte Carlo simulations performed

The MC simulation studies carried out in the first phase involved the generation of spectra collected on a Germanium detector. Table 3.4 shows the input

parameters used in the computation. The incident energy (E-Inc) of the photons was 59.5 keV in the case of the mono-energetic ^{241}Am source. In the case of the PRS, the radiation output of the probe, as measured in air on HPGe, was inserted in the code. The geometry of the regular phantom was modelled using the cylindrical geometry module of GenUC. The detector was modelled as a germanium ring around the detector, focussed at the source plane. The model implemented was used to compute spectra at various geometry settings replicating the experimental set-up. The generated spectra were ported to IDL for identical image reconstruction. The general physical parameters that were considered in the MC model are presented in Table 3.4.

MC Simulations **Spectral collection and Dose Computations**	**EGSnrc / GenUC** **BEAMnrc**
Number of Photon Histories	1-8 x 10^8
Lower photon cut-off energy for transport (MeV)	AP =1.0 x 10^{-3}
Lower charged particle cut-off energy for transport (MeV)	AE = 0.521
Photon cut-off energy (MeV)	PCUT = 1.0 x 10^{-3}
Charged particle cut-off energy (MeV)	ECUT = 0.521
Fractional energy loss	ESTEPE = 0.25
Coherent Scattering (Rayleigh) Incoherent Scattering (Compton) Photoelectric Effect	ON ON ON

Table 3.4 Input parameters of the MC simulations performed.

In the second phase of the MC studies, the energy depostion of the PRS source in the phantom was computed. Energy depostion per single particle at each volume element was recorded. The 2-D distribution of these elemental volumes gives rise to the dose deposition map. Insertion of the dose map in IDL, allows for its

visualisation as function of its intensity distribution. The model was implemented for the simulation of the PRS source only. The proposed calibration of the modelled emitted image to its predicted dose map was therefore only performed on the PRS source.

3.8 Data collection and its implementation in a proposed PRS400 treatment planning system.

The PECT imaging system was designed to provide accurate source localisation of the PRS source when buried in the body. MC simulation of the experimental PECT system, confirming the imaging abilities of the system was employed in order to relate the image created by PECT to a dose deposition map of the PRS output in the phantom. The translation of the image to a dose map can be carried out using this transform map. The convolution of the image to dose as predicted by the simulation model allows a point by point correlation of the "activity" image to dose deposition. If an empirical transformation function for this translation were to be devised then an effective treatment planning and treatment control system could be devised. The image formation can be carried out using the PECT technique to locate the source. These coordinates will be used for accurate registration of the source on the image so that transformation can be precisely performed. Computation of the transformation function could in theory be carried out on line with the imaging system, thus providing an in-vivo, in-situ TPS that monitors the delivery of the radiation treatment. To ensure correct alignment and registration of the two images (emission image and dose map image), land marking could be employed using external markers made of high Z material.

CHAPTER 4

Results on PECT Source Localisation

Introduction

The work on source localisation using the PECT imaging system was undertaken in two stages. In the first stage, the PECT system was tested for viability using an ^{241}Am source inserted into regular geometry phantoms. The second stage involved the implementation of the PRS source. As the work progressed, the laboratorial simulation moved towards more realistic conditions, requiring the use of anthropomorphic phantoms. The experimental simulation undertaken for the PECT source localisation is graphically represented in Figure 4.1. The experimental work moved over the surface, shown in Figure 4.1, from the simplistic set-ups to the ultimate goal of using the PRS with an anthropomorphic phantom. Investigations were carried out based on three generic conditions. The source under study (i.e. ^{241}Am or PRS), the phantom and therefore the medium employed, and finally, the detection system's feasibility to carry out the task of source localisation. Furthermore, the scanning parameters, such as number of views, number of detector positions, FOV and integration time were systematically investigated in order to derive the optimal PECT detection system. The implementation of the ^{241}Am source in the first stage of the simulations allowed better understanding of the physical interactions taking place, as distinction of primary to secondary radiation (scattered radiation) is possible with the Germanium detector. This also provided an insight into what might be expected in the implementation of the PRS in terms of detector response and its effect on the resulting image. Different source localisation techniques arising from image reconstruction were investigated. Selective image reconstruction was performed to simulate the response of other detection systems.

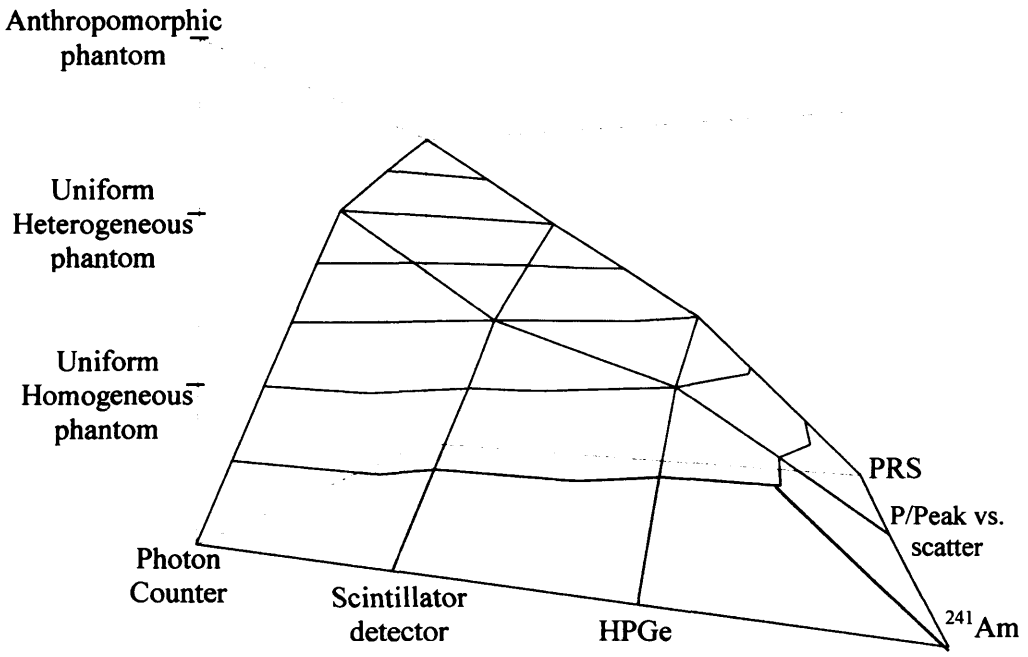

Figure 4.1 Simulation surface of the PECT source localisation investigations carried out. The simplistic case of a mono-energetic source in uniform phantoms was gradually shifted towards more clinically realistic conditions (PRS in anthropomorphic phantoms).

The PECT simulations were undertaken under various scanning parameters. The parameters investigated allowed for the optimal detection set-up to be identified, resulting in the most accurate means of source localisation. The scanning parameters investigated were:

- Field of View (FOV) of the collimator system
- Number of angular projections
- Number of detector positions

Summarising, the work on PECT source localisation involved the assessment of both sources in different composition phantoms at various scanning parameters in order to identify the optimal detection set-up for accurate localisation.

4.1 General observations from Spectral Acquisition of the ^{241}Am mono-energetic source

^{241}Am energy spectra collected from various angular projections provided varying information content. The spectra collected were represented as histograms of photon detection events by the detector. The multi-channel analyser (MCA), coupled to the detector, stored the incoming signal in a bin according to its amplitude. Pre-calibration of the detector system using a standard reference gamma ray source (^{241}Am) converted the number of the channel (bin) into a corresponding energy.

A high energy-resolution detector, such as HPGe, allows for excellent discrimination (to within 0.5 keV) of incoming photons. Distinction, therefore, between primary and scattered radiation is possible and could be implemented in the image reconstruction. The content of the spectral information is dependant on the scanning position and the angular projection of the phantom. In the case of the in-homogenous phantom where the source is in the off-centre position, the spectra collected denote different information according to the angular detector position. As the phantom is scanned across the face of the detector, there is a specific scanning position where the source aligns itself with the detector allowing a larger proportion of the primary photons to be detected. Similarly, there are other scanning positions that do not align the source with the detector collimator, giving rise to only scattered photons being detected. In the case of the inhomogeneous phantom, where aluminium rods are inserted into the phantom, there are positions in the scanning procedure where the rods align themselves between the source and the detector, resulting in spectra where masking effects predominate as shown in Figure 4.2.

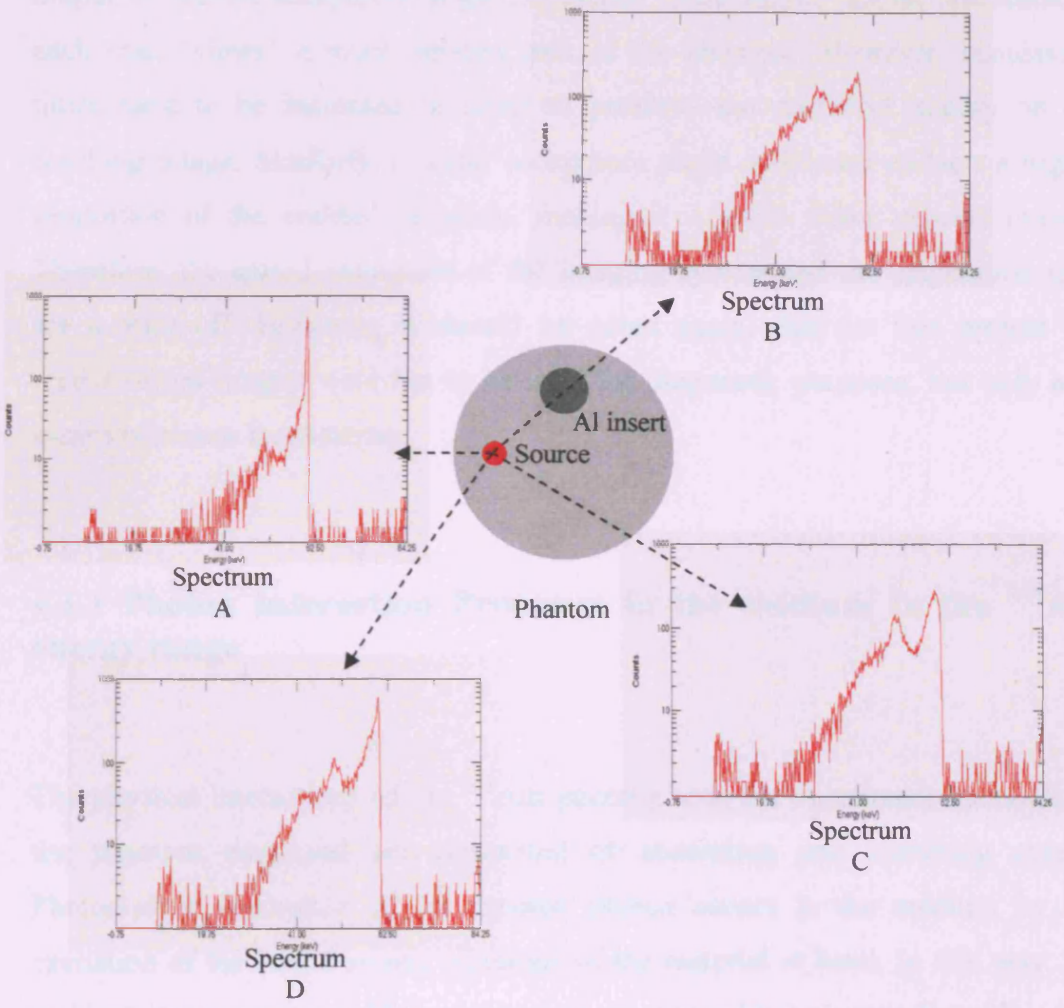

Figure 4.2 ^{241}Am spectral collection in the heterogeneous phantom. The spectral information varies according the angular detector position. The above spectra represent the central scanning slice at the corresponding angle. The collected spectra are described as follows. Spectrum A: Primary photon detection predominates at the beam transverses a small amount of the phantom. Spectra C and D describe the increasing scattering effect as the photons go through a larger portion of the phantom material. In Spectrum B the Aluminium rod insert "masks" out a large proportion of the primary photons whilst scattered photon collection predominates.

The counting statistics of the spectral acquisition are heavily dependent on the collimator's acceptance angle at the face of the detector. Pulse pile-up can be a

problem due to the long pulse shaping time (set to 6 μsec) of the main amplifier. The recording high photon fluxes will be highly compromised by this effect and this issue becomes very important in the use of the PRS's high intensity radiation output. A narrow acceptance angle collimator yields higher spatial resolution as each scan "views" a much smaller part of the phantom. However, acquisition times have to be increased in order to preserve the statistical quality on the resulting image. Similarly, a wider acceptance angle collimator collects a higher proportion of the emitted radiation, making it a much faster process overall. Therefore, the spatial resolution of the imaging system and the acquisition time are a trade-off. However, it should be noted again, that for this project the reconstructed images were not to be used for diagnostic purposes, but only as a means of source localisation.

4.1.1 Photon Interaction Processes in the medium in the ^{241}Am energy range

The physical interactions of the ^{241}Am photons with the constituent materials of the phantom employed are comprised of absorption and scattering events. Photoelectric absorption of the emitted photon occurs in the medium by the excitation of the bound atomic electrons of the material at hand. In this way, the incident photon carries sufficient energy to eject an orbital electron from the atom of the medium. The excited atom (ion) returns to ground state by the emission of characteristic x-rays as electronic reconfiguration takes place. The scattering events that occur are categorised in terms of elastic (Rayleigh) and inelastic (Compton) scatter processes. The mass attenuation coefficients for the phantom materials in the ^{241}Am energy range (59.5 keV) are given in Table 4.1 (NIST Physical Reference data). The probability for an interaction event whether it is absorption or scatter, in the medium at 59.5 keV can therefore be computed and is given in the same table.

^{241}Am 59.5 keV	Scatter cm^2/g		Photoelectric Absorption cm^2/g	Total Attenuation cm^2/g
	Elastic	Inelastic		
Nylon	$1.02x10^{-2}$ **5%**	$1.76x10^{-1}$ **91%**	$7.45x10^{-3}$ **4%**	$1.94x10^{-1}$ **100%**
Al	$3.44x10^{-2}$ **12%**	$1.48x10^{-1}$ **54%**	$9.28x10^{-2}$ **33%**	$2.81x10^{-1}$ **100%**
PMMA	$1.11x10^{-2}$ **6%**	$1.73x10^{-1}$ **90%**	$9.02x10^{-3}$ **4%**	$1.93x10^{-1}$ **100%**

Table 4.1 Probability of physical interaction of ^{241}Am photons with the phantom material constituents.

The figures in the Table 4.1 indicate that Compton (inelastic) scattering predominates in the tissue equivalent phantom material (Nylon and PMMA), while Photoelectric absorption becomes more evident when inhomogenities in the form of Aluminium rods are introduced. The spectra shown in Figure 4.2 are in agreement with the above data. Photons that traverse "tissue" material undergo scattering and once they impinge on the Aluminium rods are mainly absorbed. Photons, therefore, that are detected by the PECT imaging system are comprised by either primary photons that are elastically scattered (~ 4%) or have escaped the phantom uninteracted, and photons that have managed to escape the phantom having undergone inelastic scattering. The scattered photons detected must have undergone single scattering events. Multiple scattering events occurring within the phantom will probably prevent the photon's escape from the medium, as the photons will consequently be completely absorbed within the medium. It is difficult to experimentally predict how many orders of scattering events a photon can undergo before it is completely stopped in the medium and it is estimated that photons that do actually escape the medium must have undergone single inelastic scattering. In such events, the incident photon energy does not decrease considerably and thus the photon manages to escape the phantom. The photon interaction analysis lead to an understanding of the issues involved in the image

formation. The detection of primary photons emitted by the source buried in the phantom will assist in denoting where the source lies on the resulting image. This is not totally true, as primary photons that undergo inelastic scattering will still carry their incident energy, however the point of emission will not be the actual one as recorded by the imaging device. The PECT imaging system cannot distinguish between primary and elastically scattered photons as both types of photons carry the same energy. However, the elastic scattering content is small and can therefore be ignored. The inelastic scattering events assist in the formation of the periphery of the medium in the image reconstruction as shown in Figure 4.3. As the phantom is scanned across the face of the detector, the nature of the radiation collected is strongly dependent on the portion of the phantom as viewed by the collimation system. The total data collected is thus comprised of many such spectra collected around the phantom. The consequent image is therefore formed by the summation of all primary and scatter spectra hence, careful attention must be paid to the detection of the scattered photons as they form a useful means of image formation (Speller and Horrocks 1991). Scatter is always considered a stumbling block in radiological or x-ray imaging and scatter rejection or reduction methods have all been extensively reported (Boone and Seibert 1988). Since the PECT images in this work are not produced to derive diagnostic information, photon scatter will be employed to assist in the image formation and consequently will not be rejected. The ability of the detection system to resolve between primary and secondary radiation allows for investigation of the effect of scatter on the resulting images. Energy window selection in the image reconstruction and the resulting effect was therefore possible and was used in an attempt to define the most accurate means for source localisation. This selective reconstruction procedure enhances the choice of the HPGe detector as the single energy photons emitted by the ^{241}Am source in the phantom can clearly be distinguished in terms of their resulting energy.

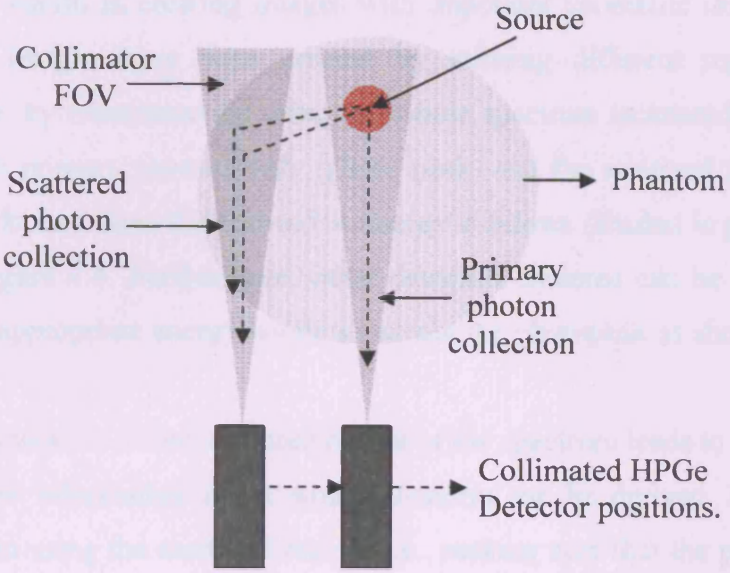

Figure 4.3 Spectral collection based on detector position. At the edge of the phantom, scattered radiation collection predominates while as the source aligns itself with the detector mostly primary photons are collected.

4.1.2 Effects of energy window selection on reconstructed images

As discussed in section 2.3.3, detector systems with a range of energy resolving properties can be simulated from the acquired Germanium spectrum. The accumulated spectrum collected during acquisition represents the photon measurements at one point in any projection. Typically in ECT, 100 such spectra constitute a projection and 100 projections make up the data set. In general, accurate source localisation can best be achieved by focussing solely on the photopeak, whereas the scattered photons must be included in order to see the periphery of the phantom and to study dose distributions within the phantom. In an attempt to register geometrical attributes of the image, careful manipulation of the spectra during reconstruction needs to be undertaken. The idea of energy

selective reconstruction, justified by the implementation of the HPGe detector, proved very useful in creating images with important geometric information. In this thesis, images have been created by utilising different regions of the spectrum, i.e. by reconstructing using the whole spectrum (scattered and primary photons), the primary photons only (photo peak) and the scattered photons only. The images formed from the respective energy windows (shaded in grey area) are shown in Figure 4.4. Furthermore, other detection systems can be simulated by selection of appropriate energy windows across the photopeak as shown in Figure 4.5.

Careful manipulation of the scattered region of the spectrum leads to images being formed where information about source location can be derived. For example, reconstruction using the scattered region, i.e., making sure that the primary photo peak is omitted, forms images showing a dark spot of low intensity where the source of primary photons would lie. The central spectrum in Figure 4.4 (scatter only) demonstrates the energy window selection for such a reconstruction. The shadowed part of the spectrum is utilised in the image formation, purposely omitting the photopeak. If the energy window selection was to include the photo peak, then the image created contains the bright spot together with the distribution of locations where photons have been scattered. Images formed by selecting the photo peak only will result in images containing the bright spot only. Finally, the total spectral collection used in the image reconstruction yields images where the whole periphery of the phantom is described. This arises from the fact that all of the Compton scatter content is incorporated in the image formation and thus the region of all interactions is described. The scatter only image retains the phantom geometry information, however the omission of the photopeak results in a different image as shown in Figure 4.3. This can also be shown in terms of sinograms. A sinogram, as stated before, is a means of image representation of raw data, obtained when projection-reconstruction imaging is used. The sinogram is a two dimensional representation of the signal measured at a given angle in the imaging plane at varying distances along the detector array, as stated in Chapter 3.

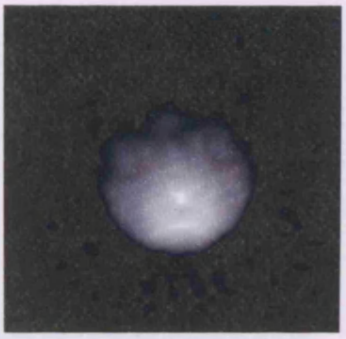

Total Spectrum

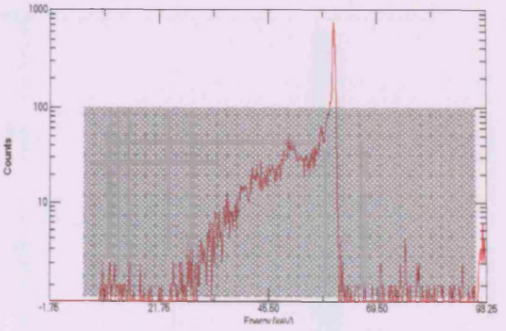

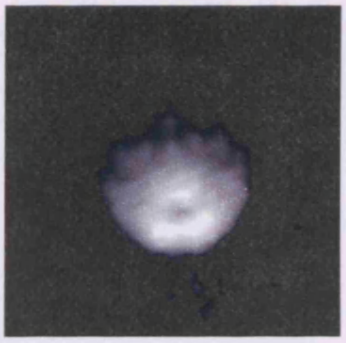

Scatter only (P/Peak omission)

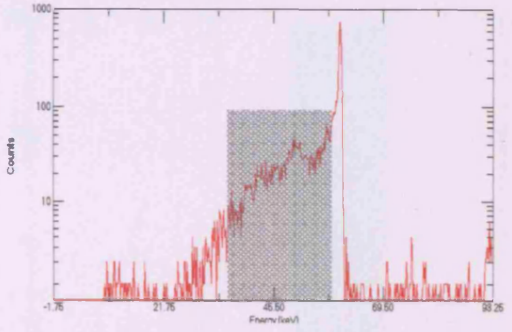

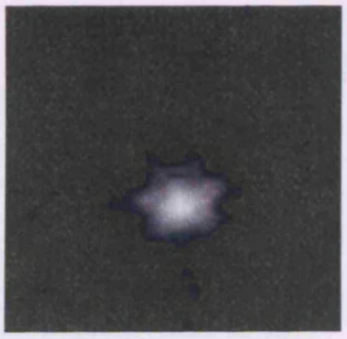

Photo Peak only

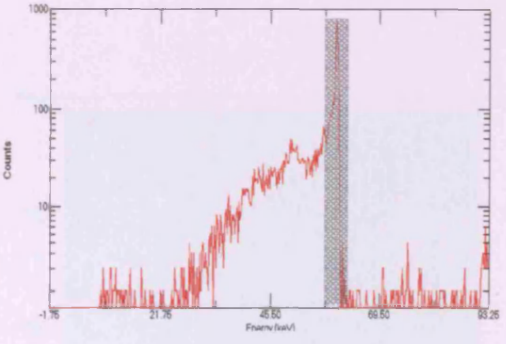

Figure 4.4 Energy window selection for image reconstruction. Spectral integration (right) and the resulting image (left) is shown. The total spectrum integration results in the description of the periphery of the phantom on the image. The same applies for the scatter only image as sites of scatter interactions occur on the whole phantom. Finally, the photopeak image denotes only where primary photons predominate so the periphery of the phantom is no longer described on the image.

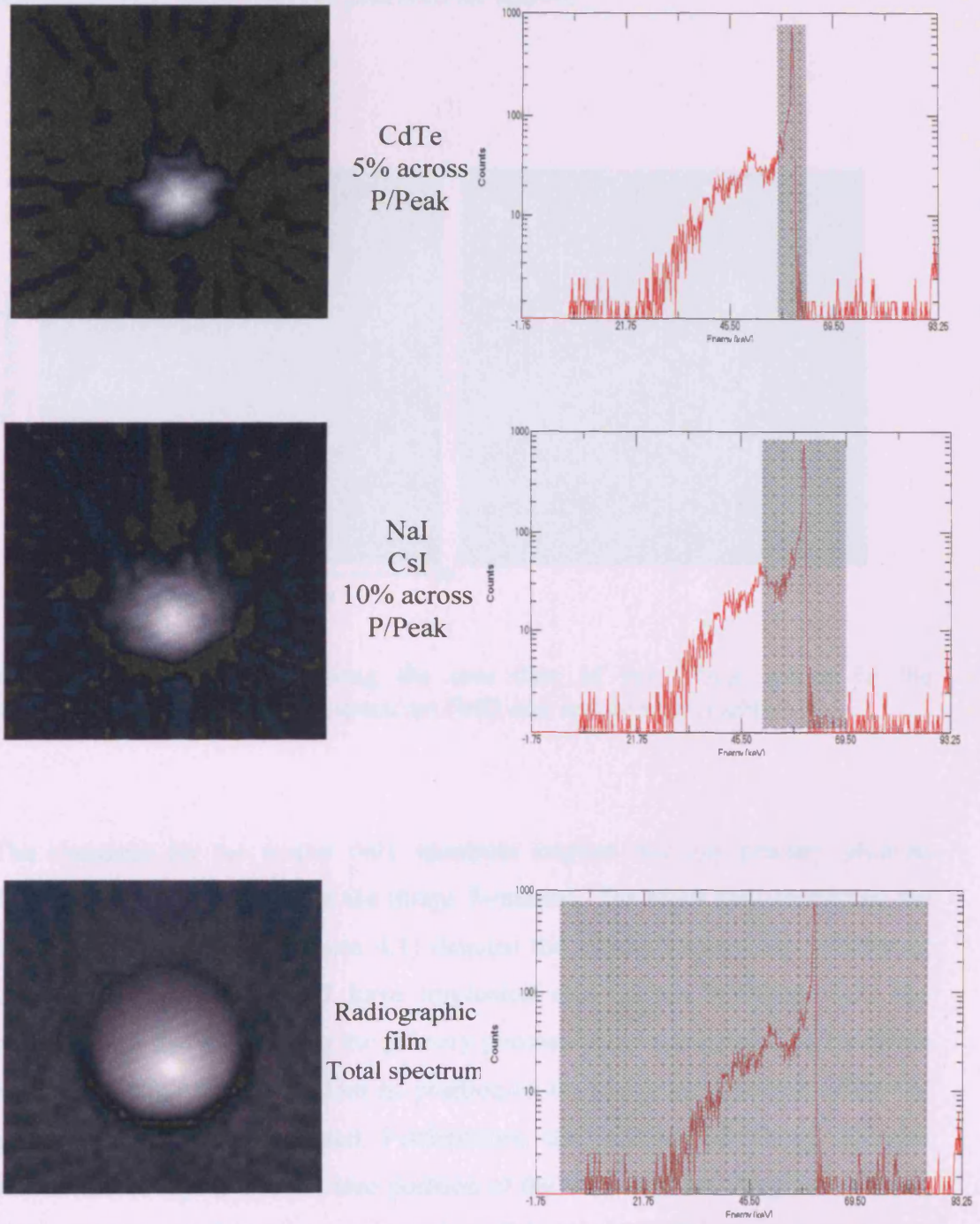

Figure 4.5 Simulation of detection systems. Solid-state detectors and scintillation detectors are simulated by energy window selection (grey shaded area) across the photopeak. (5%-CdTe, 10% -NaI/CsI). Total spectral integration simulates photographic film or photo counters. As the photopeak integrated window increases, so does the resulting image. The scattered radiation content is incorporated into the photopeak, resulting in description of a larger part of the phantom on the image.

In Figure 4.6, the sinograms generated for the total spectrum and the scatter only spectrum in the heterogeneous phantom are shown.

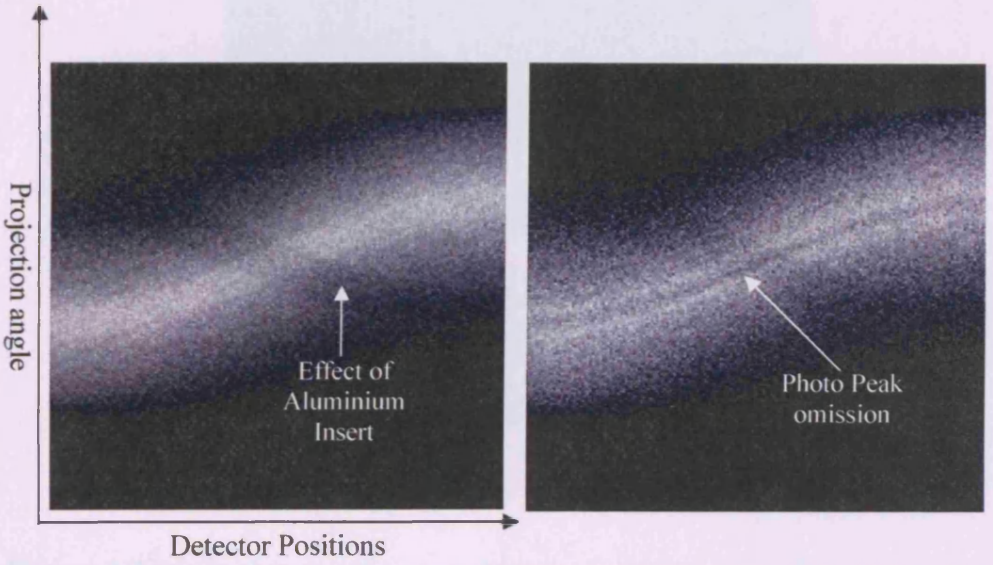

Figure 4.6 Sinograms showing the raw data of the ^{241}Am source in the heterogeneous phantom: total spectrum (left) and scatter only (right).

The sinogram for the scatter only spectrum implies that any primary photons detected will not contribute in the image formation. The black spot created on the image (middle image of Figure 4.4) denotes the position where the primary or unattenuated photons should have originated also shown in Figure 4.7. The postulation is that by omitting the primary photons in the reconstruction, the black hole is identifiable, and therefore its position on the image must declare where the photons should have originated. Furthermore, the omission of primary photons must conclusively denote the true position of the source on the image, as primary photons are emitted by the source only and have not undergone any means of inelastic scattering. Photons that have undergone elastic scattering would not have lost any energy, however their directional change due to the scattering event cannot be determined.

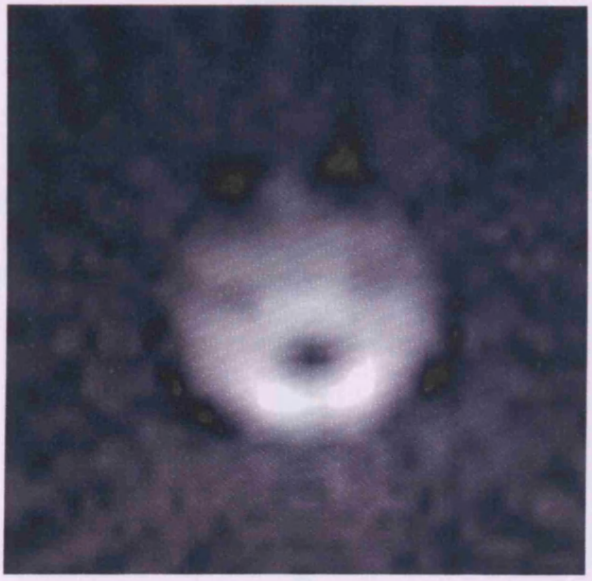

Figure 4.7 Image showing the *virtual source* location as the dark spot against the bright background. The periphery of the phantom is described by scattering events occurring in the medium. Localisation precision has been shown to be enhanced using the *virtual source* information.

The spectral manipulation during image reconstruction is referred to in this work as selective reconstruction and it yields the *virtual source* image. This image can be utilised in the attempt to localise the source position in the image.

If the reconstructed energy window was to include the photo peak only, then a bright spot appears, denoting the primary photon emission as shown in Figure 4.4. The effect of the *virtual source* formation is pictorially presented in Figure 4.8. Photons that undergo a "grazing" Compton scatter interaction, i.e. deviation from their original path by a small amount, will inevitably lose a small fraction of their incident energy. Figure 4.9 shows the Compton relationship of angle to scattered photon energy and demonstrates the effect of such an event. Photons can undergo further scattering events until they are completely absorbed in the medium. Alternately, photons that escape the medium will be detected by the Germanium detector

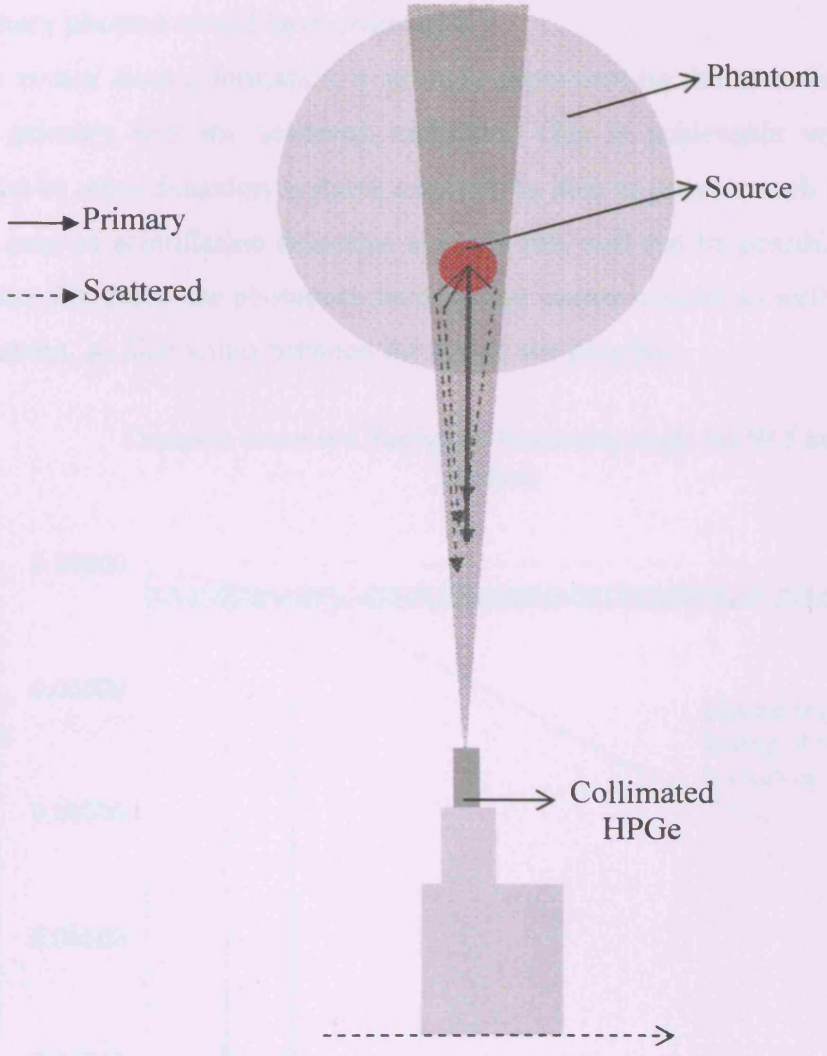

Figure 4.8 Collection of primary and scattered radiation by the collimated HPGe. Photons that undergo small angle scattering and are collected together with the primary photons. Distinction of the two is possible, thus omission of the primary will be described by a dark hole on the resulting image.

The distribution of such scattering events contributes to the formation of the periphery of the phantom on the image, as shown in Figure 4.4. The resolving power of the detection system (shaded region) allows for discrimination of such events (to within 0.5 keV). This results in the ability to select an energy window based on scattered radiation only. Omission, therefore, of the primary photons in

the reconstruction routine will bring about the shaded area on the image where primary photons would have originated.

The *virtual source* formation is strongly dependent on the accurate distinction of the primary and the scattered radiation. This is achievable with the HPGe, however other detection systems may not be able to provide such information. In the case of scintillation detection systems this will not be possible, as shown in Figure 4.4. Here, the photopeak includes the scatter content as well as the primary radiation, so distinction between the two is not possible.

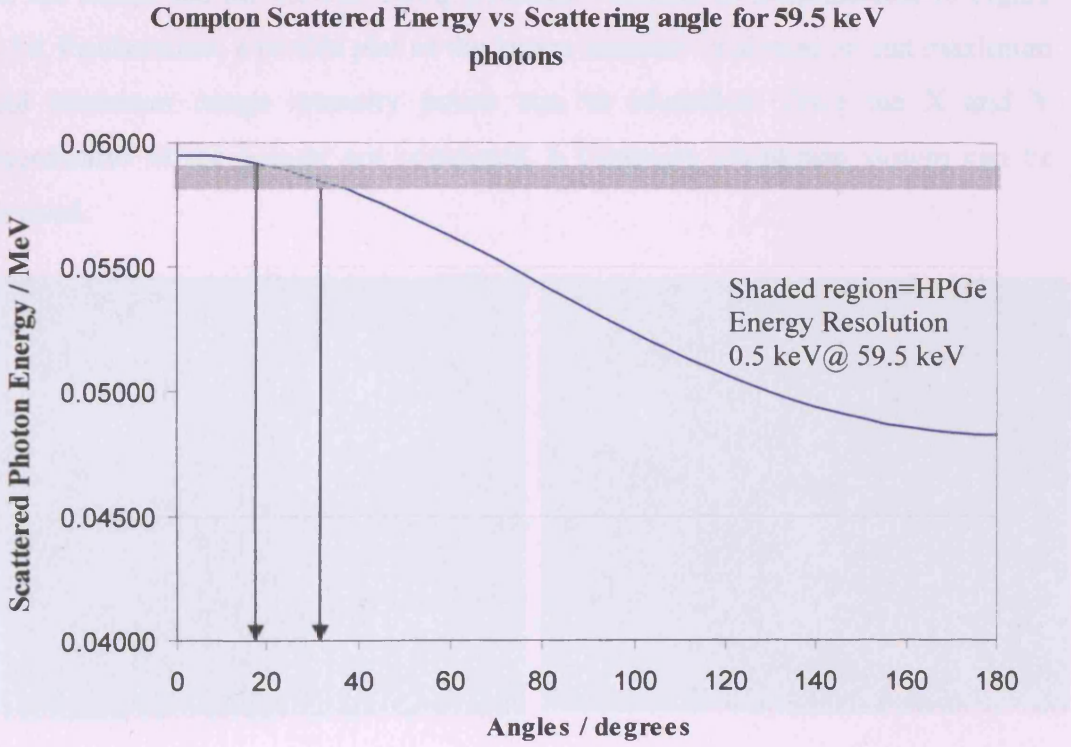

Figure 4.9 Relation of scattered photon energy to scattering angle for single Compton scattering event. The shaded region represents the energy resolution of the HPGe detector. The vertical lines demonstrate the range of scattering angles that could be obtained within the specified energy resolution

Finally, in this work, the *virtual source* information is intended be used to localise the ^{241}Am source on the resulting image. The precision with which the source can be localised will dictate the optimal scanning parameters of the imaging system.

4.1.3 Localising the source position on the image

In order to determine the black spot of the *virtual source* on the reconstructed image, profiles need to be drawn in order to compute the X and Y coordinates in terms of pixel values of the position of the dark spot on the image. Running the *profiler* function of the image analysis tool in IDL allows these coordinates to be determined. Under this function, a pointer or cursor can be positioned anywhere on the image and the corresponding position recorded, as demonstrated in Figure 4.10. Furthermore, a profile plot of the image intensity is plotted so that maximum and minimum image intensity points can be identified. Once the X and Y coordinates of the pointer are computed, a Cartesian coordinate system can be devised.

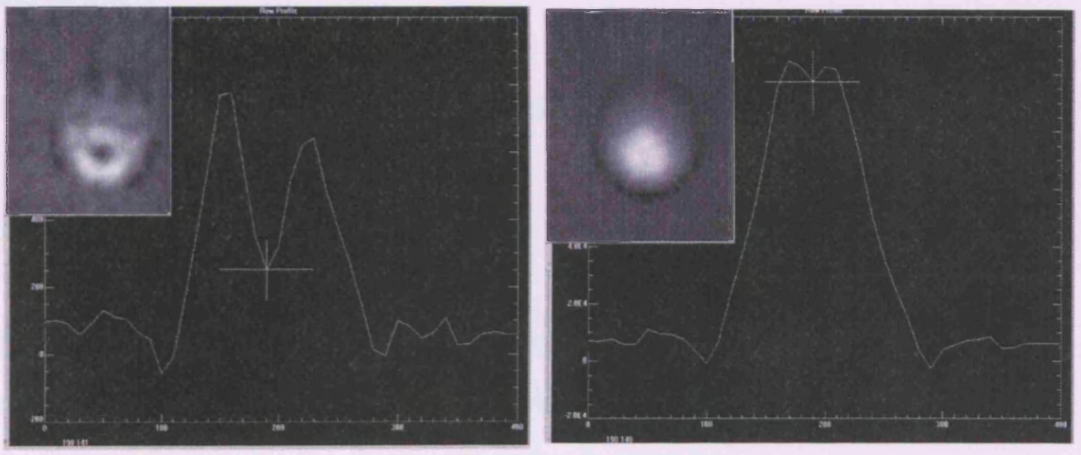

Figure 4.10 Source Localisation on the PECT images [scatter only (left) and total spectrum (right)] using the IDL profiler. The coordinates of the source are computed and compared to the physical dimensions of the source and the phantom for assessment of the PECT precision.

The geometrical source location in the phantom (in units of mm) is easily obtainable and the projected source position in the image (in units of pixels) can therefore be determined. Implementing this coordinate system allows for analytical investigation of the localisation and its precision. The deviation of the cursor position from the true source location is determined by the difference in the

X and Y plane quoted in pixel values. The difference in these values (X and Y) shows the deviation of the source location, as computed on the image from its true geometrical position. The magnitude or modulus of the deviation can be computed either as a percentage deviation from the true source position, or as a function of measured distance (in mm).

Let $\mathbf{X_i}$ and $\mathbf{Y_i}$ be the coordinates of the true source location in the phantom (in pixels values).
Let the computed coordinates of the source location in the image be **X** and **Y** respectively (in pixel values).
The deviation from the true source position is therefore:

$\mathbf{X_i - X = \Delta X}$ the deviation value in the X plane
and similarly
$\mathbf{Y_i - Y = \Delta Y}$ in the Y plane.
The deviated distance **d** from the true source location is thus given by:

$$\mathbf{d} = \left[(\Delta X)^2 + (\Delta Y)^2\right]^{1/2}$$

The error associated with the computation of X and Y will be incorporated in the calculation. Let the error in computing X be σ_x and similarly for Y be σ_y, then the propagated error σ_d for the above calculation is given by:

$$(\sigma_d)^2 = \frac{X^2}{X^2 + Y^2}\sigma^2_x + \frac{Y^2}{X^2 + Y^2}\sigma^2_y \qquad \text{Appendix A}$$

The absolute coordinates, in geometrical units, of the true position of the source in the phantom were calculated, and hence translated into pixel units on the image. This arises from the IDL reconstruction code, under the Radon back-project values, which specifies the dimensions of the image output. In the code the X and Y plane sizes are given by: NX=40 and similarly NY=40. Knowing the translation increment, which in most cases was 5mm, implies that the geometrical

dimensions of the image formed are 40 x 5=200mm in both the X and Y plane. The image dimensions in terms of pixels are again given in the code to be 400 x 400. Therefore, converting pixels to true geometrical dimensions:

400 pixels/200 mm = 2 pixels/mm.

The coordinates that are computed by running the Profiler in IDL are quoted in pixel numbers. Converting those pixel coordinates into true geometrical units allows for accurate assessment of localisation accuracy.

4.1.4 Precision of Localisation using PECT

The task of localisation precision will determine which detector set-up provides the most accurate results. The two energy spectrum regimes under investigation are the primary only (photopeak) and the scatter only (*virtual source*). Other spectral regimes, such as the total spectrum could be utilised for source location. In the case of the total spectrum, the ability to distinguish the primary photons on the image is considerably hindered by the inclusion of all photons (primary and scattered) in the spectrum. The total spectrum was not assessed as the uniformity of its resulting image does not provide precise information for source localisation. The maximum intensity region lies over an extended area (>50 pixels) and therefore a distinct point at the highest intensity cannot be accurately determined. The photopeak image provides a bright spot around the location of the source while the scatter image provides the *virtual source* that comes about by the omission of the primary photons. Both the photopeak image and the *virtual source* image were investigated for localisation accuracy using the ^{241}Am source. The precision of localising the source on the image has been derived from the deviation of the computed source location on the image from the true source position in the phantom. The percentage deviation from the true source position, averaged out for both x and y axes was calculated. Scanning parameters were systematically altered in order to investigate the optimal settings for accurate localisation as shown in Figure 4.11.

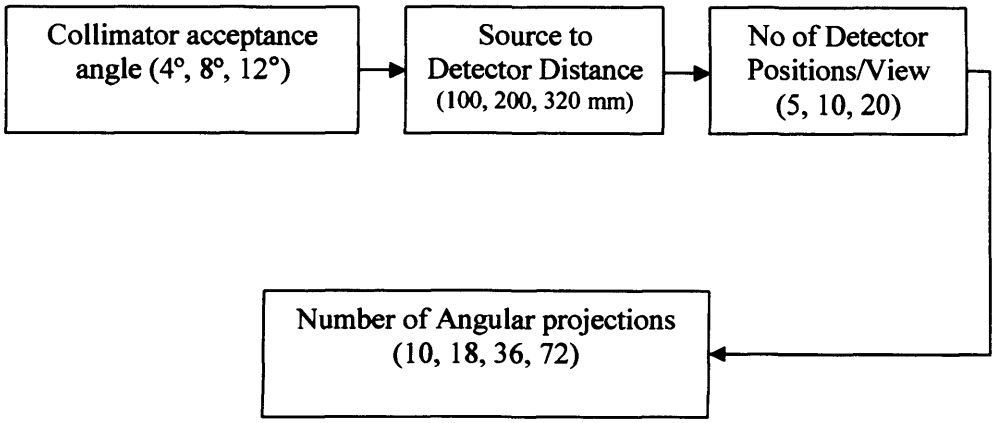

Figure 4.11 Scanning parameters investigated. The first two settings govern the projected FOV i.e., the counting statistics of the system. The other two settings govern the total data set collected for image reconstruction.

The effect of the scanning parameters on the precision with which the source can be located on the *virtual source* image has been investigated. The number of linear projections (i.e. number of detector positions at each angular projection) chosen for this work was 5, 10 or 20. The linear increment of the scanning of the phantom across the detector was varied (20mm down to 5mm) so that the whole of the phantom was completely scanned. The reconstruction algorithm requires that the object is fully scanned and has no pre-knowledge of its dimensions.

The effect of the number of angular projections on the image was thoroughly investigated. This provided information regarding the minimum number of projections required for accurate source location. The number of projections investigated was 18, 36 and 72. Increasing the number of views could not be easily implemented as the overall scanning times became difficult to handle. The minimum number of projections required for accurate source localisation was also investigated, however as the resulting image formation is also of concern to this work for dosimetric purposes, decreasing the number of projections to less than 18 resulted in images being formed with star-like artefacts, arising from the way the algorithm handles incomplete data set. Finally, the effect of the projected FOV that is brought about by the collimation set-up employed was also investigated.

This was analysed in terms of the counting performance of the detection system according to the collimation set-up devised. This resulted in assessment of the statistical significance of the counting rate (acquisition times) on the resulting image. The results on ^{241}Am source localisation using both the photopeak and the *virtual source* information are shown in Figure 4.12. Source localisation using the total spectrum was not performed on the mono-energetic source. The reason for this is that the photopeak will be incorporated into the total spectrum, and since the detection system can distinguish between the primary and secondary radiation, the photopeak on its own provides superior localisation to the total spectrum. In physical terms, this means that the response of a detector system based on total spectral collection (i.e. radiographic film) will not be assessed. The reason for this is that film cannot be considered as a successful candidate for a PECT detector as the resulting image cannot be inferred in real time. Development of the exposed film prevents the real-time dose transformation that is intended in this work. Photopeak integration will not be possible on the continuous PRS spectrum as the detection system cannot resolve the incoming photons in terms of primary or scattered radiation. The total spectrum will therefore have to be integrated for source localisation in the PRS case. The results in Figure 4.12 are given as a function of deviated distance in mm from the true source position with error estimates given for all experimental settings i.e., for all collimator acceptance angles, detector positions, source to detector distance (SDD) and number of angular projections. The values are quoted to nearest whole number except for more accurate error estimates of less than 2mm which are quoted to two decimal places At some scanning parameter settings, e.g. employing 5 detector positions at each of 18 projections, the resulting image did not allow for localisation assessment as artefacts were formed due to the incomplete nature of the data. In the other extremity, employing 20 detector positions for 72 angular projections was not ergonomically feasible, as it meant lengthy data acquisition times (in excess of 8 hours). These scanning set-ups are denoted as not available (N/A) in Figure 4.12. Furthermore, in the implementation of the 8° acceptance angle collimator, the SDD had to be increased to 200mm as detected radiation flux increased considerably, giving rise to an increased detector dead-time.

4° acceptance angle@100 mm SDD

Detector Positions	No. of Projections	P/Peak	Scatter only
	18	N/A	N/A
5	36	14±9	13±7
	72	12±6	11±5
	18	8±5	7±4
10	36	6±3	5±3
	72	5.7±1.9	5.2±1.6
	18	2.2±1.3	2.9±1.4
20	36	1.1±0.9	0.8±0.3
	72	N/A	N/A

4° acceptance angle@200 mm SDD

Detector Positions	No. of Projections	P/Peak	Scatter only
	18	N/A	N/A
5	36	15±9	14±7
	72	13±7	12±6
	18	9±4	8±3
10	36	6±3	7±2
	72	6.2±2.1	5.3±1.7
	18	2.4 ±1.4	3.1±1.8
20	36	1.8±1.0	1.2±0.4
	72	N/A	N/A

8° acceptance angle@100 mm SDD

Detector Positions	No. of Projections	P/Peak	Scatter only
	18	N/A	N/A
5	36	18±7	16±5
	72	13±5	11±4
	18	10±3	9±3
10	36	8±2	6.3±1.8
	72	4.5±1.1	4.1±1.0
	18	4.3±1.3	4.0±1.0
20	36	3.2±0.7	3.0±0.3
	72	N/A	N/A

8° acceptance angle@200 mm SDD

Detector Positions	No. of Projections	P/Peak	Scatter only
	18	N/A	N/A
5	36	17±6	17±6
	72	14±5	13±5
	18	11±4	10±3
10	36	9±2	8±2
	72	6.2±1.9	5.9±1.4
	18	5.5±1.9	4.7±1.5
20	36	4.0±1.3	3.8±1.1
	72	N/A	N/A

12° acceptance angle@200 mm SDD

Detector Positions	No. of Projections	P/Peak	Scatter only
	18	N/A	N/A
5	36	19±9	17±7
	72	14±4	12±4
	18	12±3	10±3
10	36	11±3	9±3
	72	9±2	8±2
	18	6.8±1.9	5.9±1.7
20	36	5.4±1.3	4.9±1.1
	72	N/A	N/A

12° acceptance angle@320 mm SDD

Detector Positions	No. of Projections	P/Peak	Scatter only
	18	N/A	N/A
5	36	20±8	18±8
	72	14±5	13±4
	18	14±5	14±4
10	36	11±4	10±3
	72	9±3	8±2
	18	8±2	6.7±1.9
20	36	6.6±1.8	5.1±1.3
	72	N/A	N/A

Figure 4.12 Results on the ^{241}Am source localisation as a function of deviated distance from true source position (in mm).

The results showed that localisation using the *virtual source* image provided fractionally (~2%) better accuracy than using the photopeak. For the mono-energetic ^{241}Am source, the *virtual source* image allows for accurate profile measurements, yielding superior source localisation on the resulting image. The *virtual source* provides a "sharp" distinction between the scatter image and the omitted photopeak, resulting in greater confidence for cursor positioning when drawing the profile across the image. The photopeak image also allows for accurate source localisation to a lesser degree, however in the case of poly-energetic sources (PRS), where distinction between the primary and secondary radiation is not possible, the total spectrum collected has to be integrated for source localisation.

Moreover, the results showed that localisation of the ^{241}Am source in the homogeneous, regular geometry phantom can be achieved to within 1mm using the *virtual source* and to within 1.5 mm using the photopeak spectrum only. The statistical quality of the data set increases as the detector positions and number of angular projections increase, as shown in Figure 4.13. This results in more accurate means of localisation as the statistical quality of the resulting image enables more precise localisation. Increasing the source to detector distance (SSD) and the collimator acceptance angle both result in an increase of the Field of View (FOV) of the imaging system. This results in a bigger proportion of radiation being recorded. Consequently, the ratio of primary to scattered radiation increases with increased FOV. However, the spatial resolution of the imaging system decreases with increased FOV. The former forms a trade-off with the latter, resulting in slight deterioration (5-10%) of the localisation accuracy as the FOV is increased.

The effect of the detector's energy resolution on the localisation precision was also investigated so that the ideal PECT detection system can be devised. Energy windows across the photopeak were drawn to simulate different detection scenarios, as shown already in Figure 4.4. This assisted in investigating whether departure from solid state radiation detectors, such as HPGe or CdTe, to scintillation counters, such as NaI or CsI, is feasible in the context of this work.

The results of this investigation are presented in Figure 4.14 where the accuracy of source localisation is assessed for various detection systems (Metaxas 2004).

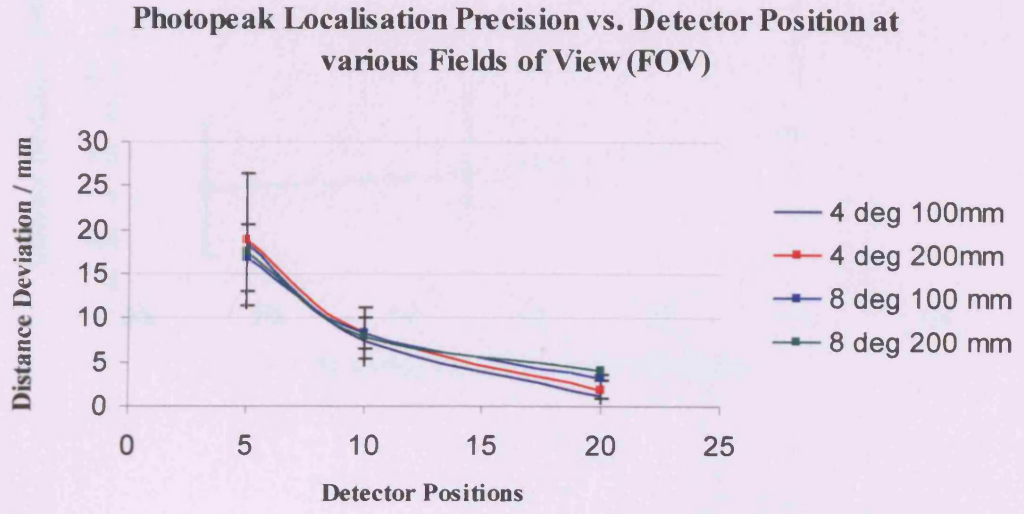

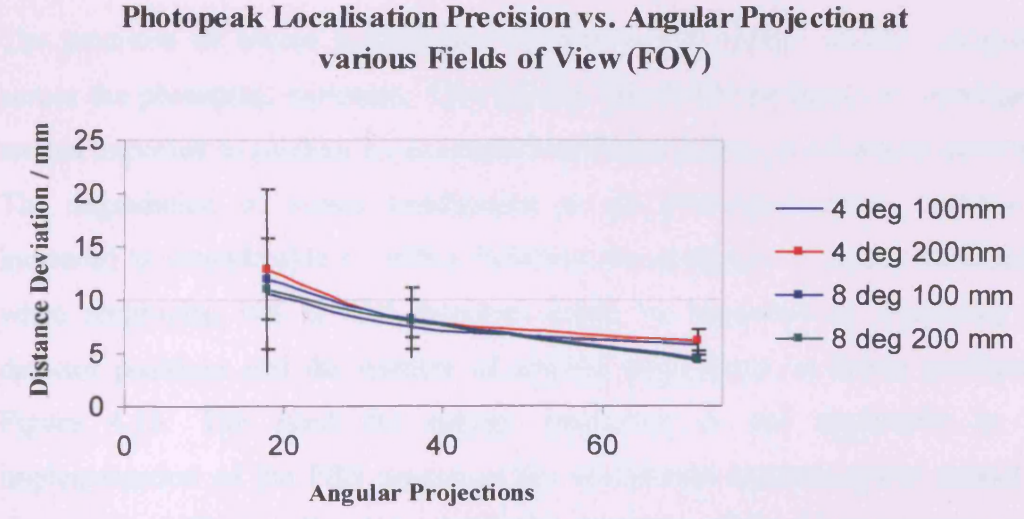

Figure 4.13 Effect of the number of detectors and the number of angular projections on the precision of photopeak localisation using a mono-energetic ^{241}Am source. Increasing the number of detector positions and angular projections results in increased precision in source localisation.

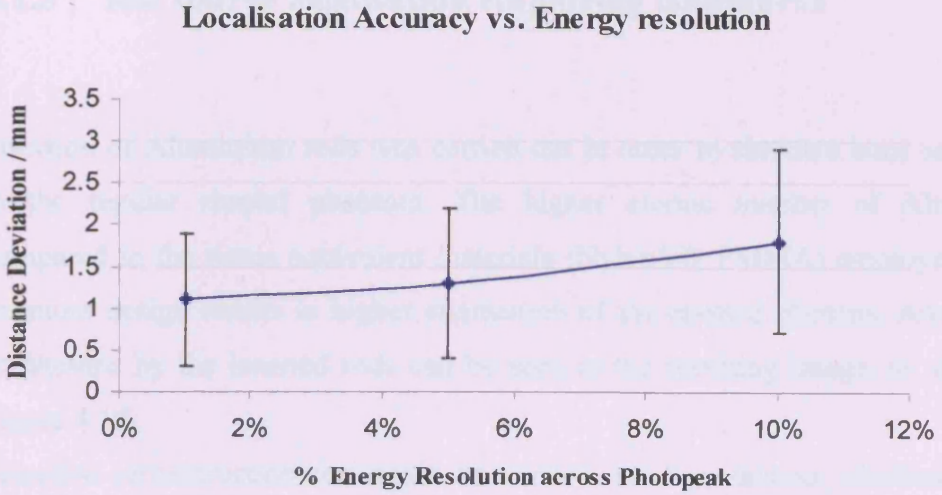

Figure 4.14 Precision of the source localisation for various detection systems. The response of the detection systems is modelled as a function of their respective energy resolving power (i.e. 1%, 5% and 10% energy window integration across the photopeak simulating HPGe, CdTe and NaI respectively)

The precision of source localisation worsens as the energy window integrated across the photopeak increases. This implies that detectors based on scintillators are not expected to produce as accurate localisation results as solid state detectors. The degradation of source localisation as the photopeak energy window is increased is considerable (~ 65%), however the accuracy of source localisation when employing NaI or CsI detectors might be improved by increasing the detector positions and the number of angular projections, as theory predicts in Figure 4.13. The need for energy resolution is not applicable in the implementation of the PRS source as the continuous spectral output cannot be distinguished. This implies that scintillation detectors might still be regarded as an ideal candidate for the PRS PECT detection system.

The optimal settings for providing the most accurate means of source localisation based on the findings of this work are concluded at the end of this chapter.

4.1.5 ^{241}Am source localisation employing landmarks

Insertion of Aluminium rods was carried out in order to simulate bone structures in the regular shaped phantom. The higher atomic number of Aluminium compared to the tissue equivalent materials (Nylon6/6, PMMA) employed in the phantom design results in higher attenuation of the emitted photons. Attenuation of photons by the inserted rods can be seen in the resulting image, as shown in Figure 4.15.

Selective reconstruction can again be carried out in a manner identical to the homogeneous phantom. This is essential, as the photopeak-integrated image will not show the rod. The scatter content of the collected spectrum needs to be integrated for the description of the whole phantom, as stated previously. The resulting image indicates the rod positions. These positions may be used to assist in source localisation by registering the source on the image with respect to these landmarks. The source localisation was undertaken in the usual manner, however in this case the distance of the source position to the rod was computed on the image and compared to the physical dimensions on the phantom. Computation of the Aluminium rod location was again performed by drawing profiles across the image in both dimensions. The distance of the source to the rod was measured to both the edge and to the centre of the rod. The dimensions of the rod can easily be determined on the image using the profiler function in IDL. The resulting images were formed at various scanning settings. Magnification of the phantom dimensions was observed at increased source to detector settings (200 and 320 mm). In such cases, the magnification ratio was computed by direct comparison of the Aluminium rod dimensions on the image to their true geometrical dimension. The computed ratio was implemented in the accurate derivation of the image dimensions.

Having localised the source on the image and thus determined the distance of the source to the Aluminium rod, accurate registration of the source on the image with respect to the known landmarks can be carried out. The insertion of the rods in the phantom was performed in order to simulate a more clinically realistic case, as discussed previously.

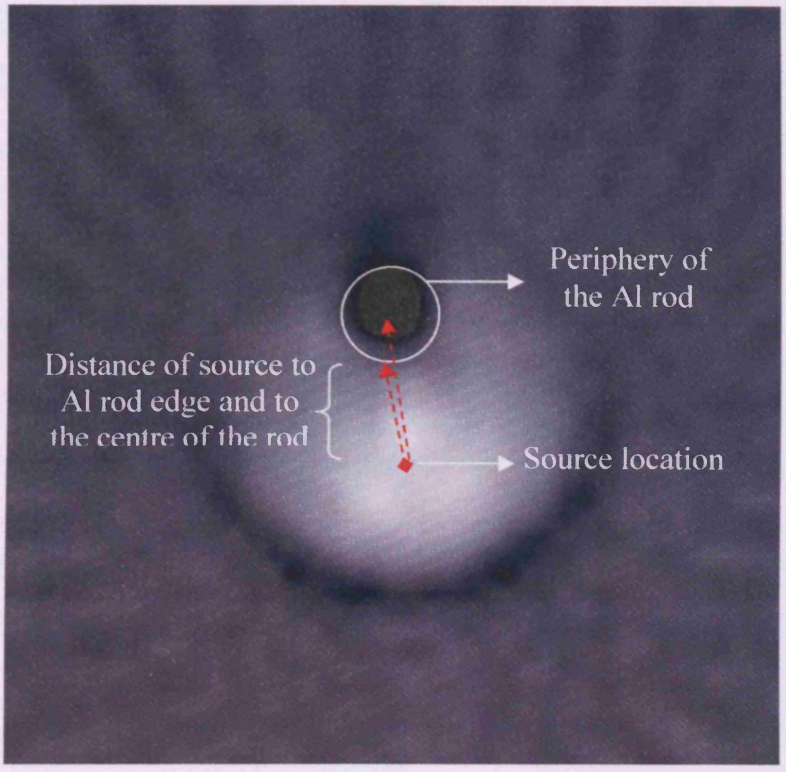

Figure 4.15 Image of the ^{241}Am source in the heterogeneous phantom. Landmark registration allows for the source to be localised on the image with respect to known geometrical distances. The profiler allows for the source and the centre and the edge of the Aluminium rod to be localised so that a coordinate system can be devised. The distance of the source to the edge and to the centre of the rod is computed and compared to the true geometric dimension

The landmark registration was undertaken in order to assist source localisation on the formed image. The resulting images describe the rod inserted in the phantom, allowing bone structures to be defined by the PECT imaging system. Alternatively, insertion of landmarks may be employed to register the source with respect these structures. The physical distance of the source to the edge of the rod and to the centre of the rod was as follows:

Source to Aluminium rod edge: 33.6 ± 0.1mm

Source to Aluminium rod centre: 43.1 ± 0.1mm

The results of the landmark registration of the source in the image are shown in Figure 4.16

4° acceptance angle@100 mm SDD

Detector Positions	No. of Projections	AL Edge	Al Centre
	18	N/A	N/A
5	36	40±7	49±8
	72	38±6	47±7
	18	37±6	47±6
10	36	35±6	45±6
	72	35±5	44±5
	18	35±4	45±4
20	36	34±2	44±3
	72	N/A	N/A

4° acceptance angle@200 mm SDD

Detector Positions	No. of Projections	AL Edge	Al Centre
	18	N/A	N/A
5	36	40±7	48±7
	72	37±6	47±7
	18	36±6	47±6
10	36	34±5	44±6
	72	34±5	44±5
	18	35±3	44±5
20	36	34±2	43±2
	72	N/A	N/A

8° acceptance angle@100 mm SDD

Detector Positions	No. of Projections	AL Edge	Al Centre
	18	N/A	N/A
5	36	39±6	48±7
	72	36±5	46±6
	18	36±5	46±6
10	36	35±5	45±5
	72	34±4	44±5
	18	33±3	44±3
20	36	33.9±1.9	43±2
	72	N/A	N/A

8° acceptance angle@200 mm SDD

Detector Positions	No. of Projections	AL Edge	Al Centre
	18	N/A	N/A
5	36	38±6	48±7
	72	35±5	46±5
	18	36±5	47±6
10	36	36±5	45± 5
	72	34±3	44±5
	18	33±3	44±4
20	36	33.4±1.1	43.1±1.5
	72	N/A	N/A

Figure 4.16 Results of ^{241}Am landmark registration. The values quoted are computed as a function of the distance of the source to the edge and to the centre of the Aluminium rod insert.

Landmark insertion plays an important role in the context of this work as it provides geometrical information about the source on the image. In an ideal clinical scenario, anatomical landmarks (e.g. the thorax in the case of breast IORT) could in theory be imaged, allowing for accurate computation of the distance of the source to the bone. This could assist in accurate derivation of the dose delivered to the bone. This is, in practice, a difficult task to undertake as it requires the detection system to be rotated around the patient (complete 2π

revolution). In the case of breast IORT where the patient under general anaesthesia is lying on the surgical bed, the imaging system cannot be implemented to record underneath the patient. It is therefore suggested that landmarks are manually inserted in order to provide the conditions for source localisation with respect to the inserted landmarks. This is similar to the markers employed in conventional BT radiographs so that the insertion of the seeds and their orientation can be cross-verified. Similar to the source localisation finding, landmark registration accuracy is enhanced with increasing angular projections and detector positions. However, contrary to the localisation results, landmark registration precision is increased with increasing collimator acceptance angle. A wider collimator acceptance angle results in a larger fraction of the emitted radiation to be recorded. This effect greatly enhances the description of the landmark on the image resulting in more accurate definition of the edge of the Aluminium rod as shown in Figure 4.15. Landmark registration accuracy is strongly dependent on source localisation as the distance of the measured source location to the landmark will be more accurately computed. As source localisation accuracy increases with increasing detector positions and angular projections, the accuracy of the computation of the distance from the source to the landmark increases. Consequently, the error in the measurement decreases as source localisation, and therefore landmark identification accuracy, increases. In the case of interstitial brain radiosurgery with the PRS, insertion of markers may not be required as the cranium bone surrounding the brain tissue might be employed as a natural existing landmark. In the case of breast IORT however, this is not applicable as the bone content lies beneath the breast tissue. Imaging, therefore, of the thorax is not possible with the PECT system as it would require rotation of the detection system under the surgical bed for the thorax to be imaged. External markers will thus have to be inserted for geometrical registration of the source on the resulting image.

4.1.6 Optimisation of the PECT detection system employing the ^{241}Am source.

The findings on the source localisation precision when using the ^{241}Am mono-energetic source indicate that a superior energy resolving detection system is preferable as distinction between primary and scattered radiation is possible. The *virtual source* image produced by omitting the primary photons from the integrated energy window during image reconstruction assists in accurate localisation of the source. Increasing the number of detector positions will greatly enhance source localisation as indicated by Figure 4.13. Localisation precision is increased with increasing number of detector positions. Increasing the number of angular projections will also result in increased localisation precision, however the effect of increasing the number of projections is not as crucial as the effect of increasing the number of detector positions per angular view. This is clearly demonstrated by the sharp increase of localisation precision with increased detector position compared to the increased number of angular projections as shown in Figure 4.13.

The optimal collimator settings suggest a narrow acceptance angle (4° to 8°), while the detector to source distance should preferably be kept to a minimum (e.g. 100 to 200 mm). This is due to the superior spatial resolution provided by the above restrictions, resulting in a more detailed integration of the phantom as it is scanned across the detector.

The accuracy of the ^{241}Am source localisation could still be adequate if a detection system with inferior energy resolution were to be used. Energy resolution is required for the formation of the *virtual source* image as stated previously. Integrating over the photopeak however, does not require superior energy resolution as shown in Figure 4.14. A scintillation detection system could not assist greatly in the selective reconstruction required to bring about the *virtual source* image, however integrating over the photopeak could still yield accurate source localisation provided that the statistical content of the data was acceptable. This could be achieved by increasing the number of angular views and more importantly detector positions, as stated previously.

In the case of single energy emitters, such as BT sources, the selection of the detection system is dependent on the amount of accuracy required for source localisation (e.g. the tolerance required by the user). It is expected that a superior energy resolving detection system can assist greatly in localising mono-energetic sources to well within 1mm. The scope of this work, however, is the ability to form an image using the PECT system in a relatively short time in order to be able to intervene should anomalies appear. The degree of accuracy might therefore be limited by the time required to form that image. Source localisation accuracy works as a trade off with the time required to form the image.

The optimal design of a clinical PECT system will be discussed at the end of this chapter, once the findings of the PRS source localisation are presented.

4.2 Precision of PRS400 Source Localisation using PECT

The results on the accuracy of the PRS source localisation using the PECT imaging system are discussed in this section. These are categorised in two sections; the results on the regular geometry phantom for both the homogeneous and the heterogeneous phantom are initially presented, followed by the results on the anthropomorphic brain phantom.

4.2.1 General observations from Spectral Acquisition of the PRS400 poly-energetic source

The spectral output of the PRS consists of characteristic x-rays as electrons impinge on the gold metal target together with a Brehmstrahlung continuum (or white spectrum). A typical spectrum of the PRS in air is shown in green in Figure 4.17. The effective energy of the continuous spectrum lies approximately between 1/2 and 1/3 of the maximum potential (Johns and Cunningham 1983). The spectrum in red demonstrates the exit spectrum of the PRS when positioned in the centre of the regular geometry phantom. The beam's effective energy increases (E_1= 21 keV, E_2=27 keV approximately) and the low energy photons are completely stopped within the phantom material (Nylon6/6). The sudden cut-off at the low energies of the green spectrum is due to the Low-Level Discriminator that has been applied to the amplifier so that noise induced by acoustic pick-up cannot compromise counting statistics. This does not affect the red spectrum since almost all photon energies below 15keV have been completely filtered out. The spectral output of the PRS in the phantom indicates that distinction between primary and scattered radiation in not possible, thus the high energy resolving ability of the HPGe is no longer necessary. It could be argued, however, that the scattered radiation content will be incorporated in the lower energy part of the spectrum.

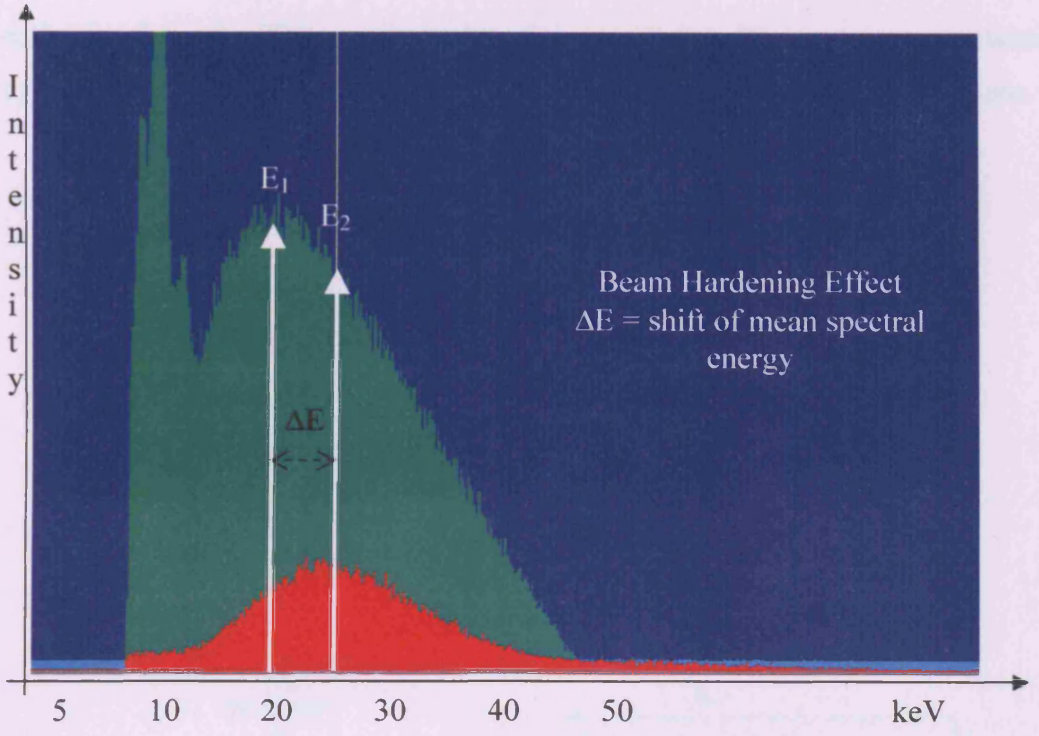

Figure 4.17 PRS spectra, in air (green) and in the phantom (red). The mean energy of the beam has increased (ΔE) and the low energy photons have been completely stopped.

Investigations have shown that selective reconstruction, i.e. drawing different energy windows on the resulting spectra, does not affect the resulting images. This implies that the distinctive content of the spectral information cannot be carried over in the reconstruction phase. Selective reconstruction therefore becomes obsolete in this case and, as such, the total spectral output needs to be integrated in the image formation. This simplifies the localisation problem, as comparison of scatter vs. primary images is no longer applicable and so cannot be assessed. The accuracy with which the PRS source can be localised in the regular phantom was again investigated using various scanning parameters. Identical experimental set-ups to the case of the ^{241}Am source were observed and the same manner of image analysis was carried out. Spectra collected at different projections through the phantom are illustrated in Figure 4.18. The same conditions of filtration apply as for the ^{241}Am source (see section 4.1). Data

collection from the PRS was limited by time constraints. The system was powered by a 12V NiCd Battery, which gave for about 4 hours of uninterrupted run time.

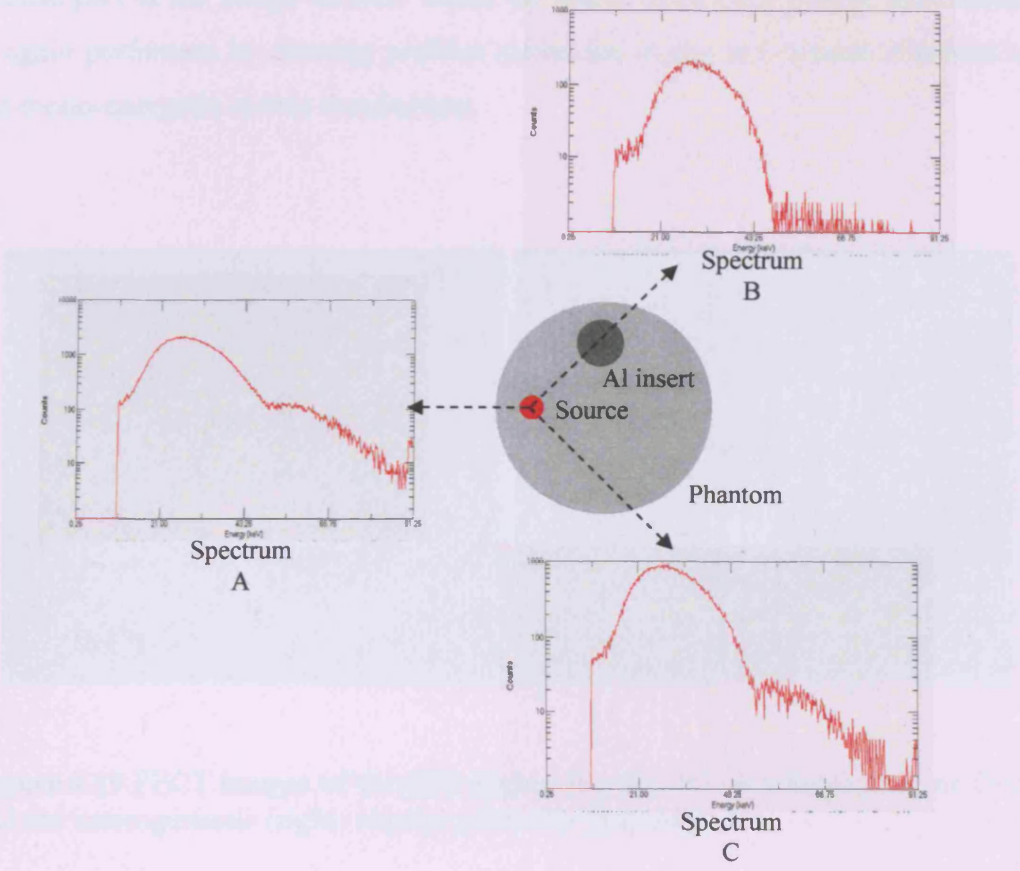

Figure 4.18 Spectral collection at various orientations around the heterogeneous phantom.

The high intensity of the probe, however, meant that lower acquisition times compared to those used with the ^{241}Am source could be employed, provided the detector was highly collimated. At the maximum kV setting (50 kVp), the radiation flux exiting the phantom can saturate the detector. Increased collimation of the detector is therefore required, and to alleviate this problem a High Rate Amplifier was also employed (Ortec, Model 973).

Counting at very high rates has a negative effect on the energy resolution of the detector system, but as resolution is of limited use in the PRS, this is not considered a major disadvantage. The resuting images from both the homogenous

and the heterogeneous phantom are shown in Figure 4.19. In this case the total spectrum was integrated. The periphery of the phantom is described, while the intense part of the image denotes where the source is located. Source localisation is again performed by drawing profiles across the image in a manner identical to the mono-energetic source localisation.

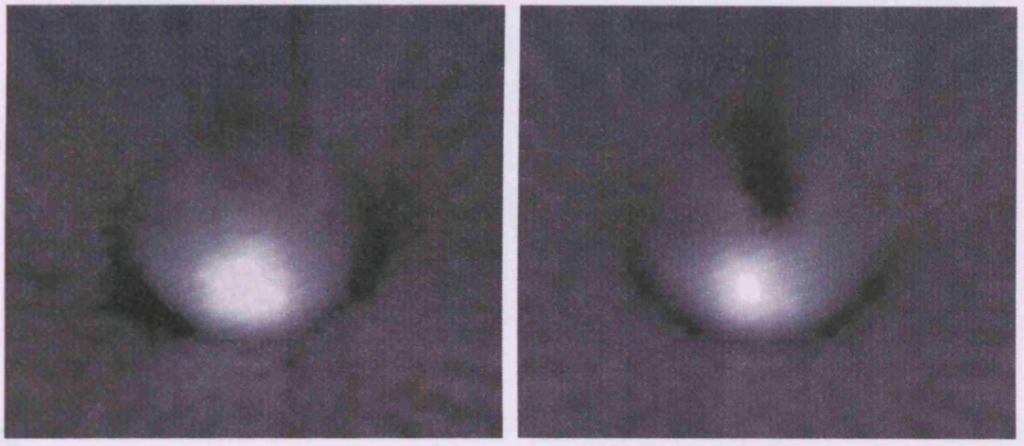

Figure 4.19 PECT images of the PRS source inserted into the homogeneous (left) and the heterogeneous (right) regular geometry phantom

The physical interactions that take place at the PRS energy range cannot be as clearly distinguished as in the ^{241}Am case. The probability of photon interaction is strongly dependent on the energy of the incident photon in the medium at hand. A breakdown of all possible photonic interactions at the energy range of the PRS system (50 kVp) is shown in Figure 4.20. Selection of different energy windows from the continuous PRS spectrum did not show any significant changes in the resulting images. Energy discrimination of the continuous PRS spectrum is not easily achieved, as the scattered part of the spectrum is incorporated in the total spectrum. It can however be assumed that the lower energy part of the spectrum will predominantly be comprised of scattered radiation, whilst the more energetic part of the spectrum is mainly comprised of primary photons.

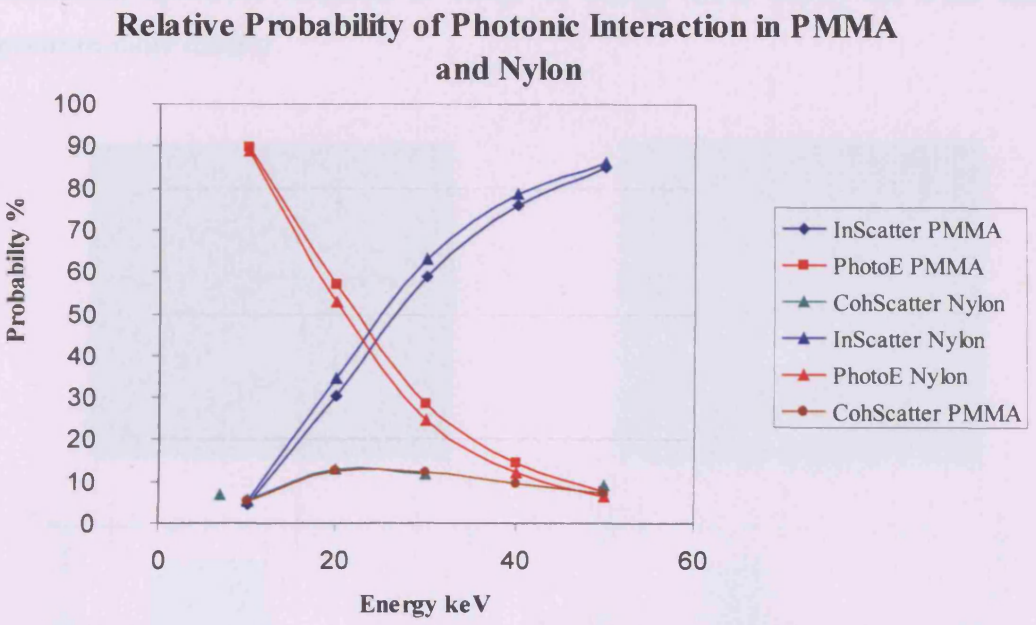

Figure 4.20 Relative probability of photonic interactions with phantom constituents (Nylon 6/6 and PMMA) in the PRS energy range (50 kVp). Photoelectric effect is the dominant interaction at lower energies, while the probability of inelastic scattering (Compton) increases with increasing energy.

The resulting images, as stated previously, did not show any definite or discrete changes as shown in Figure 4.21. The image on the top left is formed by integrating the part of the PRS spectrum shown in the grey shaded area, and similarly for the image on the top right. The bottom images are formed by integrating the lower and the higher energy part of the spectrum. The resulting images do not show great differences and it can therefore be deduced that selective reconstruction in the case of the PRS source cannot prove useful. The PECT images using the PRS as the emitting source were therefore formed using the whole of the exit spectrum. To demonstrate this fact, spectra were collected when the PRS was inserted into the anthropomorphic phantom using the Germanium detector and a scintillation based detector (NaI coupled to PMT tube) as shown in Figure 4.22 .The NaI spectrum spread over a wider range of energy channels, as expected due to its inferior energy resolving power, while the

Germaniun spectrum (defined in terms of energy flux) shows the PRS exit spectrum more clearly.

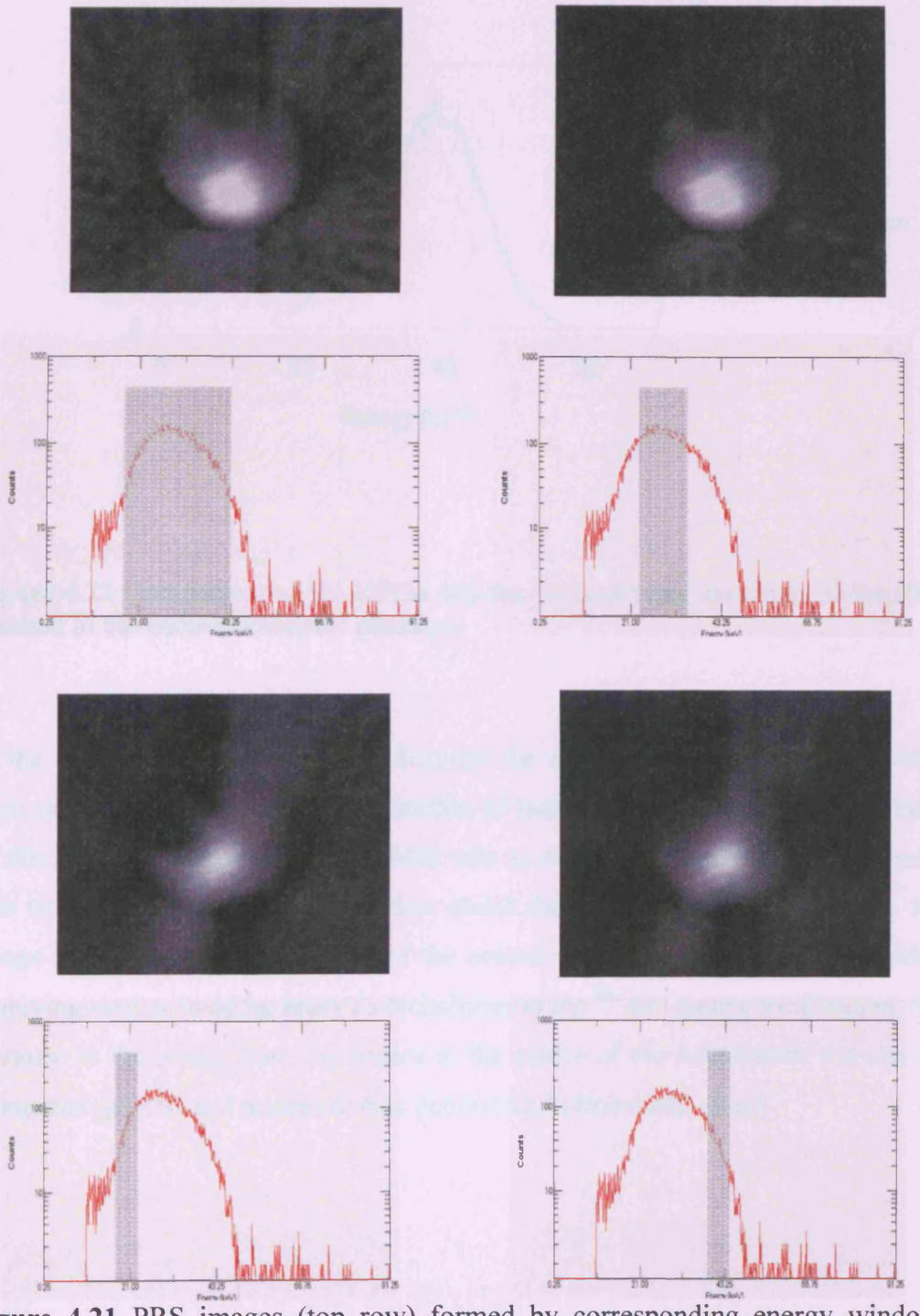

Figure 4.21 PRS images (top row) formed by corresponding energy window integrations (bottom row). Integrating over the whole or part of the PRS exit spectrum does not affect the resulting image. Integrating over the lower and the higher energy part of the spectrum again does not affect the images considerably

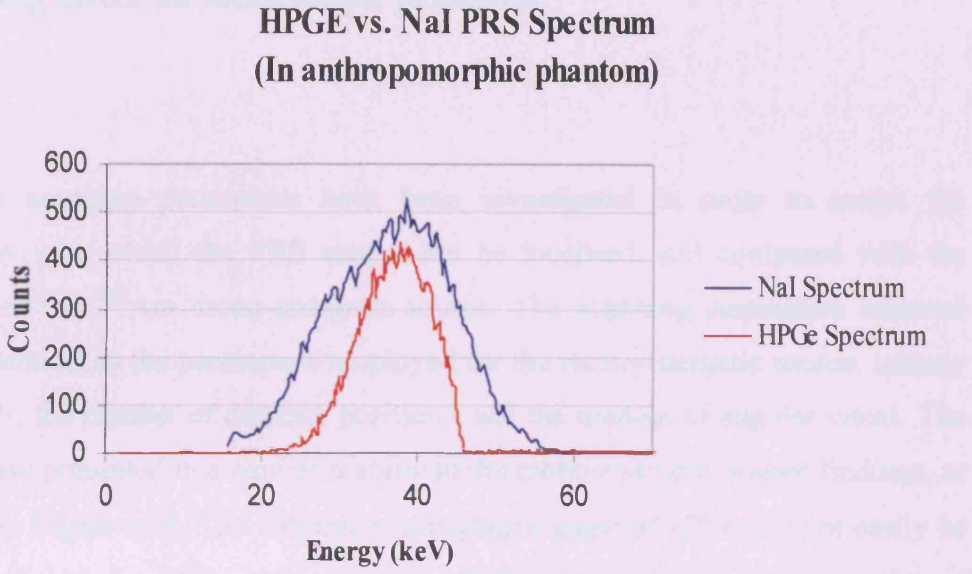

Figure 4.22 Comparison of the HPGe and the NaI collected spectrum of the PRS inserted in the anthropomorphic phantom

In the case of the heterogeneous phantom the aluminium rod is clearly visible. This can prove very useful in registration of landmarks using the PRS. Similarly in this case, the aluminium rod, which acts as a bone substitute in the phantom, can be utilised to extract information about the geometry of the source in the image by registering the location of the source with respect to these landmarks. Applying similar imaging analysis techniques to the ^{241}Am source localisation, the distance in the image from the source to the centre of the Aluminium rod can be computed (pixels) and related to true geometrical dimensions (mm).

4.2.2 Investigation on PECT scanning parameters and their resulting effect on localisation precision.

Various scanning parameters have been investigated in order to assess the accuracy with which the PRS source can be localised, and compared with the results of the ^{241}Am mono-energetic source. The scanning parameters assessed were identical to the parameters employed for the mono-energetic source, namely the FOV, the number of detector positions, and the number of angular views. The results are presented in a similar manner to the mono-energetic source findings, as shown in Figure 4.24. The collimator acceptance angle of 12° could not easily be employed with the PRS, as the increased FOV meant that a larger proportion of the exiting flux was detected, resulting in an increase in the detector dead time. When using this collimation set-up with the PRS, the implementation of the high rate amplifier could not improve the counting rates for source to detector distances smaller than 320mm. The photon detection efficiency at various collimator opening angles (FOV) was investigated. Results showed an inverse square relationship of efficiency to acceptance angle, as expected. The high intensity PRS x-ray output meant that the collimator opening angles are heavily restricted by the photon counting rates of the detection system as shown in Figure 4.23. A wide collimator acceptance angle results in a larger fraction of the PRS exit flux to be recorded. This has a negative effect on the counting rate of the Germanium detector and a high rate amplifier is required to compensate for the high photon flux, as discussed earlier. Moreover, the wider the collimator opening allows for a larger fraction of the scattered radiation to be recorded resulting in the description of the phantom periphery as well as the Aluminium inserts, as stated previously. Therefore increasing the opening of the collimator results in higher photon detection efficiency together with a better description of the medium in which the PRS source is inserted. The efficiency of the detector is calculated as the fraction of the FOV (i.e. collimator acceptance angle and SDD) to total PRS emission (4π) and is given as a function of collimator opening angle.

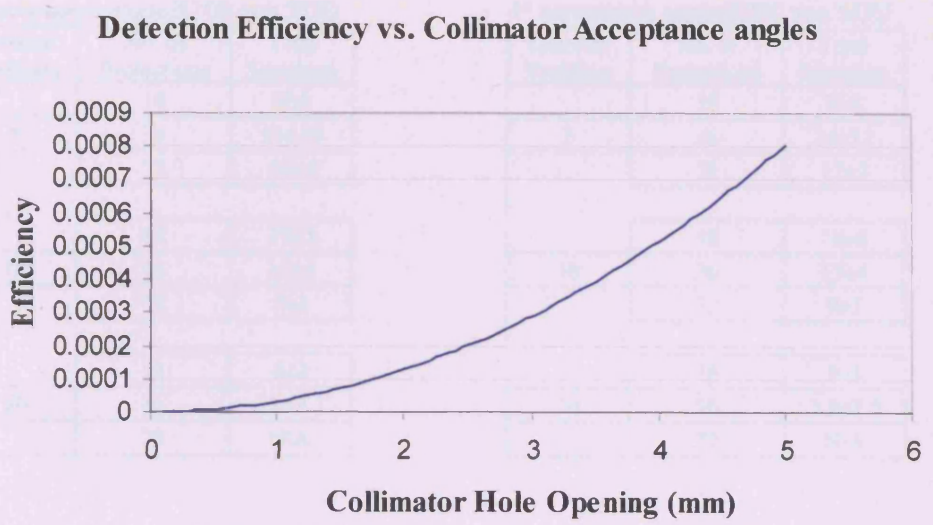

Figure 4.23 Efficiency of the HPGe detector at various collimator acceptance angles

Registration of the PRS source with respect to known landmarks was again carried out. Localisation of the PRS source employing external markers was performed using the profiler function in IDL. The distance of the source position to the marker was derived on the image and compared to physical dimensions. The results of the PRS source localisation using external markers are presented in Figure 4.24. Landmark registration was carried out by computing the distance of the source to the centre of the Aluminium rod insert and this was compared to the physical distance. The distance measured is the same as in the case of the mono-energetic Am source and is:

- Source to edge of Aluminium rod: 33.6 ± 0.1mm
- Source to centre of Aluminium rod: 43.1 ± 0.1mm

4° acceptance angle@100 mm SDD

Detector Positions	No. of Projections	Total Spectrum
	18	N\A
5	36	21±10
	72	16±5
	18	17±5
10	36	11±4
	72	7±3
	18	4±2
20	36	2.9±1.1
	72	N\A

4° acceptance angle@200 mm SDD

Detector Positions	No. of Projections	Total Spectrum
	18	N\A
5	36	24±11
	72	17±5
	18	18±6
10	36	13±4
	72	9±3
	18	5±3
20	36	3.3±1.5
	72	N\A

8° acceptance angle@100 mm SDD

Detector Positions	No. of Projections	Total Spectrum
	18	N\A
5	36	23±10
	72	18±7
	18	19±7
10	36	13±4
	72	8±2
	18	6±2
20	36	3.9±1.4
	72	N\A

8° acceptance angle@200 mm SDD

Detector Positions	No. of Projections	Total Spectrum
	18	N\A
5	36	25±10
	72	19±7
	18	20±8
10	36	15±6
	72	10 ±3
	18	7±3
20	36	4.2±1.7
	72	N\A

12° acceptance angle@320 mm SDD

Detector Positions	No. of Projections	Total Spectrum
	18	N\A
5	36	28±11
	72	19±8
	18	22±9
10	36	14±6
	72	9±4
	18	7±3
20	36	4.5±1.9
	72	N\A

Figure 4.24 Source localisation results for the PRS source embedded in the regular geometry homogeneous phantom. Results are presented as distance deviation (mm) from true source locations for all scanning settings.

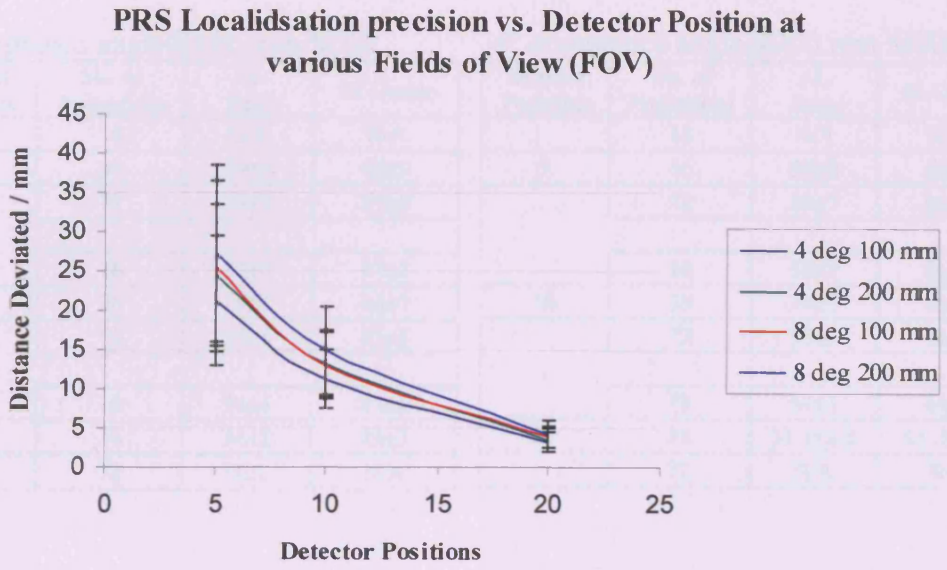

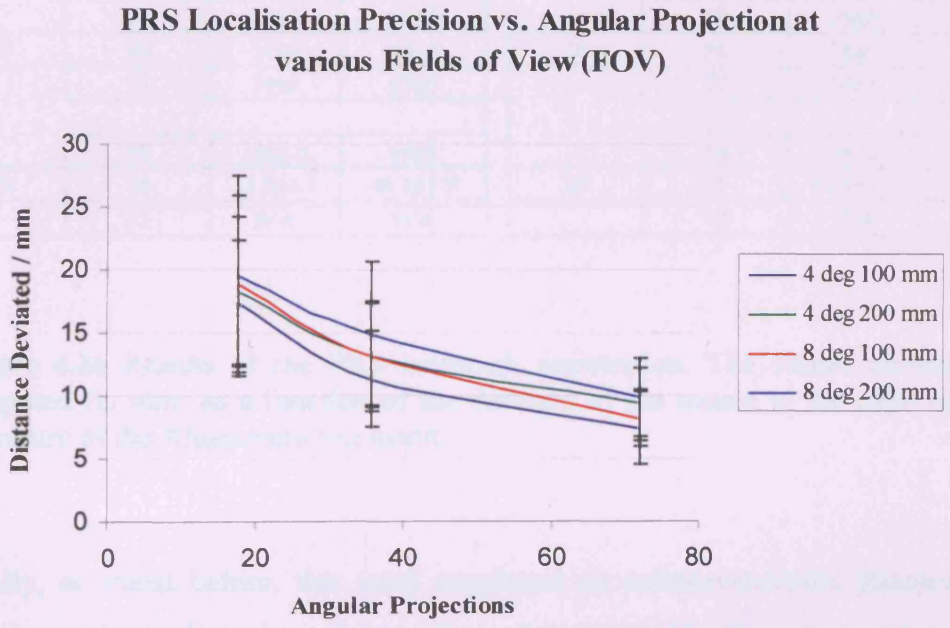

Figure 4.25 Effect of number of detector and number of angular projections on precision of PRS source localisation. Increasing the number of detector positions and angular projections results in enhanced precision of source localisation.

4° acceptance angle@100 mm SDD

Detector Positions	No. of Projections	AL Edge	Al Centre
	18	N/A	N/A
5	36	39±9	48±9
	72	38±7	47±8
	18	38±7	47±8
10	36	36±6	46±7
	72	35±5	45±5
	18	34±4	44±6
20	36	34±2	43±3
	72	N/A	N/A

4° acceptance angle@200 mm SDD

Detector Positions	No. of Projections	AL Edge	Al Centre
	18	N/A	N/A
5	36	38±8	48±8
	72	38±7	46±7
	18	38±7	46±7
10	36	36±5	46±6
	72	35±4	45±4
	18	34±3	44±3
20	36	33.1±1.5	43..3±1.1
	72	N/A	N/A

8° acceptance angle@100 mm SDD

Detector Positions	No. of Projections	AL Edge	Al Centre
	18	N/A	N/A
5	36	38±7	48±8
	72	36±6	46±8
	18	35±5	46±6
10	36	34±4	45±6
	72	34±3	45±5
	18	34±3.0	44±3
20	36	33.5±1.1	44.1±1.9
	72	N/A	N/A

8° acceptance angle@200 mm SDD

Detector Positions	No. of Projections	AL Edge	Al Centre
	18	N/A	N/A
5	36	38±7	48±8
	72	36±5	46±7
	18	35±5	47±5
10	36	34±5	45±4
	72	34±3	45±4
	18	34±2	45±3
20	36	34.1±1.7	44.5±1.4
	72	N/A	N/A

Figure 4.26 Results of the PRS landmark registration. The values quoted are computed (in mm) as a function of the distance of the source to the edge and to the centre of the Aluminium rod insert.

Finally, as stated before, this work employed an anthropomorphic phantom to simulate realistic clinical conditions. The anthropomorphic phantom was designed based on a real human cranium as discussed in Chapter 2. Aluminium insertion was therefore not necessary in this case as the bone content of the cranium acts as a natural landmark. Landmark registration in the resulting image was carried out

by computing the distance of the source to the periphery of the skull in both the x and the y axis as shown in Figure 4.27.

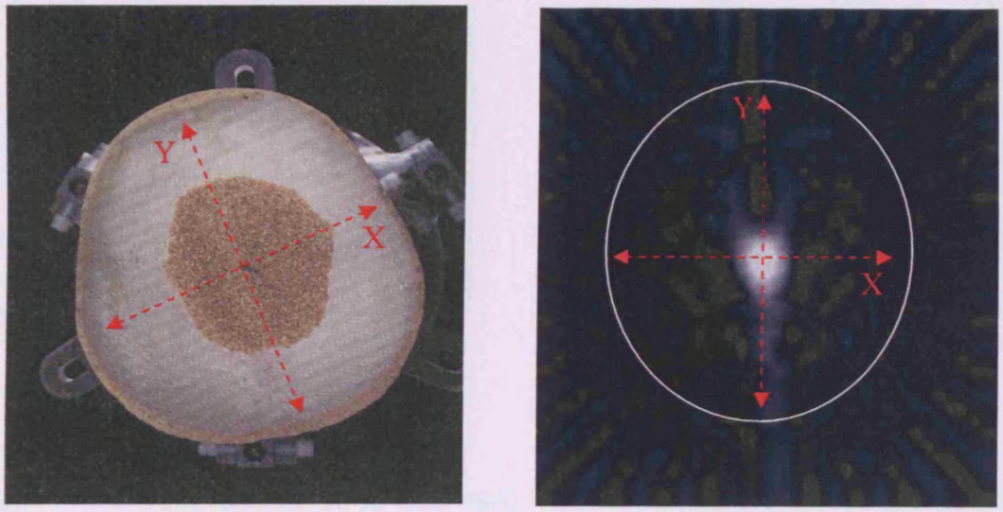

Figure 4.27 The physical dimensions of the cranium (left picture) were measured and compared to the image formed (right picture). The skull is filled with tissue equivalent (TE) material (Lincolnshire Bolus). The tip of the probe can be seen at the intersection of the two axes. The bone content of the skull was used in this case (defined with the white line for presentation purposes) in order to register the source with respect to anatomical markers.

The physical distance from the tip of the probe to the edge of the skull in both the x and the y axis are as follows:

X= 57.2 ± 0.1mm

Y= 70.5 ± 0.1mm

The image formed using the anthropomorphic phantom describes the periphery of the skull as shown in Figure 4.27. It is possible therefore to employ the skull as the landmark (no external markers required). In the case of the breast this natural landmark is not available, so external markers need to be inserted for landmark registration.

4° acceptance angle @ 100 mm SDD

Detector Position	No. of Projection	X axis	Y axis
	18	N/A	N/A
5	36	61±8	73±8
	72	60±6	72±7
	18	61±6	72±6
10	36	59±5	71±6
	72	58±4	70 ±5
	18	57±3	70±4
20	36	57±2	70±3
	72	N/A	N/A

4° acceptance angle @ 200 mm SDD

Detector Position	No. of Projection	X axis	Y axis
	18	N/A	N/A
5	36	61±6	73±7
	72	60±6	72±6
	18	61±5	72±5
10	36	59±4	71±5
	72	58±4	71±4
	18	57±2	71±3
20	36	57.5±1.5	70.9±1.7
	72	N/A	N/A

Figure 4.28 Results of the PRS landmark registration using the anthropomorphic phantom. Distance of the source to the skull periphery (quoted in mm) in both the x and y axes.

4.3 Optimisation of the PECT detection system based on experimental findings

Results on PRS localisation showed that the localisation precision can be greatly improved by increasing the statistical content of the acquired data. Similar to the ^{241}Am findings, increasing the number of detector positions results in superior source localisation precision. Increasing the number of angular views will also improve the localisation accuracy considerably, though the effect is not as dominant as increasing the detector positions. This becomes an important issue when designing the optimal detection system for PECT imaging.

The purpose of the investigation into the experimental scanning parameters and their effect on the precision of source localisation was to assist in identifying the

most suitable PECT detection system. In section 4.1.6 the implication of using a fast read-out system in order to produce an image with a good degree of source localisation accuracy was discussed. The aim of this work was to be able to monitor, and if possible modify the dose deposition of the PRS system during a clinical treatment. For this to happen, the overall data acquisition should occur in the first phase of the treatment. This implies that the PECT scanning system designed for the laboratory investigation needs to be considerably altered. Scanning components, i.e. linear and rotary motion stages, are extremely cumbersome to operate under clinical (sterile) conditions. Setting up such a detection system would require time to ensure good source-detector alignment and centre of rotation corrections, resulting in extended sedation periods for the patient being treated. Having considered all of the above findings related to scanning parameters, acquisition times and image formation, a new approach is needed in the attempt to devise a PECT clinical system. The new design needs to address three important parameters:

- Setting up or installation of the PECT system around the PRS
- Required Data acquisition times
- Image formation and analysis

The resulting image will be employed in order to obtain information regarding the PRS dose deposition during the actual treatment. This is an added burden to the overall time required for the PECT system to provide a quick indication that the PRS is functioning properly. This is probably the most important aspect of the PECT system if it is to provide real-time monitoring capabilities. The proposed PECT system is therefore based on the findings of this work, but is mostly driven by the need for real time dose monitoring which is the essence of this work. As stated previously, the step and shoot ECT modality employed in the laboratory is no longer ergonomically feasible and needs to be revised.

Based on the above three criteria and bearing in mind the goals and aspirations of the PECT system, the proposed detection system for on-line image formation and dose map computation of the PRS during a treatment is driven by the following parameters:

- Choice of detector
- Detector array arrangement
- Detector collimation
- Read-out electronics
- Sterilisation issues

The detector choice is based on the fact that energy resolution is not a requirement as the system cannot distinguish primary and scattered radiation in the polychromatic PRS output. This is regarded as an advantage as energy resolving detector materials (e.g. HPGe) are expensive to purchase and difficult to construct into the desired array. Much more easily accessible scintillation crystals can be used instead to provide the high photon counting statistics required in this work. A circular array of such detectors can easily be constructed and would provide efficient data collection in a relatively short time. The collimation system employed in conjunction with the proposed detector ring needs to be carefully considered. The annular ring of detectors around the PRS source is employed in order to avoid rotation of the imaging system around the source, thus minimising mechanical motion in the vicinity of the patient. It is therefore proposed that an array of collimators be employed in order to simulate the detector positions at each projection. This can be achieved by coupling the collimator array onto the detector ring. Having the ability to rotate the collimator array over the detection ring, will result in increasing the number of detectors thus improving localisation precision as predicted by the localisation findings in Chapter 4. The rotation of the collimators however, is not an easy task to be carried out under clinical conditions as it requires mechanical motors to drive the collimation system.

The read-out electronics coupled to the detectors need not take up a lot of space, allowing surgeons ample room to attend to the patient during the PECT set-up.

Finally, the transfer of the data onto a portable workstation (laptop PC) for on-line image reconstruction can easily be carried out in the operating theatre, allowing a real-time PRS exit flux image to be formed in a relatively short time. One major obstacle that cannot be overcome is the fact that the ring of detectors cannot be aligned at the PRS source level, which is buried in the body, as shown in the proposed clinical PECT diagram in Figure 4.29. It will be very difficult to align the detector at the source level as this would require the detector ring to be resting on the patient's body. This is not advisable as the many electronic connections (possibly carrying hundreds of volts to power the crystals) to the detectors would possible come in touch with the patient. The detector ring can be fixed onto the PRS gantry, and the collimators coupled to the detector crystals can be focused onto the PRS source lying underneath the ring, as shown in Figure 4.29. The ring of detectors can be placed at any distance between 100 and 200 mm away from the source. A collimator acceptance angle of 4 degrees can provide sufficient spatial resolution. This, however, could be altered depending on the size of the active crystal of the detector material. A small diameter crystal requires a smaller collimator and the whole detection system can be scaled down to the appropriate detector size. The read-out electronics can be housed on top of the detector ring so that they do not interfere with the detectors field of view (FOV). Sterilisation issues involved with this detector construction need to be carefully addressed. This problem could be overcome by draping the ring of detectors with an appropriate material, rendering the overall imaging system sterile thus allowing it to be placed close to the PRS source and the patient.

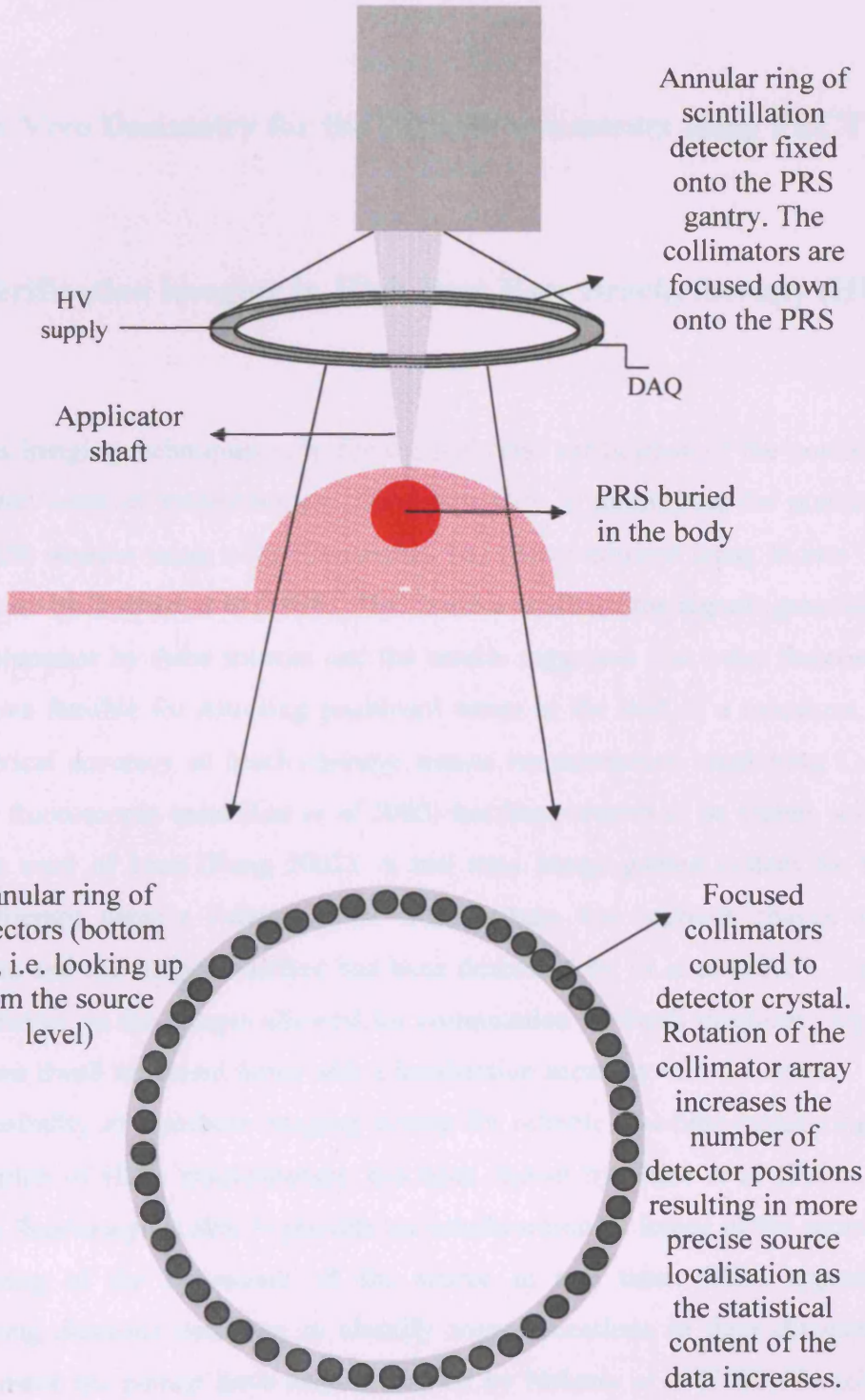

Figure 4.29 Proposed clinical PECT system. An annular ring of scintillation detectors with collimators focused down at the source level is shown. The side view of the system is shown at the top while the detector ring seen from the bottom up is shown at the bottom.

CHAPTER 5

In-Vivo Dosimetry for the PRS400 treatments using PECT

5.1 Verification Imaging in High Dose Rate Brachytherapy (HDR)

Various imaging techniques exist for the real time verification of the position of implanted seeds in brachytherapy. The practicality of monitoring the position of ^{192}Ir HDR sources using x-ray fluoroscopy has been evaluated using Monte Carlo techniques by Bagheri *et al* (1998). Their model predicted the signals generated in a CsI phosphor by these sources and the results suggested that x-ray fluoroscopy can prove feasible for detecting positional errors at the start of a treatment. The geometrical accuracy of brachytherapy source reconstruction employing C-Arm mobile fluoroscopic units (Liu *et al* 2003) has been shown to be viable, with an average error of 1mm (Fung 2002). A real time image guided system for HDR brachytherapy using a 3-dimensional video camera that captures images of the catheters and the surgical surface has been described by Li *et al* (2003). Tracing the catheters on the images allowed for computation of dwell positions, together with their dwell treatment times with a localisation accuracy of $\sigma < 1.5$mm.

The feasibility of a pinhole imaging system for reliable real-time monitoring and verification of HDR brachytherapy has been shown by Duan *et al* (2001). The pinhole fluoroscope is able to provide an autofluoroscopic image of the source for monitoring of the movement of the source in real time. Other approaches employing diamond detectors to identify source locations in three-dimensional space inside the patient have been described by Nakano *et al* (2003).To achieve high positional resolution, Nakano *et al* showed that the detectors should be placed as close as possible to the source and accurate source localisation is achieved when all lines of sight from the detectors to the source are as near to orthogonal as possible (Nakano *et al* 2005). The accuracy of such source

localisation depends strongly on the number of detectors and agrees with the localisation findings presented in Chapter 4 (Nakano *et al* 2005). The diamond detectors act as calibrated dosimeters (due to the detector's tissue like characteristics) to record the expected dose at the detector locations for comparison with expected values. Intra-operative dynamic dosimetry for prostate implants has been suggested by Todor *et al* (2003), suggesting that a paradigm shift from standard pre-planning to real time planning using dosimetric feedback based on the actual deposited seed positions within the prostate is taking place. This relies on bringing planning and evaluation into the treatment room (i.e. making post-implant evaluation superfluous), allowing rectifications to be made by employing the same imaging system (e.g. ultrasound). Dosimetric evaluation is therefore possible by fusion of ultrasonic images with 3D source coordinates reconstructed from fluoroscopic projections.

A system of non-radiographic source localisation for real time HDR monitoring realised by the implementation of an electromagnetic tracking device has been suggested by Watanabe *et al* (1997). This system consists of a transmitter coil, a receiver coil and a signal processing unit to generate the coordinates and the orientation of the transmitter, however it is sensitive to neighbouring metallic structures.

The ease of handling of the PRS source (controllable x-ray emission, manual insertion) could allow for a verification imaging system that monitors the delivery of the radiation in real time, i.e. during treatment. The shift towards real time monitoring of BT treatments has become more evident and this encourages the work investigation of such an imaging system that would allow the aforementioned capabilities.

5.2 Monte Carlo Simulations and the PECT Transform Map

In the previous chapter it was shown that the PRS source can be imaged within a representation of the patient using an ECT technique. Furthermore, analysis on the

image resulted in the source location being identified to within 3mm using "patient" landmarks. The image created can provide additional information other than the source localisation as well as possible landmark registration. This is because the image formed is an intensity map of the radiation emitted at all points in the phantom. This radiation, both primary and scatter, will be responsible for the deposition of energy in the phantom and thus source localisation can be used to map the dose. Thus information on dose delivery could be extracted during the image acquisition and an in-vivo dosimetric check of the treatment could be obtained. For this to happen, a correlation of the image to the dose map is necessary. In this work, this relationship is referred to as the Portal Emission Computed Tomography Transform Map (PECT- Transform Map). Fast data acquisition and on-line image reconstruction could allow for real-time dose delivery checks, together with a post treatment dose verification record of the actual dose delivered. The relationship of the image to the dose map cannot easily be computed, although the computation of the PRS output is a relatively easy task. Depth dose data has been obtained using the dedicated water tank provided by the manufacturer (see Chapter 1). Manipulating this dosimetric information in order to relate it to a PECT image is not straightforward as scattering from inhomogenities needs to be considered; alternative techniques need to be employed in order to derive an empirical relationship between the photon distribution in the image and the dose map. The correlation of one to the other needs to be carried out under known, predefined, controlled conditions. Monte Carlo simulations need to be employed in order to achieve this goal.

To ensure that the PECT transform map is derived under the same conditions, the PRS image creation was also modelled. If the theoretical image of the PRS in the phantom is replicated and reproduced by Monte Carlo and the computed dose map of the PRS photons in that same phantom is obtained, then a direct relation of one to the other can be achieved. The procedure used Monte Carlo simulations to provide spectral output of the PRS in the uniform homogenous phantom. These spectra were then imported into IDL for image reconstruction in the same way as discussed in Chapter 3. The dose map, as obtained by the Monte Carlo model, can also be imported to IDL and a comparison made. A transform map can then easily

be obtained by finding the relationship between the two images under certain boundary conditions. The IDL code provides the aforementioned controlled conditions necessary for correct derivation of the transform map. This is because the code creates both images according to the photon intensities, either as intensity photons in the spectral acquisition or as dose values in the dose map. The resulting images are pictorially presented using the same colour table (IDL: tvcsl) and so any perturbing effects during image reconstruction can be avoided. There are issues that need to be carefully considered before the transform map can be accurately derived. Firstly, the collection of the spectra and the resulting image formation need to be accurately implemented. The images are then formed based on the same reconstruction algorithm as the measured spectra. The PRS deposits most of its dose very locally, i.e. to within 30-40 mm's of the edge of the probe, which means that for correct derivation of the transform map, the spectral image needs to be accurately segmented such that the area of interest (i.e. equal to the dose map area) is solely extracted. Monte Carlo simulation showed that approximately 90% of the PRS emitted flux will be absorbed by the medium. The segmented image of equal dimensions to the dose map is then superimposed and divided by the dose map image in order to compute the transform map correctly. As stated before, this can lead to the empirical transform map derivation, computed under the same conditions. Direct transformation of the image to the dose map can then, in theory, be implemented for real-time monitoring during any PRS treatment. The Monte Carlo modelling was therefore divided into two sections; the first task was to reproduce the photon emissions of the PRS source from the uniform phantom. The image reconstruction was then carried out and these images compared to the measured ones. The next step required that the dosimetric model be properly optimised and checked against the measured values. This is achieved by comparison of dose maps created by the model in water and the experimentally measured depth doses in the water phantom. Once the model correlates to measured data, the dose map of the PRS in the regular geometry homogenous phantom can be confidently computed. The last step requires the segmentation of the escaped photon image the accurate superpositioning with respect to the dose map image such that the transform map can be derived.

5.2.1 Monte Carlo Spectral Collection

In order to optimise the Monte Carlo code and to ensure that the resulting spectra are correct, the ^{241}Am source was used first. The reason for this is that the incident photon energy is effectively mono-energetic (E (incident) =0.05954 MeV), with the lower energy emissions filtered out. Therefore, the resulting Monte Carlo spectra can be directly compared to the measured ones and the scattered radiation can easily be identified. Insertion of the PRS source was then carried out. This was achieved by using the measured in-air PRS spectrum as the input data file for the Monte Carlo code. The PRS spectrum, as collected using the HPGe detector, was inserted as a function of the cumulative probability photon energy distribution. This was obtained by dividing the cumulative summed photons at every energy bin by the total number of counts in the whole spectrum, creating a probability distribution between the values of 0 and 1, as shown in Figure 5.2. The computational process of the Monte Carlo code randomly selects a number between these limits and this is then directly translated to a given photon energy. A photon of this energy is then followed and its history recorded. The experimental set-up devised was simulated using the EGSnrc-Generic User Code (GEN_UC) designed by Fragoso *et al* at the Institute of Cancer Research, the Royal Marsden NHS Trust (2002). The geometry chosen for this work was that of a large circular cylinder comprised of smaller diameter cylinders placed in off-centre positions as shown in Figure 5.1. This is a direct simulation of the phantom employed in the laboratory (and should be compared to Figure 3.3). The various diameter inserts represent the positions the heterogeneous regions. The HPGe detector was simulated as a ring of Germanium at a specified distance from the edge of the phantom. The dimensions of the actual detector crystal were chosen to be identical to the detector crystal employed in the laboratory (10mm thickness, 36mm height). The detector ring was positioned at the source location plane i.e. in the middle of the phantom. The collimator system employed in the laboratory simulations was not inserted into the geometry model because computational times for a single study would have been too high. Many photons would be

rejected by the collimator system and this would have been wasteful of computer time. Optimisation of the simulation code is required for maximisation of the data collection within a reasonable computational time (~ few hours). The collimation of the collected spectra was taken into account in a later stage.

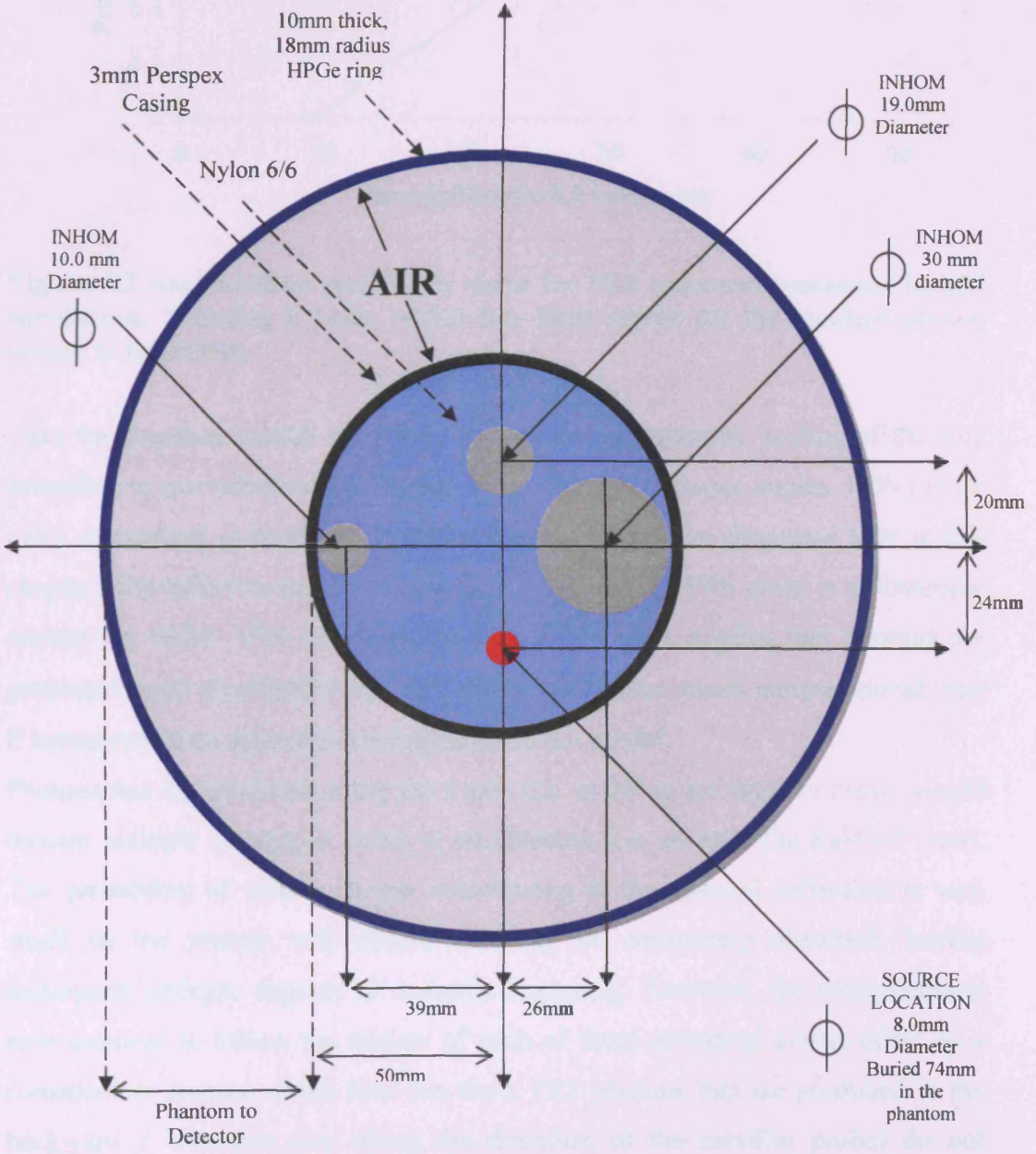

Figure 5.1 Schematic of the geometry modelled for the experimental set-up. The source is positioned 24mm off-centre and is inserted in the axial middle of the phantom. The HPGe detector is made of a small ring positioned at the source plane (middle of phantom). The collimator system employed in the laboratory was not modelled.

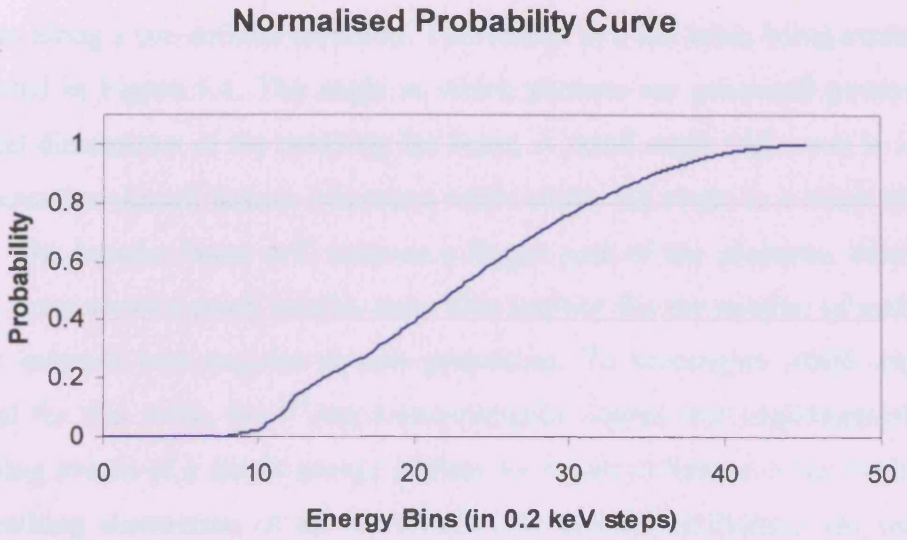

Figure 5.2 Accumulative probability curve for PRS spectrum generation in MC simulations. Selecting a value within this limit allows for the incident photon energy to be defined.

Once the acquired spectra are ported into an IDL programme, sorting of the data according to pre-selective collimation parameters (acceptance angles, FOV) is far more economical in terms of computer usage. This will be discussed later in this chapter. The radiation source in both the ^{241}Am and the PRS cases is an isotropic emitter (to within 10% in the case of the PRS). This implies that photons are generated in all directions (4π). This again will require much computational time if isotropic photon generation is requested in the model.

Photons that are produced along the z axis (i.e. at 90° to the detector plane) would require multiple scatters in order to be detected (i.e. re-enter the field of view). The probability of such a photon contributing to the spectral collection is very small as the photon will almost certainly be completely absorbed, having undergone multiple degrees of inelastic scattering. However, the computational time required to follow the history of each of these unwanted events takes up a considerable amount of the total run-time. PRS photons that are produced in the backward Z direction (i.e. along the direction of the metallic probe) do not contribute to the image formation. Perturbing effects due to photon interactions with the metallic nature of the drift tube will predominate. These again are unwanted events and need not be incorporated. To optimise the code in this case, photon generation over a restricted angular range is required in order to produce

photons along a pre-defined direction. This results in a fan beam being created, as illustrated in Figure 5.4. The angle at which photons are generated governs the physical dimensions of the resulting fan beam. A small angle will result in a finer beam creation (pencil beam), whereas a wider angle will result in a much broader beam. The broader beam will traverse a bigger part of the phantom, whereas a pencil beam views a much smaller area. This implies that the number of scattering events increase with angular photon generation. To investigate which angle is optimal for this work, the ^{241}Am mono-energetic source was implemented. The scattering events of a single energy photon are easier to follow in the model and the resulting summation of all the events (i.e. spectral collection) can indicate which angle produces the desired effect. The resulting spectra created are shown in Figure 5.3.

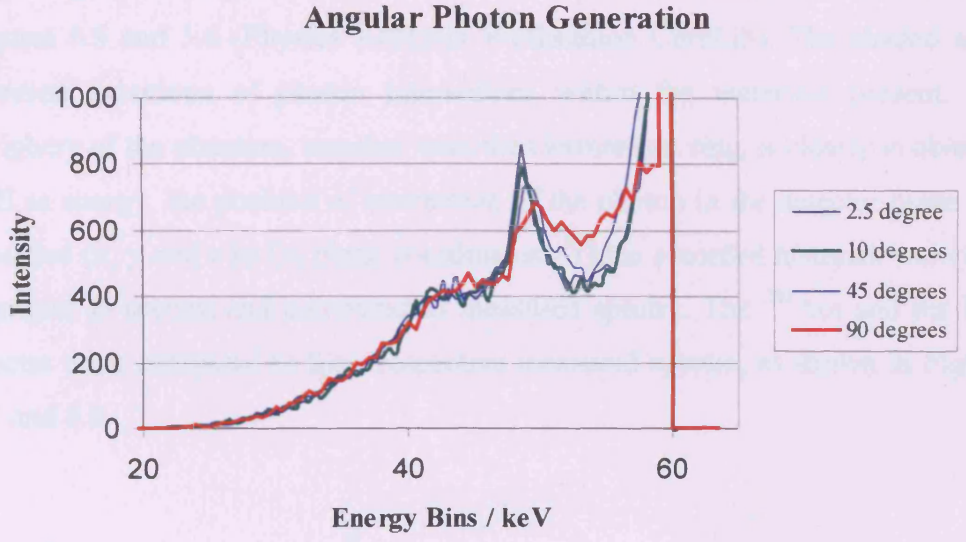

Figure 5.3 Monte Carlo generated ^{241}Am spectra at various angles. The scatter content of the spectra increases with increasing angle. The optimal angle for photon generation was 45°. This setting was kept constant for the PRS spectral studies.

The amount of scatter content in the spectra increases as the angular photon generation increases, as predicted. The scatter content of the spectrum is a vital piece of information required for selective reconstruction of the mono-energetic beam. The choice of the optimal angle is based on two criteria: the ergonomics of

the computer power available, as run times will be prolonged for wide angular photon generation and the collimation system employed in the laboratory resulting in a given FOV formed at the phantom. The projected solid angle of the emitted photon flux must overlap with the FOV of the imaging system as illustrated in Figure 5.4. The choice of 45-degree angular photon generation was chosen as the optimal setting. This ensured fast computation times for the number of histories required, whilst enabling the fan beam to cover the total field of view of the collimation. The detector was simulated as a circular ring of Germanium, as stated previously. The function of the peripheral electronics (Pre-Amplifier, Amplifier, MCA, etc), together with the induced electronic noise and its propagation, which must be incorporated in the image formation, was not considered in the model. Photon histories were recorded once a photon reached the Germanium region only. A graphical representation (GUI) of the generated histories is presented in Figures 5.5 and 5.6 (Physics Analysis Workstation CernLib). The shaded areas represent positions of photon interactions within the materials present. The periphery of the phantom, together with the Germanium ring, is clearly visible. As well as energy, the position of interaction of the photon in the detector plane was recorded (x, y and z in Ge plane coordinates). These recorded histories were then arranged as spectra and compared to measured spectra. The ^{241}Am and the PRS spectra were compared to their respective measured spectra, as shown in Figures 5.7 and 5.8.

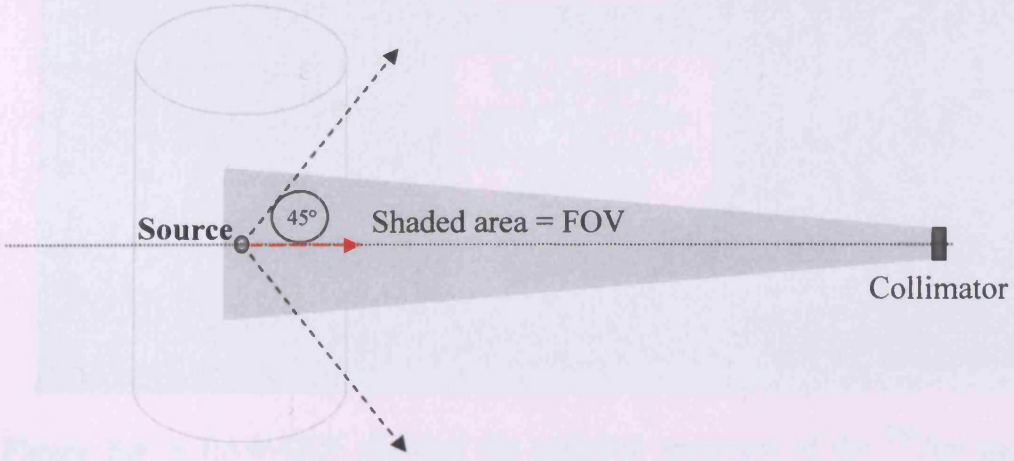

Figure 5.4 45° degree angular photon generations. At this setting, the projected FOV of the collimator system overlaps the solid angle photon flux ensuring proper photon history generation.

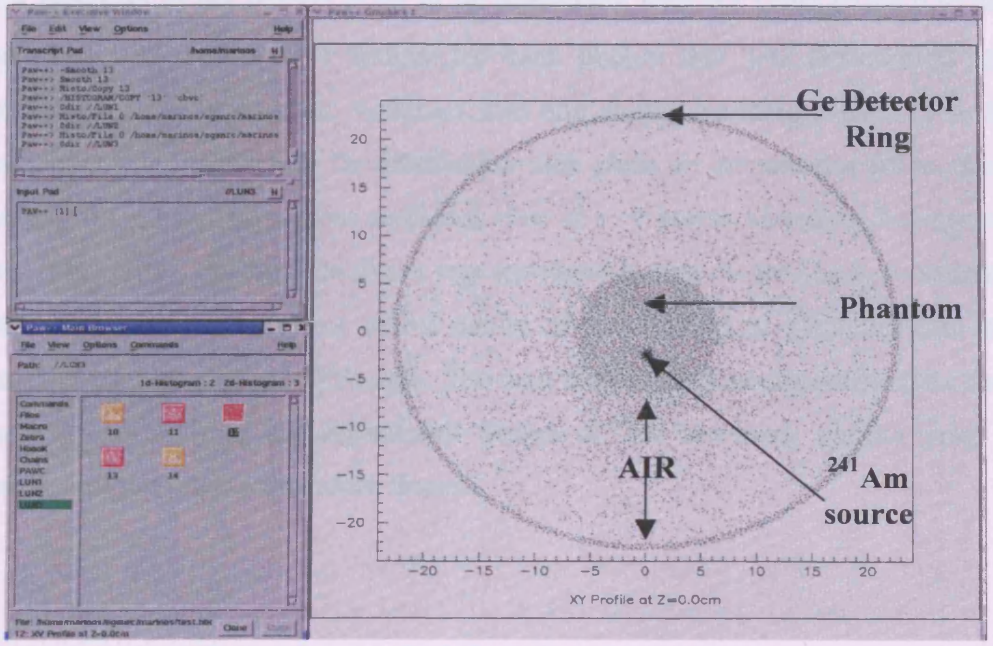

Figure 5.5 A PAW-GUI showing the XY profile of the data collected at the z = 0 plane (detector plane). Every dot represents a point of inelastic interaction according to the photon history recorded. The periphery of the detector ring is shown. The phantom structure is also described. The position of the source can be seen as the dark spot near the centre of the phantom.

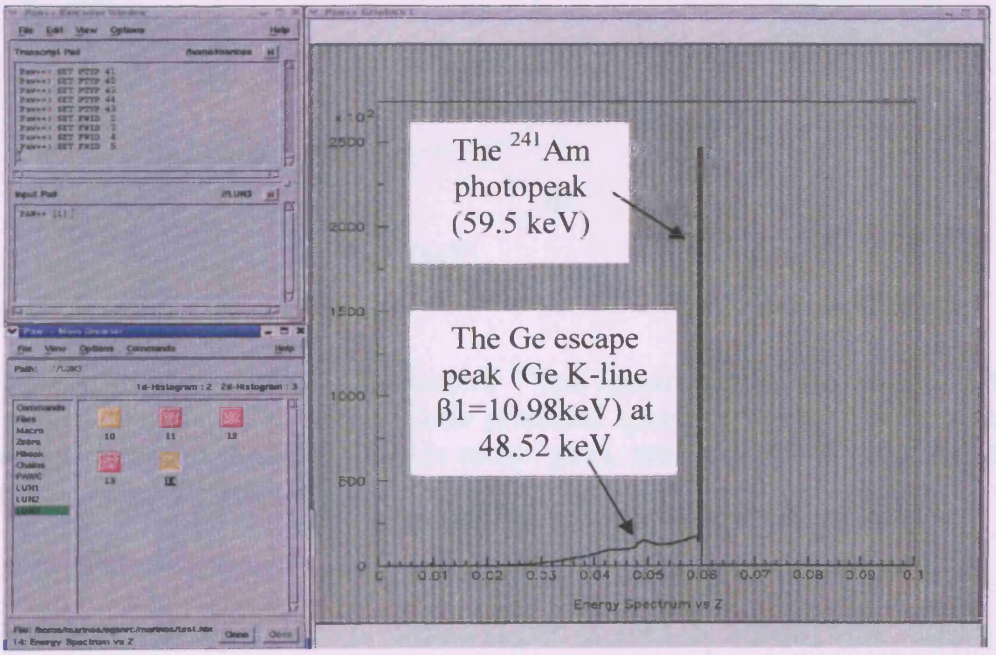

Figure 5.6 A PAW-GUI showing the emission spectrum of the ^{241}Am mono-energetic source inserted in the uniform, homogeneous phantom. The photopeak (59.5 keV) is shown together with the Ge escape peak (to the left of the main photopeak).

The direction of the photon prior to its interaction with the Germanium was also recorded. This produced a history for each photon that was represented as a function of six geometrical variables and one energy variable. The x, y and z coordinates denoted where the interaction took place on the detector plane. Since the radius (or height if a cross-sectional view at z =0 is considered) of the detector ring was 18mm, this implied that z was restricted in that range. These coordinates were computed with respect of the centre of the cylindrical geometry that was implemented by EGSnrc GEN-UC. The next three variables represented the three polar coordinates of the directional vector of the incoming photon prior to interaction with the Germanium atoms.

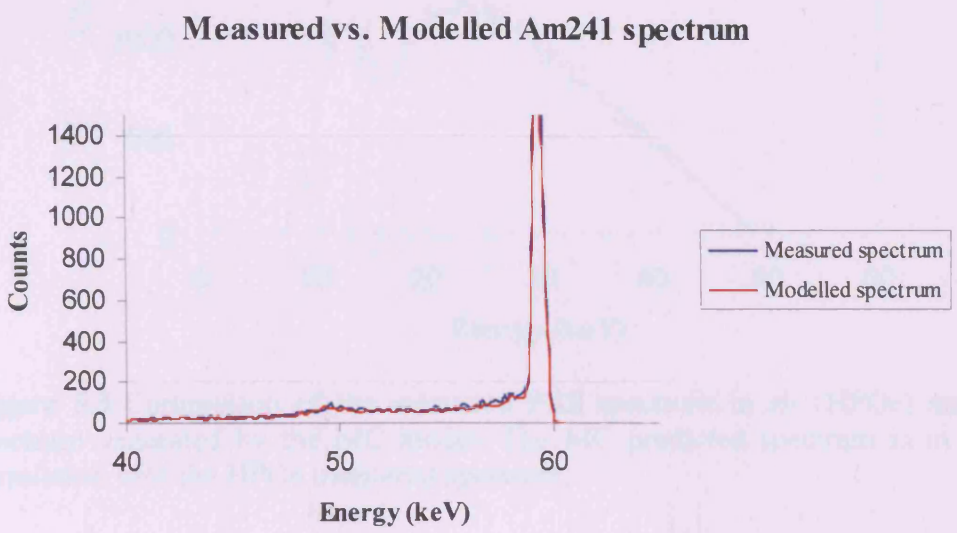

Figure 5.7 EGSnrc GEN_UC generated ^{241}Am spectrum compared to the HPGe measured spectrum. The Monte Carlo predicted spectrum is in good agreement with the measured spectrum. The Ge escape peak, predicted by MC, confirms the model is optimally performing.

Quantities U, V and W are the cosine angles (quoted in radians) with respect to the X, Y and the Z-axis respectively. These three directional quantities carry information on the direction of the photon and play an important role in sorting photons to determine if the collimator acceptance angle allows a given photon to

contribute to the image. The output file is in binary format. This is essential for big history output files (500 Million photon histories result in a 125MB output binary file), as it allows fast data handling by the IDL image reconstruction program

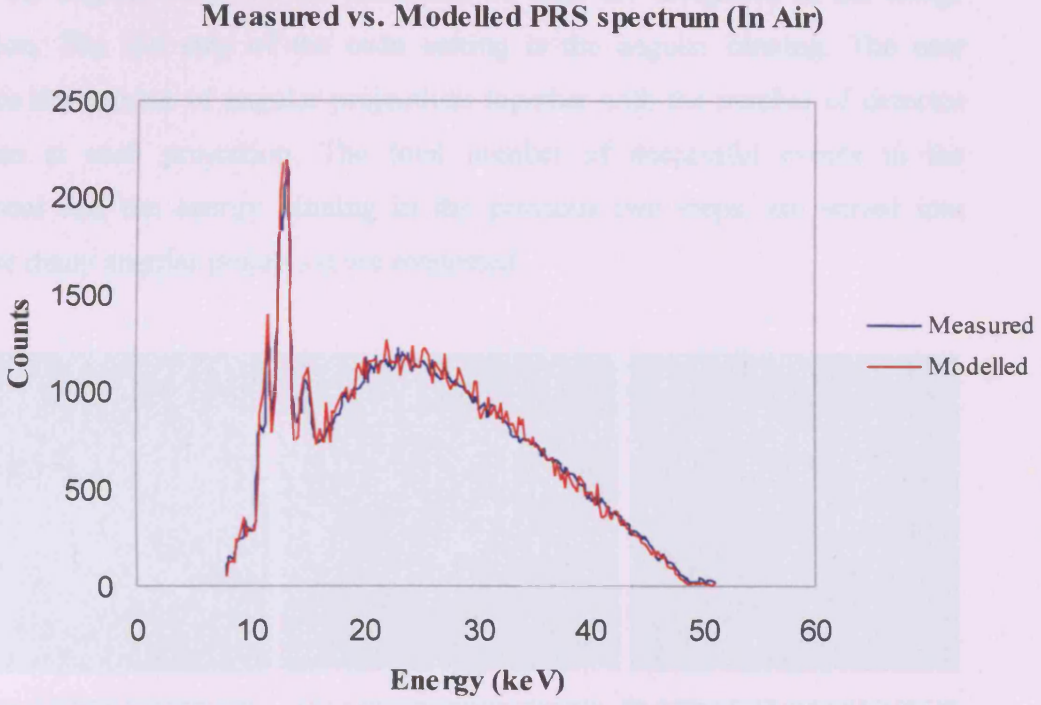

Figure 5.8 Comparison of the measured PRS spectrum in air (HPGe) and the spectrum generated by the MC model. The MC predicted spectrum is in good correlation with the HPGe measured spectrum.

5.2.2 Monte Carlo Image Reconstruction

An IDL code was constructed to "read in" the Monte Carlo output file (Erlandson 2004). The binary file is a long array of lines, each of which contain the seven output variables, and the code is requested to sort the data according to various scanning parameters replicating the experimental set-up. The code sorts every photon according to its energy, the binning of which is specified by the user. In this manner, a number of different energy resolving detection systems can be

simulated. The direction cosine values (U, V and W) then come in effect and are now sorted according to a pre-defined collimator acceptance angle. Values U and V govern the direction of the photon travel in the x and the y axes respectively just as the photon strikes or enters the Germanium region, while W values govern the azimuthal angle with respect to the z axis. The event scores with values of W within the angular range of the collimator at hand are integrated in the image formation. The last step of the code sorting is the angular binning. The user specifies the number of angular projections together with the number of detector positions at each projection. The total number of successful events in the directional and the energy binning in the previous two steps, are sorted into however many angular projection are requested.

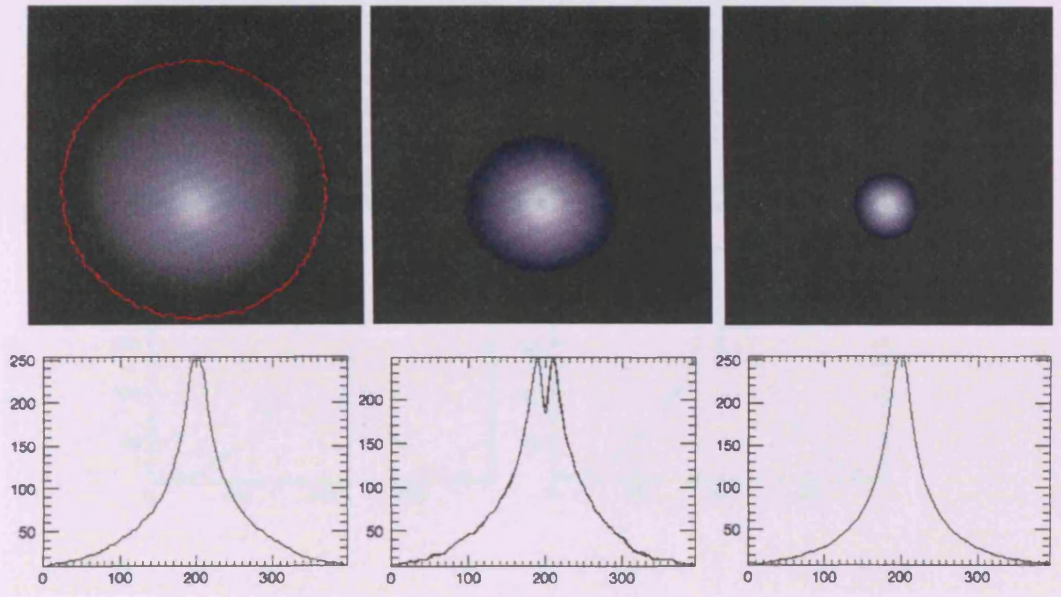

Figure 5.9 IDL reconstructed Monte Carlo images of the ^{241}Am source in the regular homogeneous phantom. Selective reconstruction was carried out yielding different images (total spectrum on the left, scatter only in the middle and photopeak only on the right). The profile drawn across the images (bottom row) indicates the FWHM of respective image.

The resulting spectra are then input into the reconstruction algorithm that was used for the experimental image reconstruction. Selective reconstruction in the case of the ^{241}Am source is again achieved by implementing various energy windows of interest. The resulting Monte Carlo modelled images of the ^{241}Am

mono-energetic source in the regular phantom are shown in Figure 5.9. The periphery of the phantom is again described from total spectral integration. Performing selective reconstruction demonstrates the *virtual source* image generation. The effect of the scatter energy window selection on the image is shown in Figure 5.10. The narrow scatter window provides superior image sharpness compared to the wider scatter window. This is expected as the narrower energy window includes photon events that have not undergone multiple orders of scattering, thus providing more localised geometrical information.

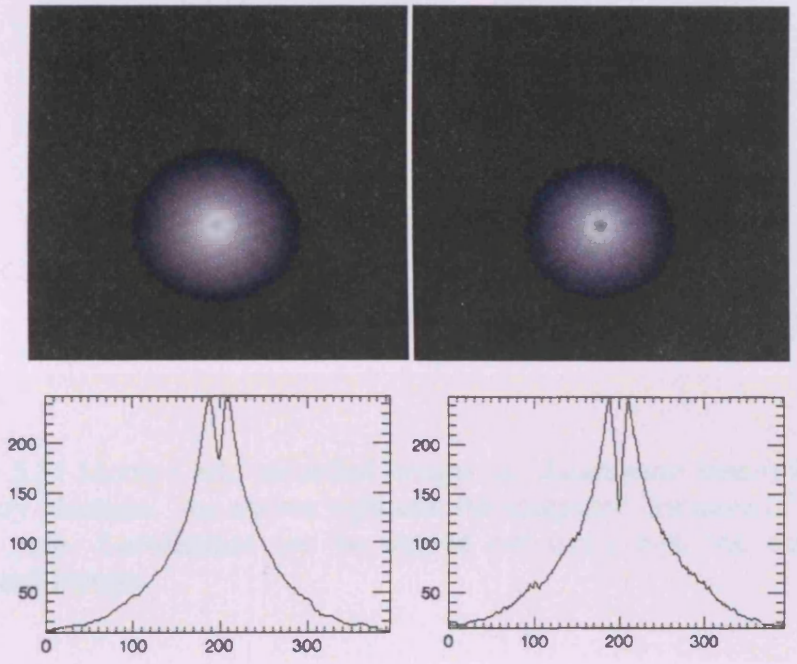

Figure 5.10 Monte Carlo generated *virtual source* images. Wide-10% scatter photon energy window from the photopeak (left) and narrow-5% (right) scatter energy window and their resulting image are illustrated. The respective profile drawn across each image is shown underneath. The narrow window (5%) provides better indication of the *virtual source* location.

As stated previously, the response of the Germanium detector (quantum efficiency, energy resolution electronic noise) was not incorporated into the theoretical model. Confirmation of the modelled geometry was carried out and geometrical registration of the source position performed, which will prove useful

in the later stages of the PECT Transform Map derivation. Precise knowledge of the source position can lead to accurate overlaying of the two images for accurate transformation. Statistical analysis on the theoretical images showed that the mean image intensity at the source position is directly proportional to the number of photon events employed by the model as shown in Figure 5.16.

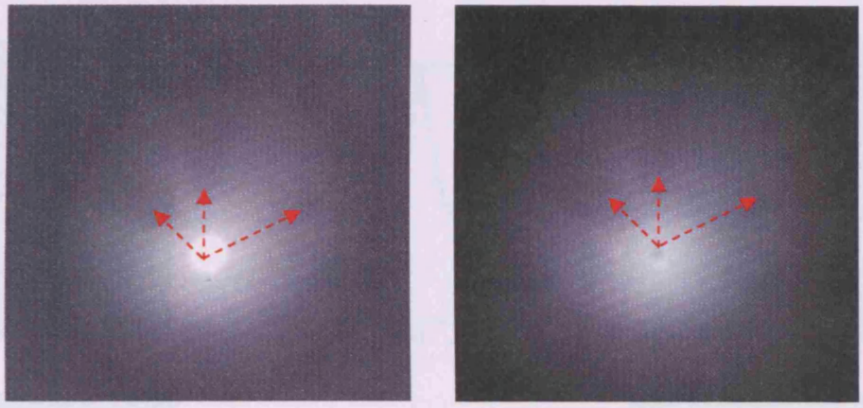

Figure 5.11 Monte Carlo modelled images of Aluminium inserts in the regular geometry phantom. The arrows represent the computed distances of the source to the Al rods. Localisation can be carried out using both the scatter and the photopeak images.

Landmark registration is also visible in the theoretical images. Figure 5.11 shows images of Aluminium inserts in the regular geometry phantom. Registration of the distances between the source position and the attenuator (Al rod) can be computed accurately. This again assists in the quantification of the image, as computation of the distance quoted in image pixel values can be accurately translated into geometrical units (mm). The reconstructed theoretical images were analysed and quantified in the same manner as the measured images. A direct comparison of measured and modelled images with the same geometrical set-up is presented in Figure 5.12. A profile is drawn across both modelled and measured images.

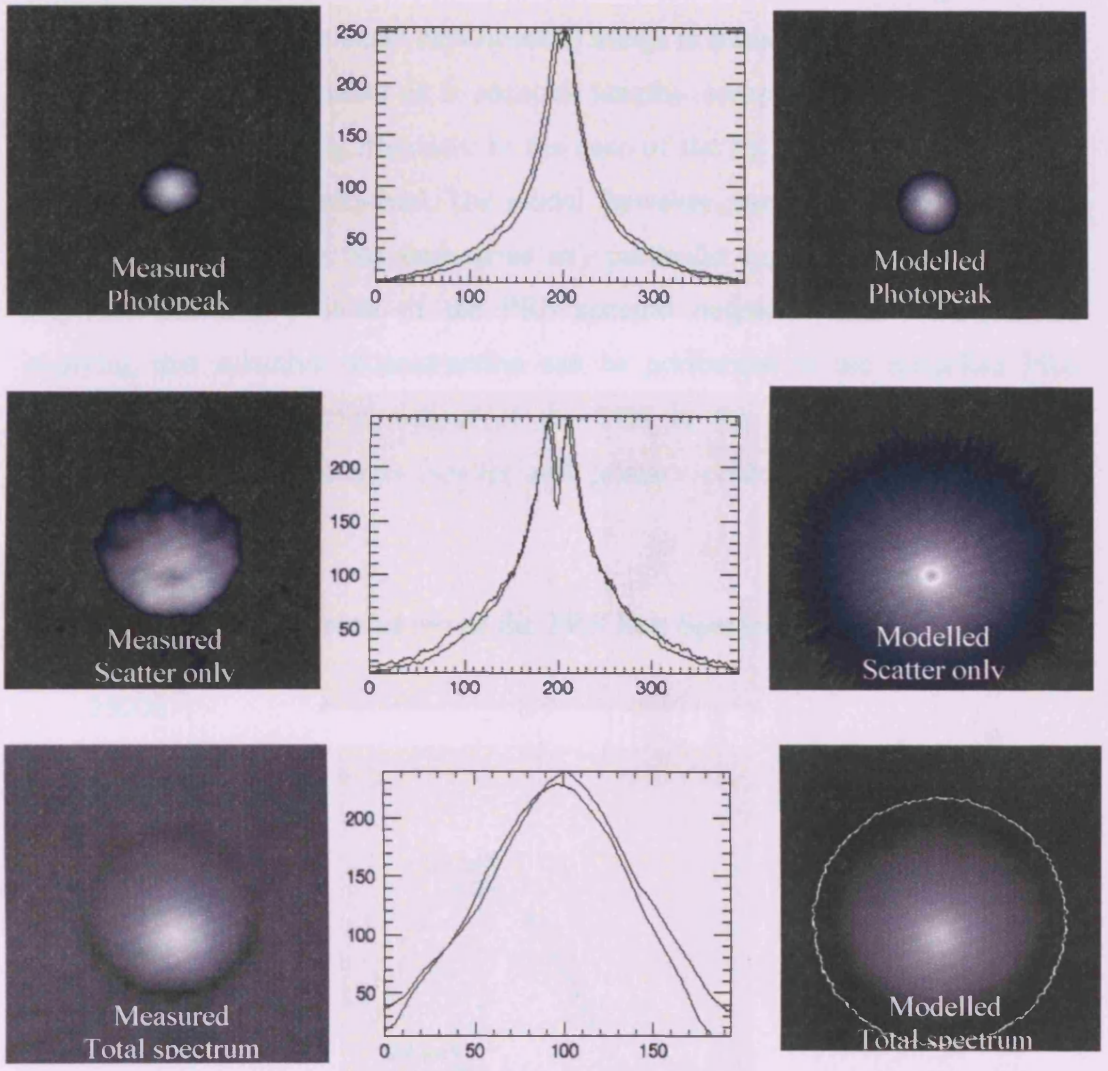

Figure 5.12 Comparison of measured (left) and modelled (right) ^{241}Am images in the heterogeneous phantom. Energy selective reconstructed images i.e. photopeak, scatter only and total spectral integration both experimentally measured and MC simulated are presented.

Each column of images in Figure 5.12 represents the measured image (top row) and the respective modelled image, for the same scanning conditions. The modelled images look very similar to the experimental images. The model replicated the realistic photon interactions within the phantom and produced the desired result in the reconstruction process. The scope of the modelling of the

experimental work was to reproduce the measured images so that they can be employed in the extraction of the dosimetric information that these images carry. To actually replicate the exact experimental image in terms of the photon counting statistics is a difficult task, as it requires lengthy computer runs and does not provide any potential significance. In the case of the PRS polychromatic source resolution is no longer required. The model, however, can be requested to flag up any photon history that has undergone any particular type of scattering. In this way, the scattered content of the PRS spectral output can be distinguished, implying that selective reconstruction can be performed in the modelled PRS images. The total spectral output of the PRS in the homogenous geometric phantom and its constituents (scatter and primary content) is shown in Figure 5.13.

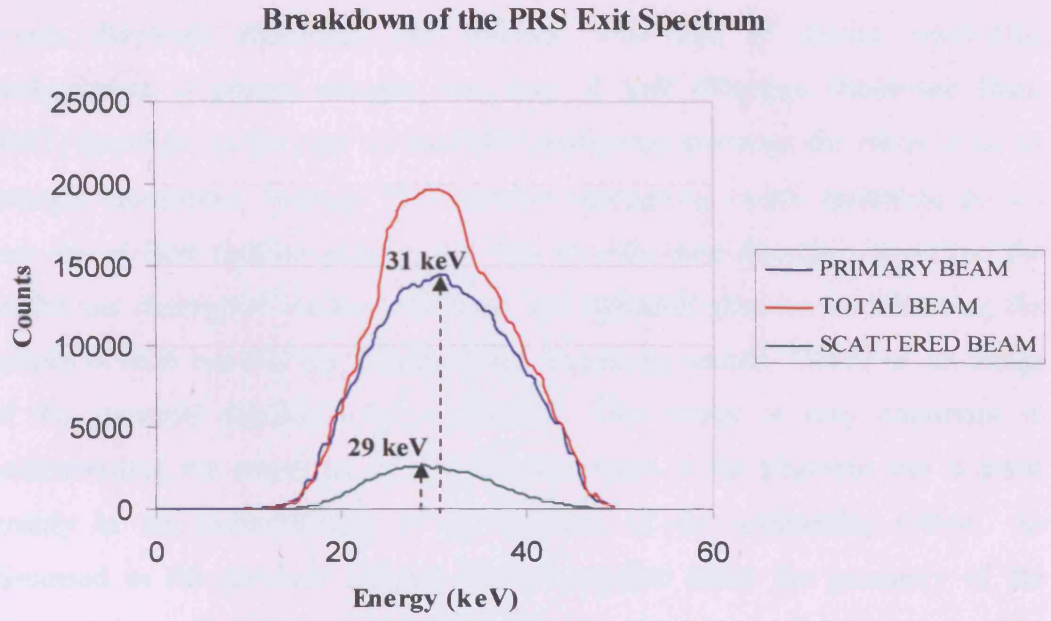

Figure 5.13 Segmentation of the total PRS spectrum into primary and scattered content using the MC model. The mean energy of the scattered radiation has dropped due to the interaction processes (Compton shift). The change, however, is small compared to the mean energy of the total PRS output. Selective reconstruction is unlikely therefore, to produce a change on the resulting PRS image as shown in Figure 4.21.

The vertical dotted lines on Figure 5.13 indicate the mean energy of the scattered and the primary photon beam. The shifting of the scattered beam towards lower photon energies (Compton Shift) is as expected very small (~2 keV). It must be

noted therefore, that photons undergoing inelastic scattering must still carry enough energy to escape the medium. Thus it can be concluded that such photons most probably undergo a single interaction in the medium. Such photons do not transfer much of their incident energy to the medium (Dose deposition) Figure 5.13 shows that most of the PRS photons that undergo interactions with the phantom material will most probably be stopped within the phantom and only a small fraction will escape the phantom. Dosimetric Monte Carlo simulations showed that almost 90% of the emitted intensity will be stopped in the medium. This implies that the total exit spectrum is mostly comprised of primary photons that escape the phantom without any interaction, together with photons that may have undergone elastic scattering with the atomic structure of the phantom material. Such photons therefore do not deposit any of their energy in the medium For the PRS study, the model was therefore requested to take the elastic scattering events (Rayleigh scattering) into account. This type of photon interaction predominates at photon energies less than 25 keV (Physical Reference Data, NIST) therefore, in the case of the PRS continuous spectrum the effect must be strongly considered. Primary PRS photons undergoing elastic scattering do not lose any of their incident energy, but they do alter their direction. However, the model can distinguish between primary and scattered photons by following the history of each one and can indicate when scattering occurs. Therefore, an image of the scattered photons only is possible. This image is very important in understanding the scattering events that take place in the phantom and it assist greatly in the understanding of the function of the collimating system. As discussed in the previous chapter, the information about the geometry of the phantom is carried over to the image by the scattered radiation events. The collimator acceptance angle is responsible for the projected FOV of the detector onto the phantom, and thus governs the amount of radiation that is detected. Increasing the collimator angle allows more scattered radiation to be integrated in the resulting image, thus increasing the amount of geometrical information in the image, as demonstrated in Figure 5.14. The content of geometrical information therefore increases with increasing collimator angle. It must be noted again, however, that a wide-angle collimator is in practice difficult to implement as the

high photon flux will give rise to an unacceptable detector dead time. Direct comparison, in terms of the counting statistics of the measured and the theoretical images was again not possible as the high PRS flux requires prolonged computation times. This problem can be overcome by scaling the modelled images to the measured ones. This is achieved by analysing both sets of images for statistical variance (Signal to Noise ratio, SNR).

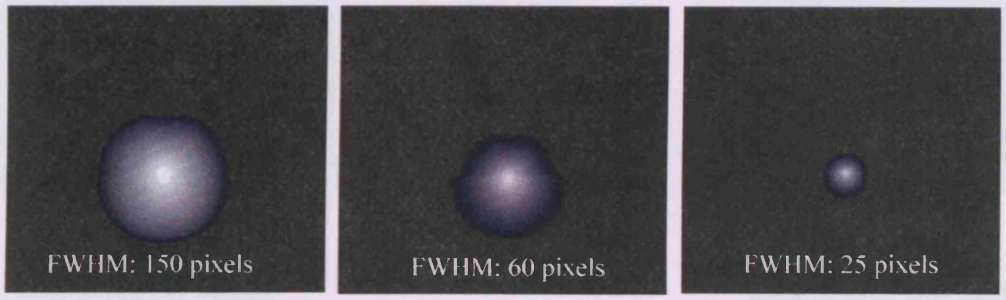

Figure 5.14 Images of the PRS in the homogeneous phantom as a function of increasing collimator acceptance angle (4°, 8° and 12°).

The collimator acceptance angle for the images in Figure 5.14 decreases from left to right. The geometrical information regarding the topology of the phantom is lost when a high collimator system is employed as stated previously. Therefore landmark registration will not be possible. The special requirements of the collimator system required in the derivation of the PECT Transform Map will be assessed later in this chapter. The modelled PRS images for the regular shape phantom compare well to the measured ones. The measured images of the PRS source when inserted in the homogeneous and the heterogeneous phantom and their respective modelled images are shown in Figure 5.15. The Monte Carlo model employed for the simulation provided realistic data on the interactions of the photons in the phantom. The data generated was correctly processed by the reconstruction algorithm and produced comparable and reproducible images. Modelled images of both the ^{241}Am and the PRS sources were generated for different numbers of photon histories. Source localization was also performed and the coordinates recorded for each image. The intensity values of each image were

also assessed and their respective maxima and minima recorded. The relationship of the resulting image intensity values to the number of photon histories employed to produce that image is shown in Figure 5.16.

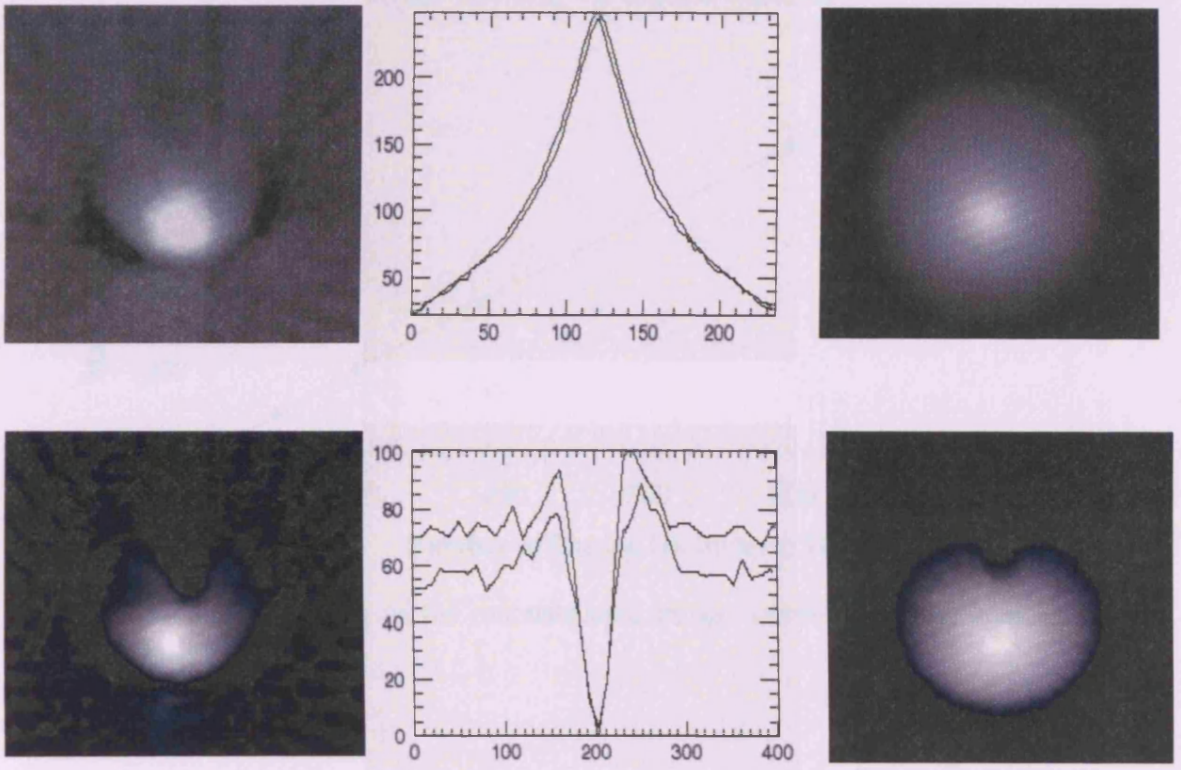

Figure 5.15 Comparison of measured (left) and modelled (right) PRS images in the regular geometry phantom for different tissue constituents. (Homogeneous phantom on the top, heterogeneous phantom on the bottom). Profiles are drawn across the respective images. In the case of the heterogeneous phantom the profile is drawn across the Aluminium rod plane.

The intensity of the measured images was far greater than that of the modelled images. Correlation, therefore, of the modelled to the measured images was not directly applicable. As stated previously, for the modelled images, the ratio of the maximum point of intensity to the minimum was investigated and compared to the measured images. In addition, visual inspection of the modelled images allowed confirmation of the correct simulation of the physical interactions that take place

which give rise to the resulting images. Finally, the reconstruction algorithm employed for the modelled image formation provided comparable results.

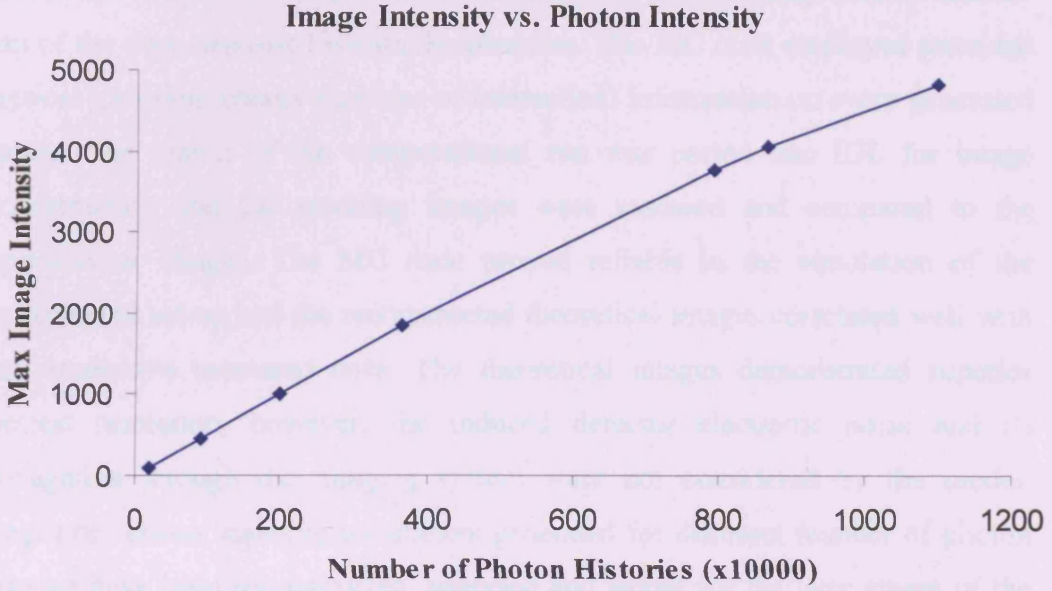

Figure 5.16 Relationship of the reconstructed image intensity against number of photon histories.

The filter that was employed for this analysis was a low-pass cosine filter; in this way any low frequency data will be omitted so that the intensity of each image can be carefully assessed. The relation of the image intensity to the flux of the photons detected is linear for low intensity images, but tails off as the number of photon histories is vastly increased. This relationship can determine the role of the image values and their dependence on the PECT Transform map. Understanding of the generation of the resulting image values is of vital importance if accurate extraction of dosimetric information from the image is to be undertaken.

5.2.3 Summary

The task undertaken in the modelling of the experimental set-up was necessary in the attempt to derive an empirical relationship between the image formed and the map of the dose deposited within the phantom. The MC code employed provided physical (position, energy and type of interaction) information on every generated photon. The output of the computational run was ported into IDL for image reconstruction and the resulting images were assessed and compared to the experimental images. The MC code proved reliable in the simulation of the experimental set-up and the reconstructed theoretical images correlated well with their respective measured ones. The theoretical images demonstrated superior contrast resolution, however, the induced detector electronic noise and its propagation through the imaging system were not considered by the model. Images of various scanning parameters generated for different number of photon histories have been reconstructed, analysed and stored for the later stages of the PECT Transform Map derivation. The effect of the photon flux upon the resulting intensity of the reconstructed image was also assessed. This is also an important parameter that needs to be carefully considered in the derivation of a transform map. Finally, the source position in the image was determined for all images so that superposition of images can be carried out based on that position.

Monte Carlo Dosimetric Studies

5.3 Geometry and Scoring of the Dosimetry Model

The photon interactions taking place in the regular geometry phantom and the image created from photons that escape the phantom have been considered. For the correct translation of this image into a dose distribution map, the distribution of the photons that contribute to the radiation dose deposited during clinical treatment has to be determined. The dosimetric simulation therefore, needs to compute the dose deposition of the PRS photons in the phantom. Absorbed dose is the quantity of interest in radiation dosimetry and is defined as the energy retained in the medium. ICRU (Report 33) has defined this quantity to be:

$$\text{Absorbed Dose (D)} = \frac{dE_{abs}}{dm}\left[\frac{energy}{mass}\right] \qquad \text{(ICRU 1980)}$$

Where dE_{abs} is the mean energy imparted by the ionising radiation to a mass, dm, of matter given in units of Gray (1 Gy = 1 J/Kg). Energy is transferred from the incident photon to the electron (*Kerma*: Kinetic energy released in the Medium) but not all of it is retained in the medium; part of it is radiated away as bremsstrahlung radiation produced from collisions of electrons with atomic nuclei in the medium. Thus kerma and absorbed dose do not take place at the same location due to the length of the induced electron tracks.

A BEAMnrc code was constructed and adapted accordingly to carry out this task. (Seco 2004) The geometry and materials inserted into this code simulated the regular geometry phantom (Nylon 6/6, PMMA). The scoring of the results is different in this case, as accurate energy deposition of the photons interacting within the phantom is required. The Monte Carlo model follows the history of each primary photon (and its consequent by-products) and thus scores the total energy deposited in a specified region. The cylindrical geometry and the composition of the phantom are identical to the previous Monte Carlo code. The

phantom, however, is now segmented into small cubes, or volume elements (voxels), so that energy deposition can be computed accurately, but most importantly, so that it can be localised precisely (~mm). In this way, the fall-off of the radiation with respect to the distance from the source can be determined (Depth Dose curve) and more importantly, the distribution of the dose around the tip of the PRS can be derived. The accuracy of the predicted results was then compared to measured data. The optimisation of the model, and hence its accuracy to produce realistic results, was first tested against measured data in water. The segmentation, or voxelisation of the phantom was performed in the x, y and z planes of the phantom, as shown in Figure 5.17. The z-axis represents the depth of the phantom. At z =0, the centre of the phantom is defined and this is where the source was inserted. There are four voxels defining planes crossing the z-axis. The top and bottom cylinders (shaded in grey in Figure 5.17) are each of 5.9 cm in height The middle two cylinders are each of 1mm in height and are smaller volumes so that dose can be computed to a greater accuracy in these areas. The dark cylinder at the top of the phantom denotes the PRS drift tube. With this in mind, the X-Y plane profile can be computed at z = 0, i.e. where the source lies, or at z = -5.9, 1mm from the tip of the probe. The segmentation of the phantom perpendicular to the horizontal X and Y plane was uniform. The voxels formed were made of 1mm at each side. At Z=0, at the source level, the size of the resulting elemental volume of the voxel was 1 mm^3. The generation of photons was again based on an accumulative probability curve that randomly generated photon energies. The mean energy deposition for the number of photon histories generated per unit voxel was computed by the model and quoted in terms of Gy/particle/voxel. The scoring of the results was extracted as a .3ddose format file which contained the complete set of data for every single voxel in all three planes. The X-Y plane at Z=0 is the slice of interest if the resulting dose map is to be compared to the measured data in the water tank.

The user can access and manipulate the generated data using DOSXYZnrc GUI (DOSXYZnrc Users Manual 2002). The generation and voxelisation of the phantom can also be inspected (dosxyz_show). Once the computation of the dose deposition within the phantom is completed the user can then inspect the resulting

dose map at every Z-axis plane. The desired plane can be sliced and the data extracted as a 2-dimensional array in text format (ASCII). This file contains the values of the energy deposition in each voxel in both the X and the Y planes. This file can then be ported into IDL, where it can be read in and processed. The resulting distribution of the dose intensity about the tip of the probe (i.e. at x = 0, y = 0, z = 0) can then be presented as an image whose intensity is directly proportional to the deposited dose.

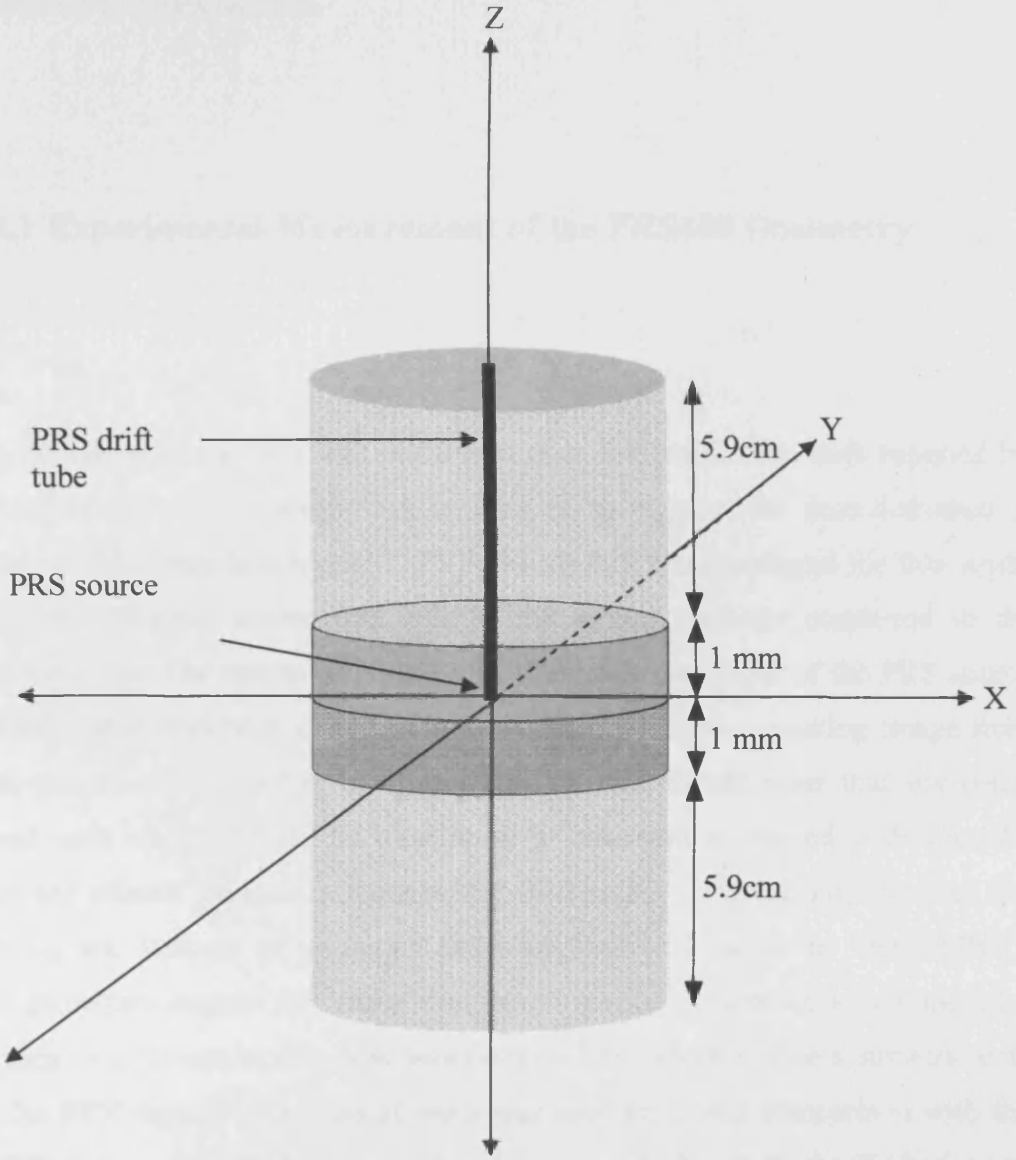

Figure 5.17 Diagram of the segmentation of the phantom (voxelisation) along the Z-axis (in cm). The phantom is segmented in 4 regions. The two larger regions lie between z = 0.1 to z = 6.0 and similarly z =-0.1 to z = -6.0. Two smaller regions exist between z = 0 and z = 1.0 and similarly, z = 0 and z = -1.0. In the X-Y plane voxels are generated every 1 mm step. This will eventually segment the whole phantom into small volume elements where dose is scored.

The resulting image can then be cross calibrated against the image formed by the photon flux escaping the phantom and thus the PECT Transform Map can be derived. The optimisation of the model is therefore an important step ensuring accurate generation of the dose map at the source plane and consequently, in the correct dose map image creation. In all dosimetric models, Rayleigh scattering was switched on and incorporated in the tracking of photon events. The theoretical depth dose of the PRS in water was consequently generated and compared to measured data.

5.3.1 Experimental Measurement of the PRS400 Dosimetry

The dosimetry of the PRS was performed on a dedicated water tank supplied by the manufacturer. This water tank is designed to measure the dose delivered in water, as discussed in Chapter 1. PRS350 s/n 005 was employed for this work, while the PRS400 source (s/n 198) is the source currently employed in the TARGIT trial. The results in Figure 5.18 show that the output of the PRS source is comparable with both x-ray heads (to within 2%), so the resulting image from both sources is expected to be almost identical and should mean that any result found with s/n 005 could be transferred to information derived with s/n 198. Standard clinical procedure requires the PRS to be systematically checked for stability and isotropy of its output and straightness of the probe. The TARGIT trial guidelines suggest that probe straightness test be carried out before and after the treatment to ensure that dose was delivered as expected. The dosimetric data for the PRS recorded for clinical work was used for direct comparison with the modelled data. The PRS water tank is permanently based at the Radiotherapy Physics Dept, Middlesex Hospital, and is still in clinical use for the TARGIT trial.

PRS350 s/n: 005

radius (mm)	Dose Rate (Gy/min)
5.0	12.294
5.5	9.984
6.0	8.171
6.5	6.797
7.0	5.710
7.5	4.858
8.0	4.164
8.5	3.611
9.0	3.157
9.5	2.793
10.0	2.474
10.5	2.195
11.0	1.975
11.5	1.781
12.0	1.614
12.5	1.467
13.0	1.342
13.5	1.228
14.0	1.127
14.5	1.043
15.0	0.957
15.5	0.887
16.0	0.825
16.5	0.770
17.0	0.713
17.5	0.668
18.0	0.627
18.5	0.588
19.0	0.552
19.5	0.523
20.0	0.489

PRS400 s/n: 198

Dose Rate (Gy/min)
12.061
9.811
8.037
6.680
5.623
4.776
4.109
3.567
3.124
2.749
2.441
2.181
1.962
1.769
1.606
1.460
1.335
1.217
1.122
1.034
0.961
0.892
0.831
0.776
0.723
0.676
0.631
0.590
0.556
0.526
0.496

Figure 5.18 Depth Dose measurements for different PRS sources. The output of both sources is comparable (to within 2%). PRS350 (used in this project) and PRS400 (now clinically used) both yield comparable dose rates.

The Monte Carlo model employed for the dose computation of the PRS in the regular geometry phantom did not incorporate the function of the Ionisation

Chamber. The modelling of the PRS probe photon generator (drift tube and its metallic constituents) and its resulting dose have already been carried out by other groups (Ebert and Carruthers 2003, Yanch and Harte 1996) and therefore this was not undertaken in this work. The photon output of the PRS as recorded on HPGe detector was inserted in the code, as discussed previously. The resulting modelled depth dose curve of the PRS in water and its correlation to measured data is shown in Figure 5.19. The predicted depth dose was normalised for maximum dose rate at 10mm from the tip of the probe.

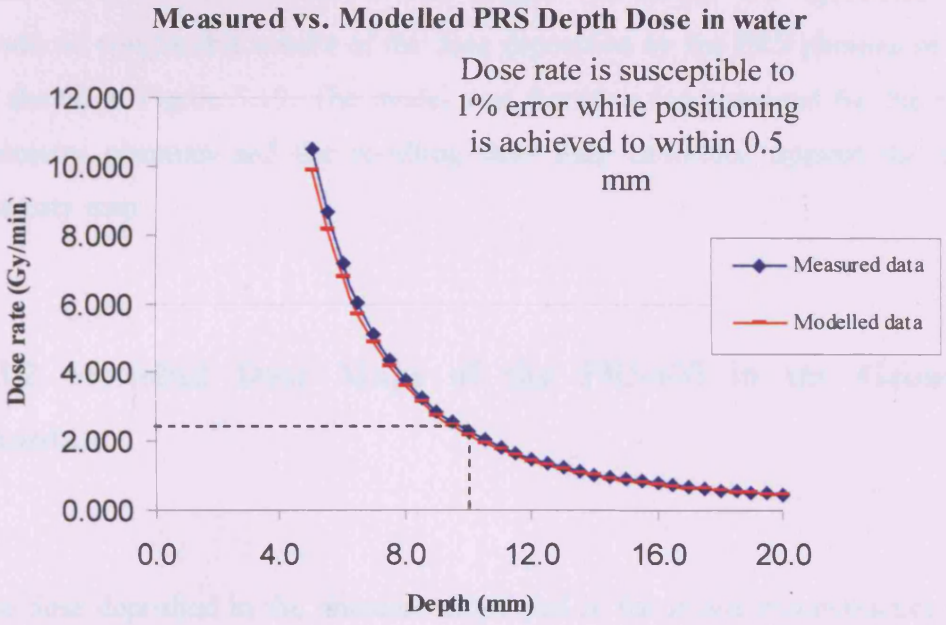

Figure 5.19 Graph demonstrating correlation between modelled and experimentally measured data. The modelled data was normalised for a maximum dose rate at 10 mm from the tip of the source, i.e. at a dose rate of approximately 2.5Gy/min.

The model and the measured depth curves match closely within errors at distances greater than 10 mm from the tip of the probe. The reason for the discrepancy at distances closer to the source is due to the difficulty in obtaining reliable experimental measurements of dose at such high dose gradients. As stated previously, the model did not simulate the function of the Ionisation Chamber employed in the experimental dosimetry, hence the difference in dose rate values at distances close to the tip of the probe. The PRS depth dose curve, as predicted and measured, indicates that dose deposition is minimal at distances greater than

30 mm from the tip of the probe. The model can be used to estimate the dose at distances greater than the capability of the water tank (max distance 20mm from either side of the probe). The segmentation of the resulting dose map image must therefore take this into consideration in the derivation of the PECT Transform Map. The deposition of dose at large distances from the probe is minimal and the low energy deposition values may induce noise in the transformation process. Because of this, the region of dosimetric interest for the computation of the transform map is a circle of radius 20mm about the source location and this region must be extracted from the overall image. The model was optimised and it produced comparable results of the dose deposition by the PRS photons in water, as shown in Figure 5.19. The model was therefore implemented for the regular geometry phantom and the resulting dose map calibrated against the photon intensity map.

5.3.2 Modelled Dose Maps of the PRS400 in the Geometric Phantom

The dose deposited in the phantom employed in the image reconstruction phase was modelled. The generated dose map can be inspected by the user using the DOSXYZnrc GUI. The localised dose map of the PRS can clearly be seen in Figure 5.20; it appears as a blue dot in the phantom. Focusing on the spot, the isodose curves of the distribution of photons about the tip of the probe can be identified. The almost spherical distribution of the PRS photon output results in a near-spherical dose distribution in the phantom. The rapid dose fall-off that occurs is due to the low-energy nature of the beam and results in a much localised dose deposition. The high intensity output of the PRS implies that a high flux of low keV photons is produced, hence yielding high dose rates. The system therefore, delivers a near isotropic distribution of high intensity, low energy x-rays that can be delivered directly to the tumour site or tumour cavity.

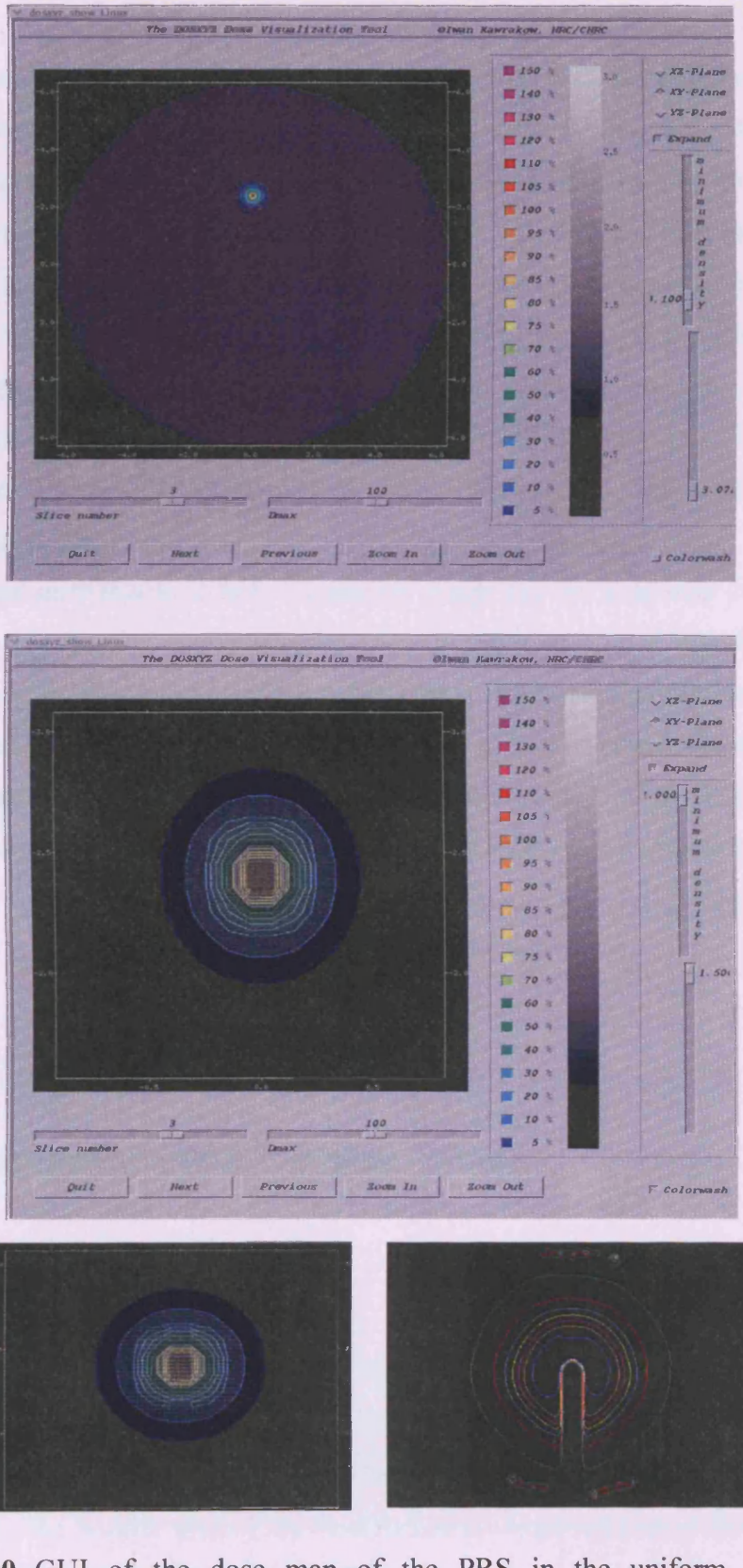

Figure 5.20 GUI of the dose map of the PRS in the uniform geometry homogeneous phantom. The macroscopic view of the source in the phantom is shown on the top. Focusing on the source (microscopic view) on the bottom, the spherical dose deposition of the PRS is compared to the previously measured contoured dose map as predicted by radiochromic film. (Figure 1.11, Chapter 1).

The localised region of PRS dose deposition was also investigated on the heterogeneous phantom, so to check that the presence of the Aluminium rods would contribute to perturbing effects in the deposition of dose. The dose map of the PRS in the heterogeneous phantom is shown in Figure 5.21. The enlarged dose map at the bottom of the schematic confirms that the localised nature of the dose deposition is not influenced by the presence of inhomogenities at distal regions from the tip of the probe. Investigating the effect of bone interfaces at various distances and the possible implication in dose delivered to bone (e.g., in the ribs for the case of breast IORT) has already been carried out by other groups (Ebert and Carruthers 2003).

The spherical distribution of both the photon image and the dose map encourages an attempt to compare one against the other in order to form a transform map. This map is a mathematical function or kernel that can be employed to convert the emission image acquired during a treatment into a 2 dimensional distribution of the dose delivered during irradiation of the patient. Careful manipulation of the corresponding images, the extraction of the useful information of each image and the overlaying of one on top of the other is required. The predicted dose map is ported in IDL, as stated previously and its image formed.

5.3.3 Derivation of a PECT Transform Map

The resulting image of the dose map deposited by the PRS in the regular geometry phantom is shown in Figure 5.22. The map is also presented as a surface plot, demonstrating the sharp fall-off of the PRS dose. The intense region of this image is essentially the breadth of the PRS dose delivered. Segmentation of this image to extract the information of the region of interest was performed in IDL.

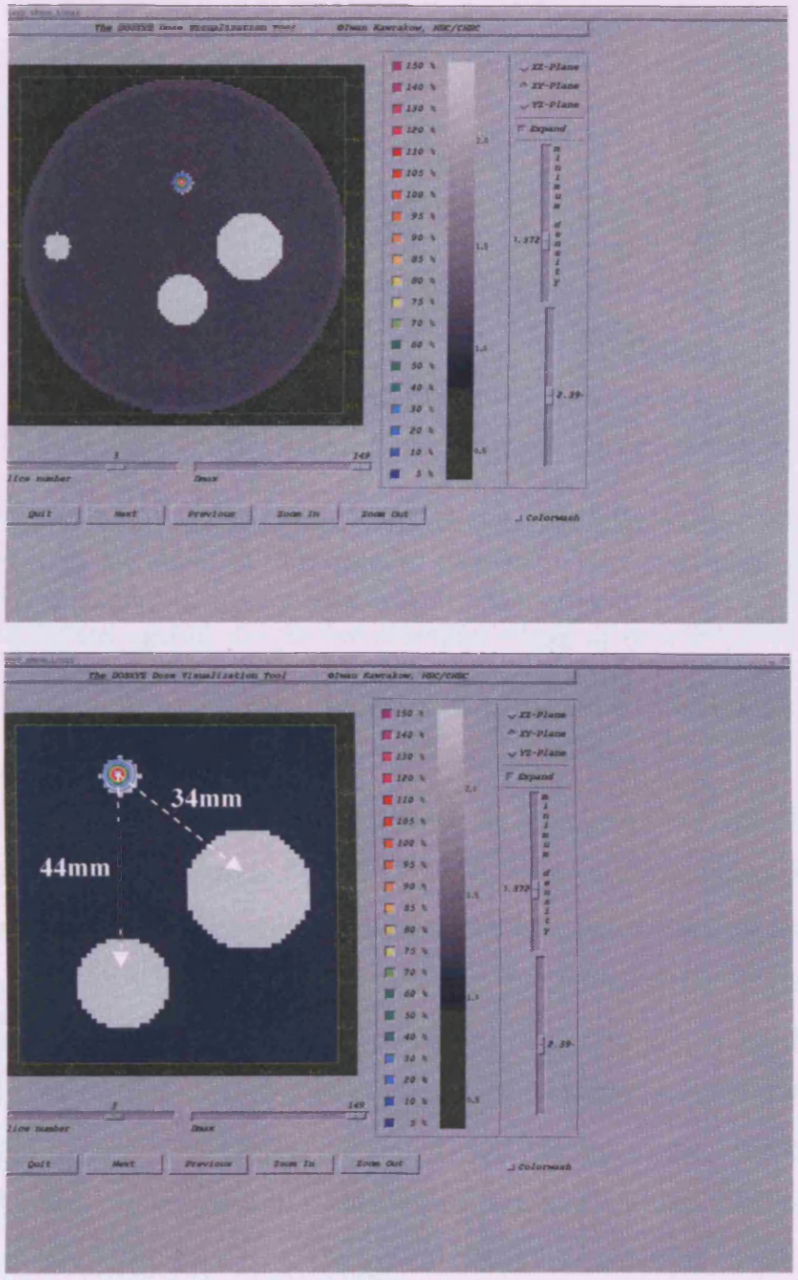

Figure 5.21 GUI of the dose map of the PRS in the heterogeneous phantom. The white circles denote the Aluminium rods inserted to simulate bone. The localised dose map is not affected (perturbed) by the presence of in heterogeneities at the given distances from the PRS probe.

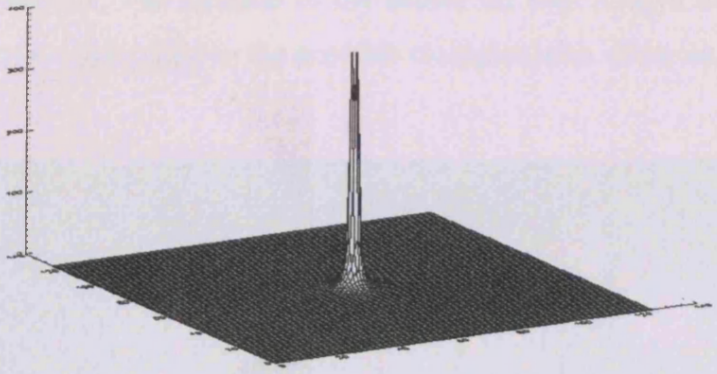

Figure 5.22 IDL generated image representing the distribution of dose values (dose map) of the PRS in the regular phantom. The generated dose map is presented as a surface plot. The spherical distribution of the dose delivered can be directly calibrated against the photon emission image as reconstructed by IDL and predicted by the model.

Segmentation of the images is performed in IDL (*exrtrac*) and the two new images extracted, as shown in Figure 5.23. The reconstructed emission images are also created in IDL so direct calibration of the two corresponding images can be undertaken in the IDL program. This enables the computation of the Transform Map to be processed under same conditions since both images are Monte Carlo generated. The direct correlation of stored images is not so trivial to implement and can induce errors, as in the process of the storage of the resulted image the measured image table can be significantly altered. Since IDL provides this advantage to manipulate any image through a specified code it can be implemented to compute the PECT Transform Map directly from raw data, and not already manipulated data. Extraction of data from both images can be performed accurately once the region of interest is specified and the image dimensions computed in terms of pixel numbers. The derivation of the transform map can therefore be achieved by simple calibration of the extracted region of interest of the emission image against the dose image.

The transformation of one image to the other is simply given by the division of one by the other, pixel by pixel, once the images are carefully aligned. This is

achieved using knowledge of the source location in terms of pixels in both the x and the y directions. The location of the source on both images is the common point of reference and assists in the accurate co-registration of the images.

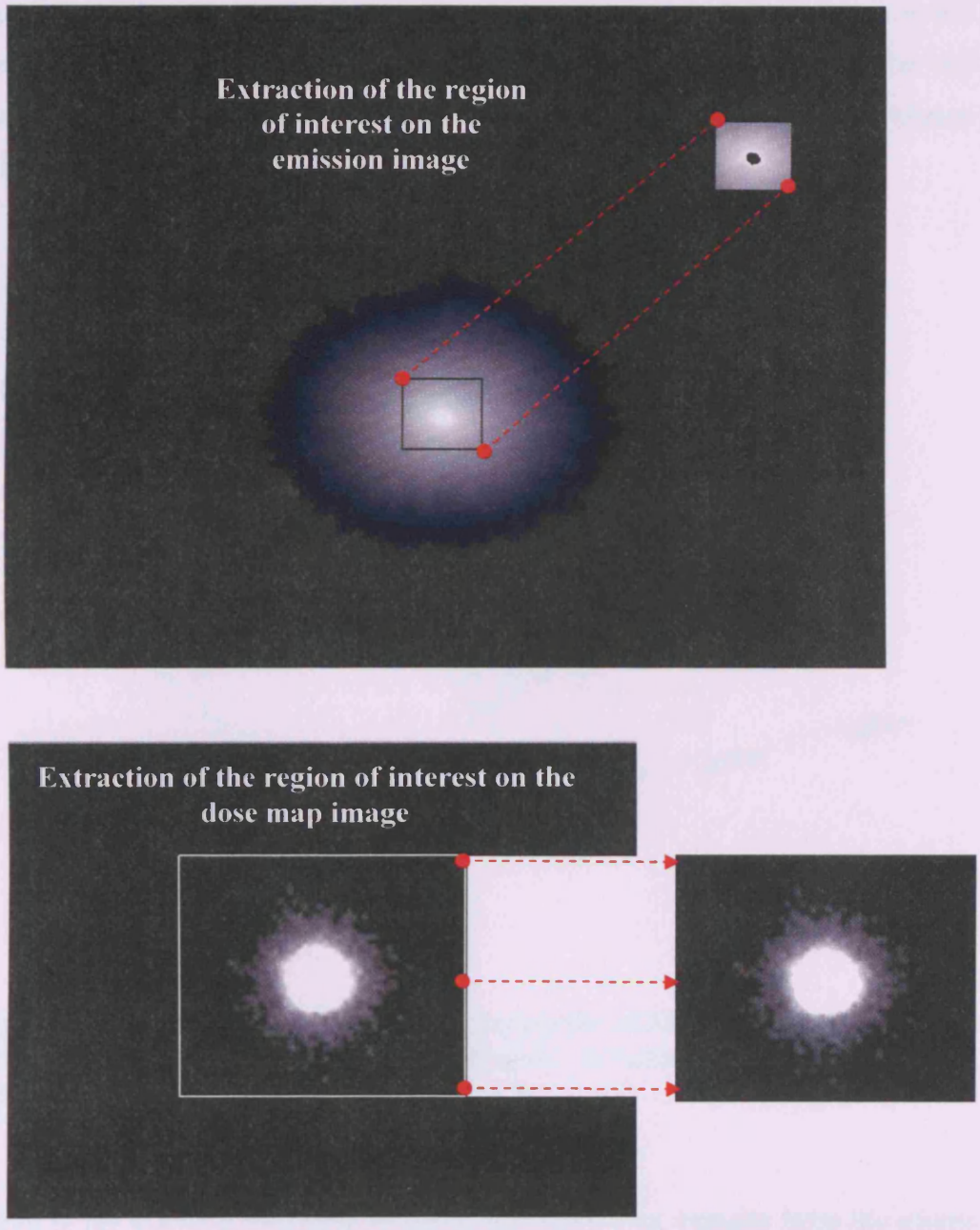

Figure 5.23 Extraction of regions of interests of similar dimensions (30mm x 30 mm) for both the emission image (top) and the dose map image (bottom). The extracted regions are superimposed and calibrated against each other, yielding the PECT Transform Map (images not to scale).

Landmark registration can be also implemented for more accurate orientation of the emission image. The result of the calibration of the two images yields the PECT Transform Map. This function is pictorially presented in Figure 5.24; this is an IDL GUI (*iimage v 6.0*) that allows inspection of the function in all dimensions. The top shaded area represents a surface plot of the function in a 2 dimensional array. The size of the function array is equal to the size of the two images (400 x 400) and represents the region of interest around the source chosen (30 x 30 mm)

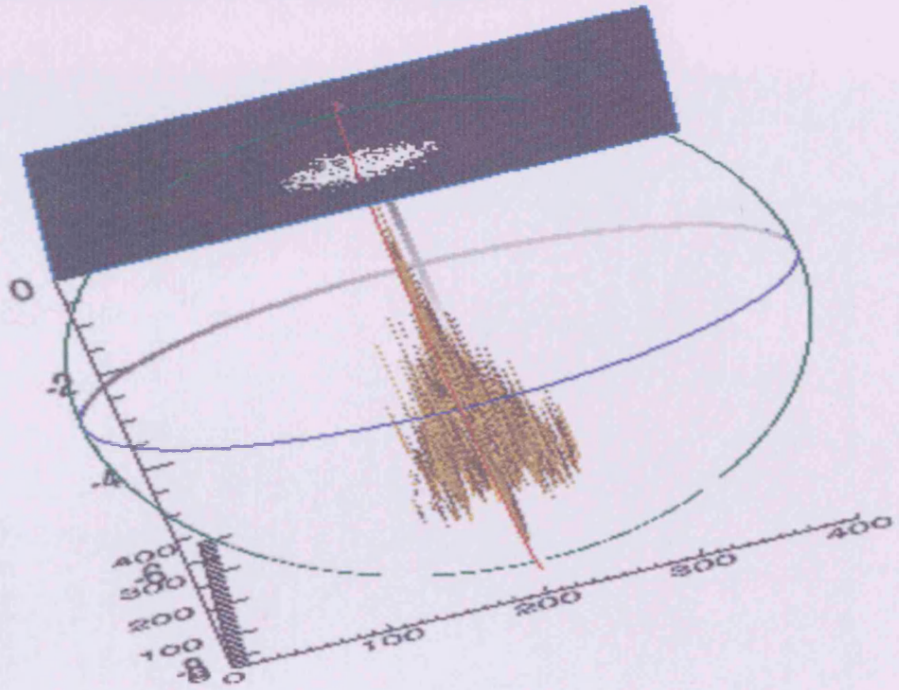

Figure 5.24 3-Dimensional Graphical presentation of the PECT Transform Map (*i-image* IDL). Units of this mathematical relation are CT (Hounsfield) number*Gy^{-1}.

Depth in the x-axis is measured in pixels and represents distance from the source for the dimensions of the region of interest chosen. The negative scale is not indicative and varies according to the intensities of both the emission image and the dose map. This scale is strongly dependent on the way in which the IDL software normalises the resulting transform map during the cross-calibration of

the respective image intensities. At the source position, the magnitude of the mathematical function reaches a maximum and it tails off as distance increases. This is as expected, as dose deposition is greater nearer the source, whilst the intensity of the emission image also reaches its maximum at the source position thus resulting in a higher value in the transformation process. Similarly, as distance increases the dose rate decreases, as does the intensity of the emitted source, thus the tailing of the transform map either side of the source position. A 2-dimensional presentation of the Transform Map at the plane just over (1 voxel thickness) the source level is shown in Figure 5.25.

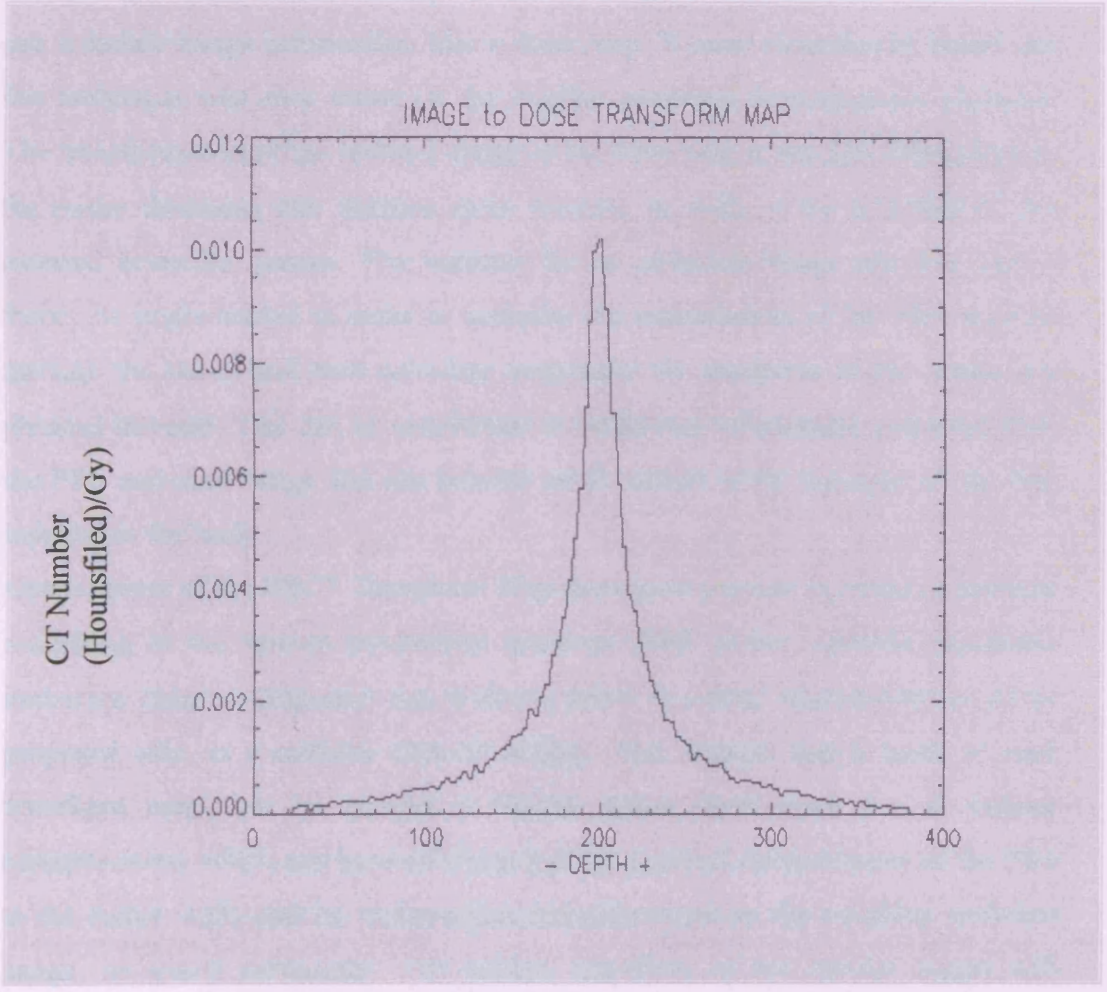

Figure 5.25 2-Dimensional PECT Transform Map (at 1 voxel over the source level) of the PRS source in the regular phantom. The data was extracted for a 25mm square region of interest about the source location and related to an emission image with the same ROI dimensions

5.4 Discussion

The results of the dosimetric studies on the PRS proved to be reliable in the simulation of the physical interactions that lead to transference of energy from the emitted photons to the surrounding materials. The MC predicted PRS depth dose in water matched very closely the water tank measured PRS depth doses (see Figure 5.19). The computed dose deposition was calibrated against the modelled emission photon map, giving rise to the PECT Transform Map derivation. This was the first experimental attempt to derive accurate computational kernels that can translate image information into a dose map. It must therefore be noted that this technique was only tested on the regular geometry homogeneous phantom. The transformation of the emitted image to the dose map is strongly dependent on the tissue thickness that photons must traverse in order to be recorded by the external detection system. The variance in the emission image intensity can in theory be implemented in order to compute the transmission of the PRS photons through the tissue and thus calculate accurately the thickness of the tissue that photons traverse. This can be considered as additional information extracted from the PRS emission image and can provide confirmation of the topology of the PRS inserted in the body.

Optimisation of the PECT Transform Map derivation process in terms of accurate modelling of the various parameters involved (PRS source, realistic phantoms, ionisation chamber response) can in theory allow for actual implementation of the proposed idea in a realistic clinical setting. This implies that a bank of such transform maps can be created at various tissue thicknesses (i.e. at various transmissions) which can be confirmed by both physical measurement of the PRS to the tissue walls and by transmission measurements on the resulting emission image, as stated previously. The choice, therefore, of the correct kernel will depend on the tissue thickness (i.e. the depth of insertion of the PRS in the body).

Furthermore, the image to dose transform map can assist in predicting the dose deposited in regions distal to the PRS probe, especially in regions where

important anatomical structures lie (e.g., the ophthalmic cavity in the case of the brain).

Provided an emission image is produced in relatively short time (e.g. within first 5 minutes of the actual treatment, nominally lasting for about 30 minutes) and that it can be processed and translated into a dose map on line with the imaging system, the deposition of dose in the patient can be monitored and recorded in real-time. The dose map derived from the emitted image allows for documentation of the PRS treatment delivery, implying that radiation oncologists and surgeons may be able to fully assess the radiation treatment and therefore provide the patient with documented proof of the dose prescription delivered. Currently, the TARGIT trial protocol does not provide documented verification of the treatment delivery (with the exception of the TLD protocol employed checking the dose delivered to the skin surface). The PRS control console stores the treatment record (Internal Rate Monitor count rate) and allows checks on the stability of the dose rate of the system. This record, together with the TLDs read out postoperatively, is at present the only means of in-vivo dosimetry checks on the PRS system. The scope of this project, i.e. the derivation of the PECT Transform map, can therefore improve on the current state of the TARGIT in-vivo dosimetry protocol and provide physicians with a comprehensive assessment of the radiotherapy delivered during the PRS treatments.

CHAPTER 6

Conclusions and Future Directions

6.1 Conclusions

This research project had two main goals:

- Source localisation of a point x-ray source embedded in tissue from images of its own radiation field. (For both mono- and poly-energetic x-ray sources.)
- Verification of the dose distribution predicted from the resulting image using Monte Carlo modelling.

The scope of this work was to attempt to image a point source of x-radiation by devising an external detection system. Both mono-energetic (^{241}Am) and poly-energetic sources (PRS) were considered. The detection system comprised of a well collimated HPGe detector used in a rotate-translate Portal Emission Computed Tomography (PECT) modality setting. A regular geometry phantom made of tissue equivalent materials (TE) and a realistic anthropomorphic phantom were constructed to simulate the patient.

In the case of the mono-energetic source, selective reconstruction was possible due to the superior energy resolution of the Germanium detector. This allowed for different regimes of the collected spectra to be integrated for image reconstruction (i.e. primary photons only, scattered photons only and total spectral integration). The scatter only image gave rise to the *virtual source* image as the photopeak was purposely omitted. This provided the best means of source localisation, as the black spot created by the photopeak emission depicted the source position with increased accuracy (to within 1 mm). The idea of energy selective reconstruction is only possible on the mono-

energetic source, as stated previously. This technique could be ideal for image verification in HDR brachytherapy (BT). An energy resolving detection system will provide the *virtual source*, image allowing accurate source localisation of the brachytherapy sources. In the case of a single source insertion the problem is easily handled, however in nominal brachytherapy treatments, an array of such sources is inserted into the body, making the detection problem more complex. This problem could be overcome by making the collimation system specification more stringent, allowing it to focus on each source independently as it scans the whole radioactive seed array. This technique for real time image verification of the inserted sources could easily be implemented in the existing treatment planning system (TPS) software widely available in modern brachytherapy (e.g. PLATO) instead of the source positions determined by radiographic localisation. The TPS software stores the radial dose distribution of the source, thus once the source positions are inserted the overall dose map produced by the seeds can be extracted.

In the case of the poly-energetic source (PRS), the need for energy resolving detectors in not apparent. Distinction of the primary to secondary radiation is not possible, thus selective reconstruction is not applicable. Monte Carlo studies employed showed that even in the breakdown of the continuous PRS spectrum, energy selective reconstruction does not produce different effects.

Source localisation was achieved to within 3mm on the PRS source. This was based on 36 angular views distributed around 360 degrees with 20 detector positions at each view. As the diameter of the PRS probe is 3.2mm, this result suggests that localisation accuracy needs to be improved. This could be achieved by increasing the statistical sample of the acquired data by increasing the number of angular projections. To compensate for minimal scanning movement in the clinical setting, it is proposed that a ring of detectors centred at the axis of the inserted probe be designed. As the imaging system does not require energy resolving detectors for the imaging of the PRS, cheaper, easier to construct, detection materials should be considered. This could be achieved using scintillating crystals coupled to optical photon detector (PMTs, CCD).

The second aim of this work was to obtain important dosimetric information directly from the image formed by the escaped photons. In the case of the PRS, this theory could be implemented as the system deposits the biggest proportion of the emitted photons (>85%) very locally (i.e. in a spherical cloud about the tip of the probe). The image formed from the escaped photons describes this localised intensity of predominantly primary photons about the tip of the probe. Monte Carlo studies were employed to:

- reproduce the emitted images
- compute the PRS dose distribution (in order to)
- relate the emission map directly to the dose map.

The latter task (i.e. the transformation of the emitted image to the dose distribution) was carried out in IDL. This enabled the accurate superposition of the two intensities so that the relation, or cross calibration, of one to the other can take place. Results showed this technique to be viable as both sets of data (image and dose intensity) are much localised. The localised energy deposition of the PRS (see Figure 1.10) is due to the low energy of the photons produced (50kVp), which are absorbed with radial distance from the tip of the probe(sharp dose fall-off). The emitted PRS image is mostly comprised of primary photons (>80%) emanating from the source, thus giving rise to the localised emission map. These two intensity distributions can therefore be calibrated against each other giving rise to the PECT transform map. The dose map comprised of the absorbed photons within the medium, while the emitted image comprised of the predominantly primary photons that escaped the medium. This can therefore be seen as an inverse relation as primary photons do not contribute to energy deposition while absorbed photons do not contribute to the image formation. This was the ultimate goal of this research project and results showed that it can be accomplished with the PRS within the constraints of the PECT imaging system. Having tested, therefore, the efficacy of this technique in the laboratory, the future task that lies ahead is to transform the idea into a fully functional clinical system.

6.2 Future Directions

As stated previously, the PECT imaging system employed to image the PRS source buried in the body needs to be modified for clinical use in future PRS treatments. Various issues need to be carefully addressed for this to happen; the most important being the special sterilisation requirements during PRS treatments. As the PRS system is essentially a radio-surgical tool, the sterile conditions under which the system operates need to be carefully observed. In nominal TARGIT treatments, the PRS is rendered sterile by draping the system with appropriate material. Similar conditions must therefore be applied to the clinical PECT system for safe use in the operating theatres. This implies that the ring of detectors proposed earlier needs also to be rendered sterile so that it can come into close contact with the patient. Furthermore, special consideration must be given to the ergonomics of the detection system; in terms of powering the system up, its read-out electronics and the time required to assembly the whole PECT system.

With regards to optimisation of the PECT detector system and the PECT transform map, accurate modelling of the structure of the tip of the PRS and of the applicators employed in IORT is required. The effect of applicators on the isotropy of the PRS, together with the scattering events occurring in the image formation, need to be carefully addressed. The scattering of emitted photons within the structure of the applicators might be beneficial in imaging the PRS source using the PECT imaging system. The scattering effects may be picked up by the detection system, resulting in a description of the surface of the applicators. This is seen as quite an advantage as the applicators themselves can act as the markers required to register the source in the image with respect to known landmarks. This will greatly assist in the localisation of the PRS source as the distance of the edge of the applicator to the tip of the probe is fixed and invariable.

Finally, the PECT transform map can be computed for different depths of PRS insertion in tissue. The resulting image will strongly depend on the thickness of tissue

the PRS beam needs to traverse for photons to escape. Transmission measurements can therefore be carried out on the emission image to compute the actual tissue thickness that PRS photons traverse. The PECT transform map can be utilised further in order to extract crucial information on the dose delivered to structures distal to the PRS source.

Realistic phantoms (based on human tissue) can therefore be employed to compute the corresponding transform map required for accurate correlation of the image to the dose map. Moreover, inhomogeneous interfaces in the tissue, such as tissue/bone and tissue/air interfaces, need to be carefully considered in order to predict dose perturbations present in such interfaces. This can greatly assist in predicting the dose delivered to the rib bones (thorax) , and in the case of the left breast, assess the risk of radiation reaching the cardiac muscle (myocardium) lying underneath.

A library of transform maps can be created so that the user can apply the correct map to the specified tissue thickness. This library will be available for on-line dose verification during PRS treatments. The efficacy therefore of this technique lies with the speed at which the image can formed and thus related to the dose map for real time monitoring of the PRS treatment delivery. As stated on many occasions in this thesis, since an in-vivo dosimetry protocol is not available for the TARGIT trials to-date, real-time dose verification in a relatively short time (compared to the total PRS treatment duration) allows for user intervention, whilst providing clinicians with a comprehensive assessment of the radiotherapy treatment to be stored with the patient records.

Finally it is hoped that this technique can assist greatly in increasing the confidence of the safe usage of the PRS source in the interstitial radiotherapy treatment of malignant tumours.

Appendix

Error propagation analysis:

Let the derived quantity be u=u (x, y, z...)

Then the standard deviation of quantity u is given by:

$$\sigma^2{}_u = \left(\frac{\partial u}{\partial x}\right)^2 \sigma_x{}^2 + \left(\frac{\partial u}{\partial y}\right)^2 \sigma_y{}^2 + \left(\frac{\partial u}{\partial z}\right)^2 \sigma_z{}^2 + \ldots$$

This is generally known as the error propagation formula and is applicable to almost all situations in nuclear measurements (Knoll G. F. 1989).

In this case, $u= (x^2+y^2)^{1/2}$,

thus, $$\frac{\partial u}{\partial x} = \frac{1}{2}\left(x^2 + y^2\right)^{-1/2}(2x) = \frac{x}{\sqrt{x^2 + y^2}},$$

similarly, $$\frac{\partial u}{\partial y} = \frac{y}{\sqrt{x^2 + y^2}}.$$

Inserting these values into the empirical formula gives,

$$\sigma^2{}_u = \frac{x^2}{x^2 + y^2}\sigma_x{}^2 + \frac{y^2}{x^2 + y^2}\sigma_y{}^2.$$

REFERENCES

AAPM 1987 Specification of brachytherapy source strength: report of AAPM Task Group No. 32 *AAPM report 21* (New York: AIP)

AAPM 1991 Clinical implementation of AAPM Task Group 32 recommendations on brachytherapy source strength specification Med. Phys. **18** pp 439-448

AAPM 1993 Remote afterloading technology: report of AAPM Task Group 41 *AAPM report 41* (New York: AIP)

AAPM 1995 Dosimetry of interstitial brachytherapy sources: recommendations of the AAPM radiation therapy committee Task Group No. 43 Med. Phys. **22** pp 209-234

AAPM 1997 Code of Practice for brachytherapy physics: report of the AAPM radiation therapy committee Task Group No. 56 Med. Phys, **24** (10) pp 1557-1597

AAPM 1998 High dose-rate brachytherapy delivery: report of the AAPM radiation therapy committee Task Group No. 59 Med. Phys. **25** (4) pp 375-403

Anger H O, 1958 Scintillation Camera Rev. Sci. Instr. **29** pp 27-33

Aird E G and Williams J R 1993 "Brachytherapy" In *Radiotherapy Physics* Williams J R and Thwaites D I eds. (Oxford: Oxford University Press) pp 185-226

Anderson L L 1995 "Dose specification and quantification of implant quality" In *Brachyterapy Physics* Williamson J F, Thomadsen B R and Nath R eds. (Madison: Medical Physics Publishing) pp 343-360

Anderson L L and Presser J E 1995 "Classical systems I for temporary interstitial implants: Manchester and Quimby systems" In *Brachytherapy Physics* Williamson J F, Thomadsen B R and Nath R eds. (Madison: Medical Physics Publishing) pp 301-321

Baum M, Vaidya J.S, Mittra I 1997 Multicentricity and recurrence of breast cancer. Lancet **349**, 208

Bagheri-Sheikh D, Munro P, 1998 A Monte Carlo study of verification imaging in high dose rate brachytherapy Med. Phys. **25** (4) pp 404-414

Ballester F, Puchades V, Lluch J L, Serrano M A,-Andrés A, Limami A 2001 Technical note: Monte-Carlo dosimetry of the HDR 12i and Plus ^{192}Ir sources, Phys. Med **28** pp 2586-2591

Ballester F, Granero D, Pérez-Calatayud J, Casal E, 2004, Monte Carlo dosimetric study of Best Industries and Alpha Omega Ir-192 brachytherapy seeds, Med. Phys. **31** pp 3298-3305

Beatty J., Biggs P.J., Gall K., Okunieff P., Pardo F.S., Harte K.J., Dalterio M.J., Sliski A. P 1996., "A new miniature x-ray source for interstitial radiosurgery: Dosimetry". Med. Phys. **23** (1), pp 53-62,

Bell A.G. 1903, "The uses of Radium". Am. Med. **6**, 261

Biggs D. S., Thomson E.S. 1996, "Radiation Properties of a miniature x-ray device for radiosurgery". The British Journal of Radiology, **69**, pp 544-547

Blondel C, Noll D, Maeght J, Celler A, 2002 Comparison of different figure of merit functions for dynamic single photon emission computed tomography (dSPECT) IEEE Trans Nucl Science **49** (3) pp 761-767

Boone J M, Seibert J A, 1988 Monte Carlo simulation of the scattered radiation distribution in diagnostic radiology Med. Phys. **15** pp 713-720

Bruyant P B, 2002 Analytic and Iterative reconstruction algorithms in SPECT J Nucl. Med. **43** pp 1343-1358

Chambron J, Arntz Y, Eclancher B, Scheiber C, Siffert P, Hage-Hali M, Regal R, Kazandjian A, Prat V, Thomas S, 2000 A pixellated gamma camera based on CdTe detectors, clinical interests and performances Nucl Instrum. Meth. **A380** pp 474-478

Cosgrove R.G., Hochberg F.H., Zervas N.T., Pardo F.S., Valenzuela R.F., Chapman P. 1997 Interstitial irradiation of brain tumours, using a miniature radiosurgery device: Initial Experience. Neurosurgery, **40** (3) pp 518-525

Cumberlin R L and Coleman C N 2002 New directions in brachytherapy Int. J. Radiation Oncology Biol. Phys. **53** (1) 6-11

Das R K, Li Z, Perera H, Williamson J F, 1996 Accuracy of Monte Carlo photon transport simulation in characterizing brachytherapy dosimeter energy-response artefacts Phys. Med. Biol. **41** pp 995-1006

Deehan C 2000 "Brachytherapy into the new century" In *Physics and Engineering in Medicine in the New Millennium* Sharp P F and Perkins A C eds. (York: IPEM Publishing)

Dinsmore M., Harte K.J., Sliski A.P., Smith D.O., Nomicos P.M., Dalterio M.J., Boom A.J., Leonard W.F., Ottinger P.E., Yanch J.C. 1996 A new miniature x-ray source for interstitial radiosurgery: Device Description. Med. Phys. **23** (1), pp 45-52

Duan J, Macey D J, Pareek P N, Brezovich I A, 2001 Real-time monitoring and verification of in vivo high dose rate brachytherapy using a pinhole camera Med. Phys. **28** (2) pp 167-173

Ebert M A, Carruthers B, Lanzon P J, Haworth A, Clarke J, Caswell N M, Siddique S A 2002 Dosimetry of a low-kV intra-operative X-ray source using basic analytical beam models Australasian Physical & Engineering Sciences in Medicine **25** pp 119-123

Ebert M A, Carruthers B, 2003 Dosimetric characteristics of a low kV intra-operative x-ray source: Implications for use in a clinical trial for treatment of low-risk breast cancer Med. Phys. **30** (9) pp 2424-2431

Eisen Y, Shor A, Mardor I, CdTe and CdZnTe, 2004 X-ray and gamma ray detectors for imaging systems IEEE Trans Nucl. Science **51** (3) pp 11911-198

Erlandson 2004, personal communication

Ford R L, Nelson W R 1978 The EGS code system: computer programs for the Monte Carlo simulation of electromagnetic cascade showers (Version 3) *SLAC Report 210* (Stanford: SLAC)

Fragoso M, 2004 Application of Monte Carlo techniques for the calculation of accurate brachytherapy dose distributions PhD Thesis, University Of London

Fragoso M, Seco J, Nahum A and Verhaegen F 2003 Incorporation of a combinational geometry package and improved scoring capabilities in the EGSnrc Monte Carlo code system Med. Phys. **30** 1076-1085

Fragoso M, Verhaegen F, Nahum A 2002, A Monte Carlo comparison (EGSnrc PENELOPE) and commercial treatment planning system (PLATO) calculations of the dose distribution delivered by low dose-rate ^{137}Cs sources in intracavitary brachytherapy Med. Phys. 29 1350

Fung A Y C, 2002, C-arm imaging for brachytherapy source reconstruction: geometrical accuracy Med. Phys. **29** (5) pp724-726

Gall K., Beatty J., Biggs P., Butler W., Sliski A.P. 1993, "Novel Microdensitometer for radiochromic film characterisation of a new 40kV x-ray device used for stereotactic radiation therapy". Med. Phys. **20** (3), 925

Gilland D. R, Tsui BMW, McCartney W H, Perry J R, Berg J 1988 Determination of the optimum filter function for SPECT imaging J Nucl. Med. **29** pp 643-650

Gilland D R , Jaszczak R J, Riauka T A, Coleman R E, 1997 Approximate 3D iterative reconstruction for SPECT Med. Phys. **24** (9) pp 14211429

Glasgow G P 1998 "Isodose planning: brachytherapy" In *Treatment Planning in radiation Oncology* Khan F M and Pottish R A eds. (Baltimore: Williams & Wilkins) pp 243-280

Gruner S M, Tate M W, Eikenberry E F 2002 Charge-coupled device area x-ray detectors (Review Article) Rev. Sci. Instrum. **73** (8) pp2815-2842

Hubbell J H 1999 Review of photon interaction cross section data in the medical and biological context (Review) Phys. Med. Biol. **44** R1-R22

Hudson H M, Larkin R S, 1994 Accelerated image reconstruction using ordered subset of projection data IEE Trans Med. Imaging **13** pp601-604

ICRU 1980 Radiation Quantities and Units ICRU *Report 33* (Maryland ICRU)

ICRU 1985 Dose and Volume specification for reporting intracavitary therapy in gynecology *ICRU Report 38* (Maryland: ICRU)

ICRU 1989 Tissue substitutes in radiation dosimetry and measurement. *ICRU Report 44* (Maryland ICRU)

ICRU 1997 Dose and Volume specification for reporting interstitial therapy *ICRU Report 58* (Maryland: ICRU)

ICWG 1990 Interstitial brachytherapy: physical, biological and clinical considerations Anderson L L, Nath R, and Weaver K A eds. (New York: Raven)

Johns H.E., Cunningham J.R 1984 "The Physics of Radiology", Fourth Edition, (Thomas, Springfield, IL, USA) pp 174

Joslin C.A.F., Flynn A., Hall E.J.1999, (Ed: Arnold), "Principles and practice of brachytherapy using afterloading systems" pp 52-57

Karger C P, Hipp P, Henze M, Echner G, Hoess A, Schad L, Hartmann G H, 2003 Stereotactic imaging for radiotherapy: accuracy of CT, MRI, PET and SPECT Phys. Med. Biol. **48** pp 211-221

Kawrakow I, Rogers D W O 2000, The EGSnrc System, a Status Report. Proceedings of the Monte Carlo 2000 Conference, Lisbon

Khan F M 1994 The physics of radiation therapy 2nd Ed (Baltimore: Williams & Wilkins)

Khare H S, DiBella E V R, Kardmas D J, Christian P E, Gullberg G T, 2001 Comparison of static and dynamic cardiac perfusion thallium-201 SPECT, IEEE Trans. Nucl. Science **48** pp 774-779

Knoll G.F 1989 "Radiation detection and measurement" Second Edition (Wiley and Sons)

Laub W, Alber M, Birkner M, Nusslin F, 2000 Monte Carlo dose computation for IMRT optimization Phys. Med. Biol. **45** pp 1741-1754

Lerma F.A., Williamson J.F 2002 Accurate localisation of intracavitary brachytherapy applicators from 3D CT imaging studies, Med. Phys. **29** (3) pp 325-333

Li S, Frassica D, DeWeese T, Lee DJ, Geng J, Nag S, 2003, A real-time image-guided intraoperative high-dose-rate brachytherapy system Brachytherapy **2** (1) pp 5-16

Li Z, Nalcacioglu I A, Ranka S, Sahni S K, Palta J R, Tome W, Kim S, 2001 An algorithm for automatic, computed tomography based source localisation after prostate implant, Med. Phys **28 (7)** pp 1410-1415

Liu L, Bassano D A, Prasad S C, Keshler B L, Hahn S S, 2003 On the use of C-arm fluoroscopy for treatment planning in HDR brachytherapy Med. Phys. 30 (9) pp 2297-2302

MAESTRO®-32 MCA Emulator for MS Win98 and MS WinNT, Software User's Manual, Perkin Elmer, EG&G Ortec, TN, USA

Matsumoto K, Ohnishi H, Yokoi T, Niida H, Nishimura Y, Wada Y, Kida T, 2003 A multicenter evaluation of seven commercial ML-EM algorithms for SPECT Image reconstruction using simulation data Jpn J. Radiol. Technol **50** (4) pp 487-493

Mainegra-Hing E, Kawrakow I, Rogers D W O, 2003 Calculation for parallel plate ion chamber in ^{60}Co beams using the EGSnrc Monte Carlo code Med. Phys. **30** pp 179-189

Mainprize J G, Ford N L, Yin S, Gordon E E, Hamilton W J, Tumer T O, Yaffe M J, 2002 A CdZnTe slot scanner detector for digital mammography Med. Phys. **29** (12) pp 2767-2773

Medich D C, Munro J J, 2003 Monte Carlo calculated TG-43 dosimetry parameters for the SeedLink™ ^{125}Iodine brachytherapy system Med. Phys **30** (9) pp 2503-2508

Meier D, Czermak A, Jalocha P, 2002 Silicon detector for a Compton camera in nuclear medical imaging IEEE Trans. Nucl. Science **49** (3): 812-816

Meikle S R, Hutton B F, 1994 Accelerated EM reconstruction in total body PET: potential for improving tumor detectability Phys. Med. Biol. **39** pp 1689-1704

Meli J.A 1995 "Source Localisation in Brachytherapy Physics" Williamson J.F., Thomasden B.R., Nath R., eds. (Madison: Medical Physics Publishing) pp 235-251

Metaxas M G, Speller R D, Royle G J, Seco J, 2004 Source Location and Dose Verification for X-ray Intra-Operative Radiotherapy (IORT) Proceeding of the Medical Imaging Conference (MIC-M5-234), IEEE Rome 2004.

Mestais C, Baffert N, Bonnefoy J P, Chapuis A, Koenig A, Monnet O, Ouvrier-Buffet P, Rostaing J P, Sauvage F, Verger L 2001 A new design for high resolution, high efficiency CZT gamma camera detector Nucl Instrum. Meth. **A458** pp 62-67

Muehllehner G, Hamisch Y, 1999 Sodium iodide positron detectors: PET/SPECT dedicated systems, Revue de l'Acomen **5** (2) pp 145-150

Nakano T, Suchowerska N, Bilek M M, McKenzie D R, Ng N, Kron T, 2003 High dose-rate brachytherapy source localization: positional resolution using a diamond detector, Phys. Med. Biol. **48** pp 2133-2146

Nakano T, Suchowerska N, McKenzie D R, Bilek M M, 2005 Real-time verification of HDR brachytherapy source location: implementation of detector redundancy Phys. Med. Biol. **50** pp 319-327

Natterer F, 1986 The Mathematics of Computerized Tomography John Wiley and Sons and B G Teubner

Natterer F, 1999 Numerical Methods in Tomography Acta Numerica pp 1-35

Ogawa K, Ohno S, 2003 Three-Dimensional data acquisition with a semiconductor detector in SPECT IEEE Trans Nucl. Science **50** (1) pp 97-104

Ollinger J M, 1990 Iterative Reconstruction-Reprojection and the Expectation-Maximization algorithm IEEE Trans. Med. Imaging **9** pp 94-98

Pohle R, Wegner M, Rink K, Toennies K, Celler A, Blinder S, 2004 Segmentation of the left ventricle in 4d-dSPECT data using free form deformation of super quadrics Proceedings of SPIE (5370) pp 1388-1394

PeC, North Billerica, MA, USA "PRS400 – Theory of Operation Manual

Pérez-Calatayud J, Granero D, E. Casal E, and F. Ballester F 2005 Monte Carlo and experimental derivation of TG43 dosimetric parameters for CSM-type Cs-137 sources, Med. Phys. **32** pp 28-36

Polgar C, Sulyok Z, Fodor J, 2002 Sole brachytherapy of the tumour bed after conservative surgery for T1 breast cancer: five year results of phase I-II study and initial findings of a randomised phase III trial J. Surg. Oncol. **80** pp 121-128

Picardi L, Rosinvalle C, Tata A, Vignati A, 2000 The Italian IORT project Proceedings of the EPAC 2000, Vienna, Austria

Rivard M J, 2002 Comprehensive Monte Carlo calculations of AAPM Task Group Report No. 43 dosimetry parameters for the Model 3500 I-Plant 125I brachytherapy source Appl. Radiat. Isot. **57** pp 381-389

Seco J, 2004 personal communication

Shepp L A, Vardi Y, 1982 Maximum likelihood reconstruction in position emission tomography IEEE Trans Med. Imaging **MI-I (1)** pp 113-122

Singh M, Brechner R R, 1990 Compton camera J. Nucl Med. **31** pp 178-186

Speller R D, Horrocks J A, 1991 Photon scattering-a "new" source of information in medicine and biology? Phys Med. Biol. **36** (1) pp1-6

Takahashi Y, Ito A,Yoshioka a, Kuwabara A, Yanashita T, 2003 Verification of dose accuracy of RTP systems by Monte Carlo simulation, Proceedings of the EGS4 user's meeting (Japan) pp 74-81

Takayama T, Hiwatari K, Nakamura N, Motomura N, Mori I, Ohno R, 2000 Feasibility study of SPECT quantification using CdTe semiconductor detector Jpn J. Nucl. Med. **37** (4) pp 333-338

Todd-Pokropek A, 2003 Personal Communication

Todor D A, Zaider M, Cohen G N, Worman M F, Zelefsky M J, 2003 Intraoperative dynamic dosimetry for prostate implants Phys. Med. Biol. **48** pp 1153-1171

Vaidya J.S., Baum M, Tobias J.S., D'Souza D.P., Naidu S.V., Morgan S., Metaxas M.G., Harte K.J., Sliski A.P., Thomson E.S. 2001 Targeted intra-operative radiotherapy (TARGIT): An innovative method for treatment of early breast cancer" Annals of Oncology **12**, pp 1075-1080

Vaidya J S, Tobias J S, Baum M, Keshtgar M, Joseph D, Wenz F, Houghton J, Saunders C, Corica T, D'Souza D, Sainsbury R, Massarut S, Taylor I, Hilaris B, 2004 Intraoperative radiotherapy for breast cancer The Lancet Oncology **5** pp 165-173

Van Eijk C W E, 2002 Inorganic scintillators in medical imaging (Topical Review) Phys. Med. Biol. **47** R85-R106

Van Laere K, Koole M, Lemahieu I, Dierckx R, 2001 Image filtering in single-photon emission computed tomography: principles and applications Comput. Med. Imaging Graph **25** pp 127-133

Veronesi U, Orecchia R, Luini A, Gatti G, Intra M, Zurrida S., Ivaldi G, Tosi G, Ciocca M, Tosoni A, DeLucia F.2001 A preliminary report of intraoperative radiotherapy (IORT) in limited-stage breast cancers that are conservatively treated European Journal of Cancer pp 2178-2183

Veronesi U, Marubini E, Mariani L, Galimberti V, Luini A, Veronesi P, Salvadori B, Zucali R 2001 Radiotherapy after breast-conserving surgery in small breast carcinoma: Long-term results of a randomised trial Annals of Oncology 12 pp 997-1003

Warnke PC; Kopitzki K; Ostertag CB, 2003 Interstitial Stereotactic Radiosurgery ACT NEUR S, **88**: pp 45-50

Watanabe Y, Anderson L L, 1997, A system for nonradiographic source localisation and real-time planning of intraoperative high dose rate brachytherapy Med. Phys. **24** (12) pp 2014-2023

Walters B R B, Rogers D W O, 2002 DOSXYZnrc Users Manual, Ionizing Radiation Standards National Council of Canada, Ottawa, NRCC report PIRS-794

Webb S, 2002, "The Physics of Medical Imaging" IOP Publishing, Bristol, UK

Wermes N, 2004, Trends in pixel detectors IEEE Trans. Nucl. Science 51 pp 1006-1015

Williamson J F, 1987 Monte Carlo evaluation of kerma at a point for photon transport problems Med Phys **14** (4) pp 567-576

Williamson J F, 1991 Comparison of measured and calculated dose rates in water near I-125 and Ir-192 seeds Med. Phys **18** (4) pp 776-786

Yaffe M J, Rowlands J A, 1997 X-ray detectors for digital radiography (Review) Phys. Med. Biol. **42** pp 1-39

Yanch J.C., Harte K.J. 1996, Monte Carlo simulation of a miniature, radiosurgery x-ray tube using the ITS 3.0 coupled electron-photon transport code. Med. Phys. **23** (1), pp 45-52

Yasuda T, Biggs P, Beatty J, Gall K, 1998 Two dimensional Dose Distribution of a miniature x-ray device for stereotactic radiosurgery. Med. Phys. **23** (6) 1166